Controlled Release of Isoniazid by Hybrid Systems

By

Jéssica DE CARVALHO ARJONA

MANUSCRIPT-BASED THESIS PRESENTED TO ÉCOLE DE TECHNOLOGIE SUPÉRIEURE AND UNIVERSITY OF SAO PAULO IN PARTIAL FULFILLMENT FOR THE DEGREE OF DOCTOR OF PHILOSOPHY
Ph.D.

MONTRÉAL, AUGUST 15th, 2025.

ÉCOLE DE TECHNOLOGIE SUPÉRIEURE
UNIVERSITÉ DU QUÉBEC

BOARD OF EXAMINERS

THIS THESIS WAS EVALUATED

BY THE FOLLOWING JURY COMMITTEE:

Mrs. Nicole Raymonde Demarquette, Thesis Supervisor
Mechanical Engineering Department at École de Technologie Supérieure.

Mr. Francisco Rolando Valenzuela-Diaz, Thesis Supervisor
Metallurgical and Materials Engineering Department at the Polytechnic School of the University of São Paulo.

Mr. Ricardo Izquierdo, Chair, Board of Examiners
Electrical Engineering Department at École de Technologie Supérieure

Mr. Ali Ahmadi, jury member
Mechanical Engineering Department at École de Technologie Supérieure.

Mrs. Carina Ulsen, jury member
Mining and Petroleum Engineering Department at the Polytechnic School of the University of São Paulo.

Mr. Antonio Hortêncio Munhoz Junior, external evaluator
Universidade Presbiteriana Mackenzie.

THIS THESIS WAS PRESENTED AND DEFENDED

IN THE PRESENCE OF A BOARD OF EXAMINERS AND THE PUBLIC

ON AUGUST 04, 2025

AT ÉCOLE DE TECHNOLOGIE SUPÉRIEURE.

Ao meu grande amor, meu marido, que sempre me impulsiona a dar voos mais longos.

ACKNOWLEDGMENTS

This work is not mine alone. I had the help and support of amazing people from Brazil and Canada, in many different ways, whether by giving me guidance, ideas, or simply cheering me on. If you gave me a chance to talk about this project or encouraged me at any point, thank you so much! I really appreciate it, and I will never forget.

I also thank the members of the jury for agreeing to evaluate my thesis, as well as for their advice and constructive criticism.

Prof. Dr. Carina Ulsen e ao LCT pela disponibilidade em ajudar e a melhorar o trabalho. Agradeço também ao grupo de pesquisa da Prof. Dr. Dayane Tada pelos ensaios de citotoxicidade.

Aos meus orientadores, Prof. Dr. Francisco Valenzuela e Prof. Dr. Nicole Demarquette, eu agradeço primeiramente pela oportunidade de trabalhar com vocês. Agradeço por terem me ensinado, apoiado, criticado, apontado um melhor caminho sempre que necessário. Serei eternamente grata pela oportunidade e por todos os ensinamentos. Agradeço ao Prof Francisco pela sua calma e apoio em todos esses anos, desde 2014 trabalhando juntos e até hoje me surpreendo com a sua gentileza e leveza de ser. Agradeço à Prof Nicole por seu carisma e sua humanidade, por ter acreditado neste projeto e me convidado a vir à Montreal em 2021. Agradeço o acolhimento, os conselhos, os incentivos e puxões de orelha. Me inspiro na sua maneira de enxergar o mundo e na sua habilidade de fazer ciência e de divulgação científica.

To the Drug Delivery Team, including professors Dr. Ali Ahmadi (for your comments and suggestions and thoughtful advices in performing drug release tests), Dr. Sophie Lerouge (for guiding me with rheology of hydrogels and help me to organize better the work methodologies), Dr. Milan Bergeron-Brlek (for all meetings where you kind helped me with H-NMR results interpretation), Dr. Amilton Martins dos Santos (for guiding me with pullulan modification methodologies), and Dr. Julio César dos Santos, and Dr. Shahriar Ghaffari, for their valuable contributions to this work.

Aos meus colegas de Laboratório de Argilas, Larg, por terem me recebido desde 2014. Agradeço a todos que passaram, mas principalmente ao técnico Wilson Maia, que me auxiliou em tantas demandas, e às minhas queridas colegas que escutaram meus medos e anseios, me deram ideias de como melhorar meu trabalho e dicas valiosas que vou levar para o resto da vida, as doutoras Maria das Graças Silva-Valenzuela e Tatiana Oliveira. Um agradecimento especial à Graça por ter me orientado desde a iniciação científica e ser uma inspiração para mim. Eu serei eternamente grata a todas as nossas conversas, e peço desculpas pela minha teimosia.

To my wonderful colleagues at PolymerETS and former LIPEC, I am genuinely grateful for the warm welcome and constant support you have provided me throughout these years. Special thanks to Mauricio, whose thoughtful advice on presenting my data and insightful ideas helped me immensely whenever I felt stuck; to Ziani, for patiently teaching me how to perform rheological tests, use the rheometer, and organize parameters; and to Atefe, my amazing partner in the Pullulan meetings, whose knowledge and generous support made a significant difference in my work. Heartfelt thanks to Hind, whose friendship brought me comfort and joy when I was far from my family. I also deeply appreciate Jessica, Iman, Samira, Romain, Sare, Behnam, Mohammad, Daria, Judith, Laura, Étienne, and Killian for their kindness, good humor, and encouragement, which brightened many of my days.

To Mazen Samara, thank you for your incredible patience with my writing, for guiding me in organizing data effectively, and for always being available to help improve my work, telling me good jokes, and being supportive when I was stressed about PhD life. A big thank you to the technicians, Nabil Mazeghrane, Dmytro Kevorkov, and Marielle Jacques, for all your training sessions and helpful conversations.

Special gratitude goes to the research associate, MSc. Julie Bertucceli, thank you for your endless patience, kindness, and invaluable guidance during the rheological tests, and to Elie Daoust and their colleagues at *Laboratoire de Biomatériaux et Biofabrication*. To undergraduate student Colyne Jacques and master's student Juliette Crey, thank you for your essential support in numerous lab experiments and the great conversations we've shared. I hope I've made a positive contribution to your academic journey and that you've gained valuable experience from our projects together.

Aos meus avós que passaram tantas dificuldades que eu não consigo nem imaginar. Que criaram suas famílias com a força de só quem não tem outra opção poderia conseguir. Por terem trabalhado na roça, sol a sol, terem criado tantos filhos quanto Deus quis mandar, superado a fome e o frio, para que duas gerações depois, eu pudesse estar aqui, colhendo os frutos que vocês plantaram lá atrás. Obrigada, vô Darcy, vó Maria, vô João, e, especialmente, minha amada vó Dita. Vocês estarão sempre comigo no que vivemos e nas histórias que eu ouvi sobre vocês. Também agradeço aos meus tios, tias, primos e primas. Só quem veio de uma grande família unida sabe o impacto que a vida familiar tem na construção da nossa força e caráter. À minha madrinha, Gabi, que cuidou de mim e dos meus irmãos como mãe. É realmente muito bom saber que a gente sempre pode voltar para onde veio.

Aos meus irmãos, Thiago, Jaqueline e Caroline. Obrigada por existirem, eu realmente não sei o que teria sido de mim sem vocês na minha vida. Ao Thiago por ser o alívio cômico da nossa família, por trazer leveza e risadas mesmo nos momentos mais difíceis. À Jaqueline por ser um exemplo de força e estar sempre disposta a lutar por aquilo que acredita e ajudar todos ao seu redor. À Caroline por ser a personificação da gentileza, por ser aberta às pessoas e ser o porto seguro de tanta gente. Todo dia eu me inspiro para ser um pouquinho mais como vocês. Eu agradeço por vocês terem sempre acreditado em mim, mesmo quando eu duvidava bastante.

À minha base, meus pais, Roberto e Margarida, que me ensinaram pelo exemplo. Ao meu pai, agradeço por me mostrar que mesmo diante da secura da vida, podemos ser doces, gentis e solícitos com todos ao nosso redor. Por ser meu exemplo de bom humor e carisma, espero um dia ser igual ao senhor. À minha mãe por ter sido exemplo de força, perseverança e garra, por ter me ensinado que mesmo na tarefa mais difícil, o melhor a se fazer é seguir. Sem perceber, acabei seguindo seus passos e seus exemplos. Eu amo vocês dois, esse título é nosso.

Ao meu marido, que há onze anos é o maior e melhor parceiro que eu poderia encontrar. Que se tornou minha família, minha base e meu porto seguro; que me permite vacilar e ser

pequena, para me sustentar nos momentos de trevas. Por estar comigo independente do que aconteça e de como eu esteja. Obrigada por ser tudo aquilo que eu preciso, por sair de cena para me mostrar como sou forte e voltar para celebrar comigo todas as nossas conquistas.

E, por fim, agradeço à Deus, que, para mim, é essa energia que me permite desabar e chorar quando tudo vai mal. Mas, que no outro dia, me dá a força necessária para seguir e enfrentar os problemas de frente. Que, quando eu penso em desistir, sussurra ao meu ouvido “Hoje, não. Desista amanhã”. Graças a Ele, esse amanhã ainda não chegou.

Libération Contrôlée de l'Isoniazide pour les Systèmes Hybrides

Jessica DE CARVALHO ARJONA

RÉSUMÉ

Les argiles et les polysaccharides se démarquent comme des vecteurs prometteurs pour la libération contrôlée de médicaments, en raison de leur biocompatibilité, de leur polyvalence et de leur faible coût. Cette étude explore le potentiel des argiles smectites et des hydrogels de pullulane modifiée comme véhicules de libération de l'isoniazide (INH), un médicament de première ligne dans le traitement de la tuberculose. Sept argiles naturelles et synthétiques ont été caractérisées par FRX, DRX, FTIR, BET et TGA afin d'examiner la relation entre le volume des pores, la charge de surface et les mécanismes d'adsorption et de libération de l'INH. L'argile présentant un volume de pores optimal (~0,100 cm^3/g) a montré une capacité supérieure de rétention et de libération prolongée en milieu neutre. L'adsorption maximale (~115 mg/g) a été observée avec la montmorillonite à pH 2, condition dans laquelle l'INH, chargée positivement, interagit plus fortement avec les surfaces argileuses chargées négativement. Des essais comparatifs avec la Laponite, une argile de type hectorite, ont démontré que la charge de surface et la structure poreuse influencent significativement l'efficacité d'incorporation et de libération, la montmorillonite libérant moins de 8 % de l'INH dans des conditions gastriques simulées. Les mécanismes d'adsorption ont varié selon le pH, passant d'une adsorption en monocouche à une adsorption en multicouches, ce qui a directement influencé la cinétique de libération. Les hybrides en monocouche ont suivi un profil de libération d'ordre zéro ($R^2 > 0,93$), assurant une libération régulière et contrôlée. Les tests de cytocompatibilité ont confirmé la tolérance cellulaire sécurité des systèmes à base d'argile. Parallèlement, la pullulane a été fonctionnalisée avec de l'anhydride méthacrylique, permettant une réticulation par UV et la formation d'hydrogels aux propriétés de gonflement modulables. Le degré de fonctionnalisation a été confirmé par H-NMR et FTIR, tandis que le degré de réticulation, évalué par rhéologie, a eu un impact direct sur la capacité de gonflement et les profils de libération de l'INH en conditions gastro-intestinales (pH 7.4). Les hydrogels de pullulane ont démontré des avantages en matière de procédés durables et un fort potentiel pour la libération prolongée de médicaments. Ces résultats apportent des contributions précieuses au développement de systèmes avancés de libération de médicaments sensibles au pH,

mettant en lumière le potentiel complémentaire des argiles naturelles et des biopolymères modifiés dans des applications biomédicales.

Mots-clés : argiles, libération de médicaments, isoniazide, pullulane, hydrogels

Controlled Release of Isoniazid by Hybrid Systems

Jessica DE CARVALHO ARJONA

ABSTRACT

Clays and polysaccharides have emerged as promising platforms for drug delivery due to their biocompatibility, tunable properties, and cost-effectiveness. This study investigates the potential of smectite clays and modified pullulan hydrogels as drug carriers for isoniazid (INH), a first-line treatment for tuberculosis. Seven natural and synthetic clays were characterized by XRF, XRD, FTIR, BET, and TGA to explore the relationship between pore volume, surface charge, and INH adsorption/release. The clay exhibiting an ideal pore volume (~0.100 cm^3/g) displayed superior retention and sustained release in neural environment. Optimal adsorption (~115 mg/g) was achieved with montmorillonite at pH 2, where INH is positively charged and interacts more strongly with negatively charged clay surfaces. Comparative tests with Laponite, a hectorite clay type, revealed that surface charge and pore structure significantly influence both incorporation and release efficiency, with montmorillonite releasing less than 8% INH under simulated gastric conditions. Adsorption mechanisms varied with pH, transitioning from monolayer to multilayer regimes, which in turn influenced the release kinetics. Monolayer-loaded hybrids followed a zero-order release profile ($R^2 > 0.93$), offering steady and controlled delivery. Cytocompatibility tests confirmed the safety of the clay-based systems. In parallel, pullulan was functionalized with methacrylic anhydride to enable UV cross-linking, forming hydrogels with tunable swelling properties. The degree of functionalization was confirmed by H-NMR and FTIR. Crosslinking degree, confirmed by rheology, directly impacted the hydrogel swelling capacity and INH release profiles under gastrointestinal conditions (pH 7.4). The pullulan hydrogels demonstrated green-processing advantages and potential for sustained drug delivery. Together, these findings provide valuable insights into the design of advanced, pH-responsive drug delivery systems. By elucidating the interplay between material structure, drug state, and release behavior, this work supports the development of optimized carriers for tuberculosis therapy and highlights the complementary potential of natural clays and modified biopolymers in biomedical applications.

Keywords: clays, drug delivery, isoniazid, pullulan, hydrogel

Liberação Controlada de Isoniazida por Sistemas Híbridos

Jessica DE CARVALHO ARJONA

RESUMO

As argilas e os polissacarídeos têm se destacado como veículos promissores para a liberação controlada de fármacos, devido à sua biocompatibilidade, versatilidade e baixo custo. Este estudo explora o potencial de argilas esmectitas e de hidrogéis de pullulan modificada como carreadores para a isoniazida (INH), medicamento de primeira linha no tratamento da tuberculose. Sete argilas naturais e sintéticas foram caracterizadas por FRX, DRX, FTIR, BET e TGA, com o objetivo de investigar a relação entre o volume de poros, a carga superficial e os mecanismos de adsorção e liberação da INH. A argila que apresentou volume de poros ideal (~0,100 cm^3/g) revelou maior capacidade de retenção e liberação sustentada em meio neutro. A adsorção máxima (~115 mg/g) foi observada para a montmorilonita em pH 2, condição em que a INH, carregada positivamente, interage de forma mais intensa com superfícies argilosas negativamente carregadas. Ensaios comparativos com Laponita, uma argila do tipo hectorita, demonstraram que tanto a carga superficial quanto a estrutura porosa influenciam significativamente a eficiência de incorporação e liberação, sendo que as montmorilonitas liberaram menos de 8% de INH em condições gástricas simuladas. Os mecanismos de adsorção variaram conforme o pH, passando de monocamada para multicamadas, o que afetou diretamente a cinética de liberação. Híbridos com adsorção em monocamada seguiram um perfil de liberação de ordem zero ($R^2 > 0,93$), promovendo liberação constante e controlada. Ensaios de cito compatibilidade confirmaram a segurança dos sistemas à base de argila. Em paralelo, a pullulan foi funcionalizada com anidrido metacrílico, permitindo sua reticulação por UV e originando hidrogéis com capacidade de inchamento ajustável. A funcionalização foi confirmada por H-NMR e FTIR, e o grau de reticulação, avaliado por reologia, influenciou diretamente a capacidade de intumescimento e os perfis de liberação da INH em condições gastrointestinais (pH 7.4). Os hidrogéis de pullulan apresentaram vantagens sustentáveis de processamento e elevado potencial para liberação prolongada de fármacos. Esses resultados oferecem contribuições relevantes para o desenvolvimento de sistemas avançados de

liberação de fármacos responsivos ao pH, destacando o potencial complementar entre argilas naturais e biopolímeros modificados em aplicações biomédicas.

Palavras-chave: argilas, liberação de fármacos, isoniazida, pullulana, hidrogéis

TABLE OF CONTENTS

Page

LIST OF TABLES

Page

LIST OF FIGURES

Page

LIST OF ABBREVIATIONS AND ACRONYMS

Abs	Absorbance
ANOVA	Analysis Of Variance
APIs	Active Pharmaceutical Ingredients
BET	Brunauer-Emmett-Teller
CEC	Cation Exchange Capacity
CL	Cloisite
CW	Cellulose Whiskers
DD	Drug Delivery
DDS	Drug Delivery Systems
DMEM	Dulbecco's Modified Eagle Medium
DMSO	Dimethyl Sulfoxide
DSC	Differential Scanning Calorimetry
FBS	Fetal Bovine Serum
FTIR	Fourier Transform Infrared Spectroscopy
GI	Gastrointestinal
HIV	Human Immunodeficiency Virus

HMP	Hydroxypropyl Methylcellulose
HNMR	Proton Nuclear Magnetic Resonance
HPC	Hydroxypropyl Cellulose
ICDD	International Centre for Diffraction Data
ICP-OES	Inductively Coupled Plasma Optical Emission Spectroscopy
ICSD	Inorganic Crystal Structure Database
INH	Isoniazid
IR	Immediate Release
IUPAC	International Union of Pure and Applied Chemistry
LDHs	Layered Double Hydroxides
LOI	Loss In Ignition
LP	Laponite
LPNs	Lipid-Polymer Nanoparticles
MA	Methacrylic Anhydride
MIC	Minimum Inhibitory Concentration
MR	Modified Release
Mtt	Montmorillonite

MTT	(3-(4,5-Dimethylthiazol-2-Yl)-2,5-Diphenyltetrazolium Bromide)
PBS	Phosphate Buffer Solution
PEG	Polyethylene Glycol
PEGDA	Polyethylene Glycol Diacrylate
PEO	Polyethyleneoxide
PFO	Pseudo-First Order Model
PLA	Polylactic Acid
PLGA	Poly(Lactide-Co-Glycolide)
PLLA	Poly-L-Lactic Acid
PSO	Pseudo-Second Order Model
Pul	Pullulan
PulMA	Pullulan Methacrylated
PVA	Polyvinyl Alcohol
RIF	Rifampicin
SD	Substitution Degree

SR	Sustained Release
SSR	Sum of Squared Residuals
TB	Tuberculosis
TGA	Thermogravimetric Analysis
TGA	Glass Transition Temperature
TOT	Tetrahedral-Octahedral-Tetrahedral Structure
UNIFESP	Universidade Federal De São Paulo
UV	Ultraviolet Light
UV-vis	Ultraviolet Visible Light Spectroscopy
VC	Verde Claro
VL	Verde Lago
VR	Verde Rosa
VVd	Verde Verde
VVm	Verde Vermelho
WHO	World Health Organization
XRD	X Ray Diffraction
XRF	X Ray Fluorescence

LIST OF SYMBOLS AND UNITS OF MEASUREMENT (INTERNATIONAL SYSTEM)

%	Percentage
°	Degree
°C	Celsius temperature
2θ	Diffraction angle between Incident and Reflected X-Rays
C	Concentration
C_{1t}	Percentage of drug released at time from system 1 (%)
C_{2t}	Percentage of drug released at time from system 2 (%)
C_e	Equilibrium concentration (mg/L or mmol/L)
cm^{-1}	Wavenumber (spatial frequency of a wave)
cm^3/g	Volume (centimeter cubic) per gram
Da	Dalton (atomic mass unit)
f_2	Similarity factor
g	Gram
G'	Storage modulus (Pa)

G"	Loss modulus (Pa)
g/L	Gram per liter
g/m^3	Gram per meter cubic
h	Hours
K	Kelvin temperature
K_0	Zero-order model constant
k_1	Pseudo-first-order constant
k_2	Pseudo-second-order constant
k_d	Adsorption-diffusion constant
K_F	Freundlich adsorption model constant
K_h	Higuchi model constant
K_{kp}	Korsmeyer-Peppas model constant
K_L	Langmuir adsorption model constant
m	Weight (g)
M_∞	Initial amount of drug (mg)
mg	Milligram
mg/g	Milligram per gram

mg/L	Milligram per liter
min	Minutes
mL	Milliliter
mmol/L	Millimole per liter
mol/L	Mole per liter
mol/m^3	Mole per cubic meter
M_t	Amount of drug release at time (mg)
mV	Millivolts
n	Release exponent in the Korsmeyer-Peppas model
n_{ab}	Amount of drug incorporated by clay (mg/g)
N_f	Freundlich adsorption model exponent
nm	Nanometer
p	p-value (statistical significance level)
Pa	Pascal
ppm	Parts per million
q_e	Quantity of INH adsorbed at equilibrium (mg/g)

Q_i	INH initial concentration (mg/L or mmol/L)
$q_{i,exp}$	Experimental adsorption data values (mg/g)
$q_{i,model}$	Model-predicted adsorption values (mg/g)
Q_m	Theoretical amount of drug absorbed at equilibrium (mg/g)
Q_e	Isoniazid residual concentration in the supernatant (mg/L)
q_t	Quantity of INH adsorbed during the time interval (mg/g)
R	Universal gas constant (J/molK)
R^2	Coefficient of determination
R_L	Langmuir model separation factor
rpm	Rotations per minute
t	Time (min or h)
T	Temperature (K or °C)
v/v	Volume per volume
W/g	Wats per gram
w/v	Weight per volume
w/w	Weight per weight
W_d	Hydrogel dried weight (g)

W_s	Hydrogel swollen weight (g)
δ_{cros}	Crosslinking density (g/cm^3)
λ	Wavelength (nm)

INTRODUCTION

This chapter provides a foundational overview of tuberculosis and isoniazid, establishing the relevance and significance of the research topic. It then outlines the specific objectives of the study and concludes with a description of the structure and organization of the thesis.

0.1 Context

Tuberculosis (TB), caused by the bacterium *Mycobacterium tuberculosis*, remains one of the leading causes of death from a single infectious agent, with an estimated 10.6 million people developing the disease in 2022 and 1.3 million deaths among HIV-negative individuals (WHO, 2024, 2020). These figures fall short of the WHO's target to eliminate TB as a global health threat by 2030. In Canada, TB incidence is rising, with approximately 75% of Canadian-born cases occurring among Inuit and First Nations populations (PUBLIC HEALTH AGENCY OF CANADA, 2025). In Brazil, TB is often considered a social disease, disproportionately affecting low-income regions with limited access to healthcare MINISTÉRIO DA SAÚDE (2025).

Given the global burden and the challenges posed by poor treatment adherence and drug resistance, effective pharmacological strategies are essential. Isoniazid (INH), a first-line antitubercular agent, remains a cornerstone in standard regimens. INH is a crystalline, water-soluble compound with a molar mass of 137 g/mol and the molecular formula $C_6H_7N_3O$ (Damasceno Junior et al., 2019). Due to its high minimum inhibitory concentration (MIC) and rapid systemic clearance, it is typically administered in high daily doses of up to 300 mg (Bhandari, 2012; James C. Johnston & Menzies, 2022). Co-administration with other drugs, such as rifampin or pyrazinamide, can further reduce its bioavailability due to pharmacokinetic interactions (Esperanza Carazo et al., 2019).

Extended high-dose INH therapy is associated with severe hepatotoxicity, neurotoxicity, and nephrotoxicity (Damasceno Junior et al., 2019; C. Li et al., 2022) negatively affecting patient's quality of life and treatment adherence (C. Li et al., 2022). Moreover, suboptimal adherence contributes significantly to the emergence of drug-resistant TB strains, posing a major threat to public health systems worldwide.

Pharmacokinetic studies show that INH undergoes protonation in the acidic gastric environment, impairing absorption and reducing therapeutic efficacy (Damasceno Junior et al., 2019). To increase its efficiency, studies in the area are pointing out that one of the best solutions is the controlled release of this drug, enhancing drug stability, bioavailability, and patient compliance. Several inorganic materials have been explored as carriers, including montmorillonite (Mtt) (Esperanza Carazo et al., 2018), halloysite (E. Carazo et al., 2017), palygorskite (E. Carazo et al., 2018), zeolite (Souza et al., 2021), and layered double hydroxides (LDHs) (Muráth et al., 2023; Zauška et al., 2022). These carriers offer tunable interlayer spaces and good biocompatibility, enabling the intercalation of drugs and sustained release. Montmorillonite is especially attractive for oral DD applications, as it is low-cost, non-toxic, and stable under gastrointestinal conditions (Almeida et al., 2019; Tören & Mazari, 2024). Nevertheless, the use of Mtt for INH delivery has been insufficiently explored, particularly regarding the influence of clay composition, structure, and processing conditions on adsorption and release performance.

Polymeric matrices, such as microparticles (Angadi et al., 2010; Anisimova et al., 2000) and hydrogels (Adoungotchodo et al., 2021; Badr et al., 2023; Caliceti et al., 2001; Jiang et al., 2009), have also gained traction as drug delivery platforms due to their controlled swelling behavior and biodegradability (Jiang et al., 2009; Sosnik & Seremeta, 2015). Among them, hydrogels are particularly promising for oral delivery due to their ability to retain large amounts of water and mimic the properties of biological tissues.

Pullulan-based hydrogels represent a promising platform for isoniazid delivery due to pullulan's biodegradability, biocompatibility, and origin from renewable biomass (Pires et al., 2024; Singh et al., 2021). Its natural water solubility eliminates the need for organic solvents, making it suitable for environmentally friendly processing and safer biomedical applications. Moreover, pullulan hydrogels can be engineered for both oral and topical drug delivery routes. Although relatively few studies have investigated their use for anti-tuberculosis therapies, preliminary results have demonstrated their potential as effective carriers in biomedical contexts (Bae et al., 2011; Tören & Mazari, 2024).

This thesis aims to develop and evaluate drug delivery systems for the controlled release of INH. Seven different clay samples were investigated for their adsorption capacity and release kinetics under various pH and drug concentration conditions. In addition, pullulan,

a water-soluble, biodegradable polysaccharide, was explored as a hydrogel-forming matrix due to its environmentally friendly processing and biocompatibility. However, because of its high-water solubility, pullulan was chemically modified with methacrylic anhydride and crosslinked to reduce solubility and achieve sustained release.

In this context, two distinct platforms were selected for the controlled release of isoniazid: clays and pullulan-based hydrogels. Clays are low-cost, abundant, and biocompatible materials that offer a practical and scalable solution for improving TB treatment, especially in low-income regions where the disease burden is highest (Almeida et al., 2019; Esperanza Carazo et al., 2018; Tören & Mazari, 2024). Their integration into drug delivery systems could reduce costs for public health systems while enhancing therapeutic outcomes. In parallel, pullulan hydrogels can offer a biocompatible and adaptable matrix for both oral and topical administration (G. Chen et al., 2018; Sosnik & Seremeta, 2015), which is particularly promising for cases such as cutaneous TB, where local delivery can reduce systemic side effects and improve treatment efficacy (G. Chen et al., 2018). Importantly, the systems developed in this study are not limited to TB treatment; the insights gained may extend to other therapeutic agents and infectious diseases, underscoring the broader significance and potential global impact of this work.

0.2 Objectives

The main objective of this work is to develop controlled drug delivery (DD) systems for tuberculosis treatment by investigating two distinct platforms for the release of isoniazid (INH): clay-based carriers and pullulan-based hydrogels. The specific objectives are:

1. To develop a clay-based drug delivery system.

2. To develop a pullulan-based hydrogel system.

0.3 Thesis Outline

Following this introduction, Chapter 1 presents a literature review covering the fundamental concepts of drug delivery systems, the use of clays as drug carriers, the role

of polymers in the controlled release of isoniazid (INH), and the structure, applications, and chemical modification of pullulan. Chapter 2 outlines the general and specific objectives of the study. Chapter 3 describes the materials and methodologies employed to address each objective.

Chapters 4 to 7 present the experimental results and are organized around the manuscripts produced during this research. Three articles have been published, and they are presented in chapters 4 to 6. These chapters primarily address the first objective of this thesis, which is clay-based drug delivery systems, focusing on the influence of clay properties, drug concentration, and pH on INH adsorption and release. Although the second objective, centered on pullulan hydrogels, was not the focus of the submitted manuscripts, the results obtained were promising. The data are currently being organized for a future manuscript and are discussed in the corresponding chapter.

Finally, the conclusion section highlights the significance of the findings and outlines potential directions for future research in the development of advanced drug delivery systems.

CHAPTER 1

LITERATURE REVIEW

This chapter is organized into two main sections: General Background and State of the Art. The first section provides a concise overview of the key concepts relevant to this research, including drug delivery systems, the structural properties of clays, pullulan as a biopolymer, and the pharmaceutical compound isoniazid. The second section presents a critical review of recent literature focused on the use of clays as drug delivery vehicles, the application of pullulan in drug delivery, and the release behavior of isoniazid in various delivery systems.

1.1 General Background

1.1.1 Drug Delivery Systems

Drug delivery systems (DDS) are engineered to optimize the therapeutic performance of active pharmaceutical ingredients (APIs) by controlling the rate, time, and place of drug release within the body. These systems aim to maximize efficacy while minimizing side effects and degradation prior to reaching the target site. DDS can generally be classified into two broad categories: immediate release (IR) and modified release (MR) formulations (Hillery & Brayden, 2017).

Immediate release systems are designed for rapid disintegration and absorption, allowing the drug to enter systemic circulation almost immediately after administration. In contrast, modified release systems regulate the release profile to improve pharmacokinetics and patient compliance. A key subclass of MR is sustained release (SR), which enables prolonged therapeutic action by gradually releasing the drug over an extended period. This approach helps avoid the initial burst release, a sudden, high-concentration exposure that may cause toxicity or diminished therapeutic effectiveness (Hillery & Brayden, 2017).

Various strategies are employed to achieve sustained release, including encapsulation within polymeric matrices, adsorption onto porous carriers, and chemical modification of the drug or carrier. These methods not only prolong release but can also protect the drug from harsh physiological environments, such as acidic gastric conditions or enzymatic degradation in the gastrointestinal tract (Chavda & Patel, 2010).

Recent advances in DDS have focused on stimuli-responsive systems, where release is triggered by external or internal stimuli such as pH, temperature, or enzymatic activity. These systems offer site-specific and on-demand drug release, which is particularly advantageous for conditions requiring localized or time-sensitive delivery. Materials such as biopolymers and inorganic clays are increasingly being explored for such applications due to their tunable properties, biocompatibility, and ability to interact with drugs through various mechanisms, including adsorption, intercalation, and encapsulation.

To better understand the mechanisms governing drug release from delivery systems, mathematical models are commonly applied to experimental data. These models help describe the release profile and infer the dominant physical processes, such as diffusion, erosion, or polymer relaxation, involved in drug transport. Among the most widely used models are the zero-order, Higuchi, and Korsmeyer–Peppas models (Ahmed et al., 2019).

The zero-order model assumes a constant drug release rate, independent of concentration, which is ideal for achieving prolonged therapeutic levels. This model is most applicable to systems where the drug is uniformly distributed and the release is governed by a constant driving force. It is typically represented by equation (1.1), where M_t is the amount of drug released at time (t), M_∞ is the initial amount of drug, and k_0 is the zero-order model constant.

$$\frac{M_t}{M_\infty} = K_0 \cdot t \tag{1.1}$$

The Higuchi model is based on Fickian diffusion and is suitable for matrix-based systems, particularly when drug release is controlled by diffusion through a porous matrix. It is described by the equation (1.2), where M_t is the amount of drug released at time (t), M_∞ is the initial amount of drug, and k_H is the Higuchi model constant. This model assumes that the initial drug concentration is much higher than the drug solubility, and that the diffusion path length increases over time as the drug is released.

$$\frac{M_t}{M_\infty} = K_h \cdot t^{0.5} \tag{1.2}$$

The Korsmeyer–Peppas model is a semi-empirical equation used to analyze release data when the mechanism is not well understood or involves more than one type of release

behavior. It is expressed as shown in equation (1.3). Where M_t is the amount of drug released at time (t), M_∞ is the initial amount of drug, and K_{kp} is the model release constant, and n release exponent in the Korsmeyer–Peppas model.

$$\frac{M_t}{M_\infty} = K_{kp} \cdot t^n \tag{1.3}$$

The release exponent in the Korsmeyer-Peppas model indicates the release rate mechanism. Table 1.1 lists the possible n values and their meaning regarding the drug release mechanism. As can be seen, for $n \leq 0.5$, the drug release is mainly driven by Fickian diffusion of the drug to the environment (Vueba et al., 2013). Values of n from 0.5 to 1.0 indicate the non-Fickian diffusion release, and the release mechanism is a combination of diffusion, polymer relaxation, and/or matrix erosion. While $n \approx 1$, called super case II transport, is given when the release is mostly guided by polymer relaxation or swelling (Chavda & Patel, 2010) .

Table 1.1 Correlation between the Korsmeyer-Peppas exponent (n) and the drug release mechanism.
Adapted from Ahmed et al., (2019, p. 55)

Exponent (n)	**Drug Release Mechanism**
$n \leq 0.5$	Fickian diffusion (Case I diffusional)
$0.5 < n < 1.0$	Anomalous (non-Fickian) diffusion
$n \approx 1.0$	Super case II transport

1.1.2 Drug Adsorption by Inorganic Particles

In order to be used as drug release systems, some vehicles, as inorganic particles, first adsorb the drug molecules to further release them. To better understand the mechanism of drug adsorption onto clays or other inorganic particles, two main types of adsorption experiments are typically performed: adsorption kinetics and adsorption isotherms. These experiments help elucidate how the drug interacts with the clay over time and about its initial concentration in solution.

Adsorption kinetics evaluate the influence of contact time between the clay (adsorbent) and the drug (adsorbate). This analysis is essential for determining the rate-limiting steps of the adsorption process, whether they are governed by surface interactions, pore diffusion, or a combination of both. The most commonly applied models are: the pseudo-first order (PFO), pseudo-second order (PSO), and the intraparticle diffusion model.

The Pseudo-First-Order (PFO) model, which assumes that the rate of occupancy of adsorption sites is proportional to the number of unoccupied sites. It is typically expressed as shown in equation (1.4).

$$\frac{1}{q_t} = \left(\frac{k_1}{q_e}\right)\left(\frac{1}{t}\right) + \frac{1}{q_e} \tag{1.4}$$

The Pseudo-Second-Order (PSO) model assumes that adsorption follows a second-order mechanism, often associated with chemisorption, involving valence forces or electron exchange. Its linear form is in equation (1.5).

$$\frac{t}{q_t} = \frac{1}{k_2 q_e^2} + \frac{1}{q_e} t \tag{1.5}$$

The Intraparticle Diffusion (Weber–Morris or ADS) model helps determine whether diffusion within the clay pores contributes significantly to the adsorption process. It is expressed as shown in equation (1.6).

$$q_t = k_d \sqrt{t} \tag{1.6}$$

Where q_t is the quantity of INH adsorbed during the time interval t, q_e is the quantity of INH adsorbed when equilibrium is reached, k_1 is the pseudo-first-order constant, k_2 is the pseudo-second-order constant, and k_d is the adsorption-diffusion constant.

In parallel, adsorption isotherms provide insight into the capacity and surface characteristics of the adsorbent as a function of the initial drug concentration at equilibrium. The two most widely used isotherm models are the Langmuir and the Freundlich isotherms. The Langmuir model, shown in equation (1.7), assumes monolayer adsorption on a homogeneous surface with finite, identical sites and no interaction between adsorbed

molecules, where n_{ab} is the amount of drug adsorbed, K_L is the Langmuir constant, Q_m is the theoretical amount of drug adsorbed at equilibrium, and C_e is the equilibrium concentration. While the Freundlich isotherm, equation (1.8), describes heterogeneous surface adsorption with varying affinities, is useful for non-ideal systems, where n_{ab} is the amount of drug incorporated by clay, C_e is the equilibrium concentration, K_F and n_F are the Freundlich constants.

$$n_{ab} = \frac{K_L Q_m C_e}{1+K_L C_e} \tag{1.7}$$

$$n_{ab} = K_F C_e^{\frac{1}{n_F}} \tag{1.8}$$

Additionally, Giles isotherm classification offers a qualitative method to categorize the isotherm shapes, which can provide useful insights into the adsorbate–adsorbent interaction mechanisms. For example, L-type curves suggest high affinity and monolayer formation, while S-type curves may indicate cooperative adsorption or structural rearrangements during adsorption (C. H. Giles et al., 1960; Charles H. Giles & Smith, 1974).

Together, these models offer a comprehensive understanding of the adsorption behavior of isoniazid onto clay minerals and can support hypotheses about the mechanisms involved, such as electrostatic interactions, hydrogen bonding, or pore filling.

1.1.3 Clays and Clay Minerals

The clays investigated in this study belong to the smectite group, which is extensively utilized in pharmaceutical and environmental applications due to their notable swelling capacity and high sorption potential. Figure 1.1a illustrates the general structure of these minerals. Specifically, two smectite-type clays were examined: montmorillonite and hectorite. Both are members of the phyllosilicate family and exhibit a characteristic 2:1 layered structure, also known as a TOT structure, consisting of one octahedral sheet sandwiched between two tetrahedral silica sheets. In montmorillonite, the octahedral layer

is primarily composed of aluminum (Al^{3+}), while in hectorite, it is predominantly magnesium (Mg^{2+}) (Bergaya et al., 2005; G Lagaly, 2006; G Lagaly et al., 1976).

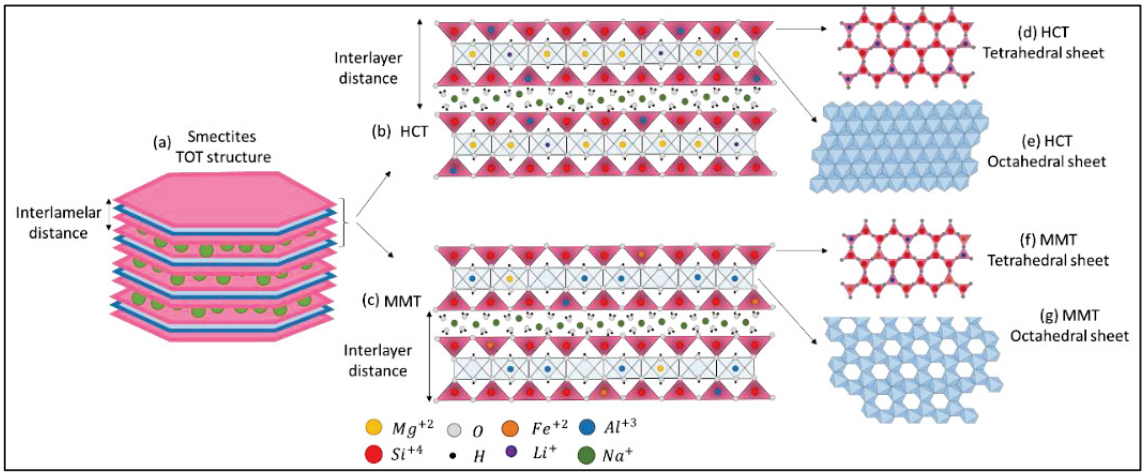

Figure 1.1 Schematic representation of smectite clay structures: (a) general phyllosilicate framework; (b, d, e) trioctahedral structure of hectorite-like clay; (c, f, g) dioctahedral structure of montmorillonite
Taken from de Carvalho Arjona et al. (2025, p. 2)

The crystal chemistry distinguishes the two smectite types. Hectorite-like clays are trioctahedral, meaning all octahedral sites are occupied by divalent cations (typically Mg^{2+}) (Figure 1.1b,d,e). Montmorillonite, by contrast, is dioctahedral, with only two-thirds of the octahedral positions occupied, usually by Al^{3+} (Figure 1.1c,f,g).

During clay mineral formation, isomorphic substitution occurs when cations in the original rock are replaced by others of lower valence (e.g., Si^{4+} by Al^{3+}, or Al^{3+} by Mg^{2+}), resulting in a permanent negative structural charge (Gerhard Lagaly & Beneke, 1976; Nomicisio et al., 2023). This charge is compensated by exchangeable cations, such as Na^{+}, Ca^{2+}, and others, located in the interlayer regions. Each smectite layer is approximately 1 nm thick and may extend up to two microns laterally. These layers are stacked and held together by van der Waals interactions, and the spacing between them, known as the interlamellar distance, is filled with these exchangeable cations (Brigatti et al., 2006). The type and concentration of these cations directly influence the clay's cation exchange capacity (CEC), a critical parameter for adsorption processes (de Paiva et al., 2008).

Additionally, hydroxyl groups located on the edges of clay lamellae contribute to the surface reactivity, especially under acidic conditions. In such environments, H^+ ions can displace the interlayer cations and interact with the hydroxyl groups, thereby modifying the surface charge. This pH-dependent behavior may significantly affect the adsorption and desorption of specific drug molecules, such as isoniazid (Almeida et al., 2019).

Structurally, smectite layers aggregate into tactoids, which further assemble into larger aggregates with variable stacking orientations. This hierarchical architecture results in a complex porous network, enabling smectites to act as porous materials. These materials display micropores (<2 nm), mesopores (2–50 nm), and macropores (>50 nm). Micropores are mainly associated with interlayer spaces within tactoids, whereas meso- and macropores arise from voids between tactoid aggregates (Shah et al., 2018).

The chemical composition, porosity, and CEC play a crucial role in determining the clay's swelling behavior and molecular permeability. The CEC, in particular, reflects the clay's capacity to exchange interlayer cations with those present in the surrounding media (X. Wang et al., 2020). Although atomistic-level simulations have been employed to understand the adsorption and desorption of drugs in clays, experimental results remain inconsistent due to the diversity in clay types and testing conditions (Borrego-Sánchez & Sainz-Díaz, 2021; E. Carazo et al., 2018; Esperanza Carazo et al., 2018, 2019; Damasceno Junior et al., 2019). Based on the findings of this work, the pore volume emerges as a promising parameter influencing drug adsorption and release behavior in smectite clays.

1.1.4 Pullulan

Pullulan (Pul) is a biopolymer derived from microbial fermentation of starch-based biomass and has been widely investigated as a versatile biomaterial over the past few decades. Its chemical structure can be observed in Figure 1.2. As a polysaccharide composed primarily of maltotriose units, pullulan is highly water-soluble, a property that has attracted interest in various pharmaceutical and biomedical applications. It has been employed as a stabilizer for nanoemulsions (Ferreira et al., 2015), in the formulation of fast-dissolving films

(Murata et al., 2010), for taste masking in oral drug delivery (Krieser et al., 2020), and in the production of capsules (Garbacz et al., 2014), among others.

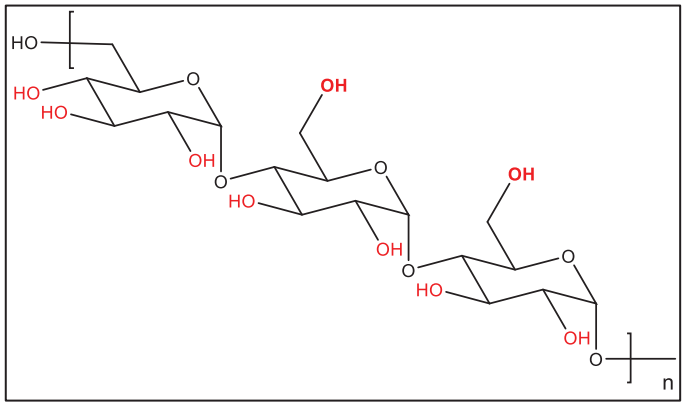

Figure 1.2 Pullulan chemical structure

In the present thesis, the focus is on the use of pullulan as a drug delivery matrix. Although its hydrophilicity is advantageous for some pharmaceutical applications, in the context of controlled drug release, such high solubility may lead to an undesired burst release effect. Therefore, chemical or physical modifications, such as crosslinking or blending with other materials, are often necessary to slow down the dissolution rate, enhance the stability of the matrix, and achieve a more sustained and predictable drug release profile. More details are shown in section 1.2.4.

1.1.5 Isoniazid

Isoniazid (INH) is a first-line antitubercular drug and a cornerstone of standard treatment regimens for tuberculosis. Its chemical structure (Figure 1.3a) comprises a pyridine ring and a hydrazide group, both of which play key roles in its interactions with carrier materials (Almeida et al., 2019; Damasceno Junior et al., 2019) . INH is a crystalline, water-soluble compound with a molar mass of 137 g/mol and molecular formula $C_6H_7N_3O$. Despite its effectiveness, the drug's high minimum inhibitory concentration (MIC) and rapid systemic clearance necessitate high daily doses: often up to 300 mg (Bhandari, 2012; James C. Johnston & Menzies, 2022). When co-administered with other antitubercular agents, such as rifampin or pyrazinamide, its bioavailability may decrease due to pharmacokinetic interactions (Esperanza Carazo et al., 2019).

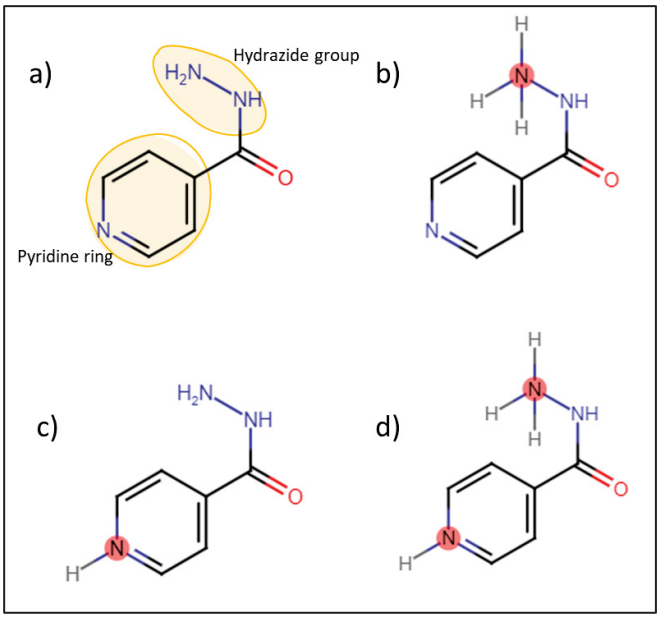

Figure 1.3 The four possible forms of INH (in red, protonated N): a) neutral, b) protonation on N of the hydrazide group, c) protonation on N of the pyridine ring, and d) protonation on N of the hydrazide group and pyridine ring

However, extended high-dose therapy has been associated with significant side effects, including hepatotoxicity, neurotoxicity, and nephrotoxicity (C. Li et al., 2022), which can negatively impact patient adherence and quality of life. Poor adherence not only reduces therapeutic efficacy but also contributes to the emergence of drug-resistant tuberculosis strains, posing a major global public health threat.

INH's pKa values (2.0, 3.6, and 10.8) significantly influence its chemical structure and protonation behavior, which in turn affect its adsorption and release from drug delivery systems. Under acidic conditions, protonation can occur on the hydrazide group (Figure 1.3b) and/or the pyridine nitrogen (Figure 1.3-c-d), altering the drug's interaction with negatively charged surfaces such as those of clay minerals (Souza et al., 2021). This protonation enhances electrostatic interactions, potentially enabling cation exchange and hydrogen bonding with the carrier material (Bhat et al., 2020; Kiaee et al., 2022; Zhu et al., 2016).

Various drug delivery systems have been explored to optimize INH delivery and minimize burst release. These include polymeric carriers (Angadi et al., 2010; Devi & Maji, 2010; Gajendiran et al., 2019; Lucinda-Silva & Evangelista, 2003; Oliveira et al., 2017), 3D-printed pills (Genina et al., 2017), inorganic materials such as zeolites (Souza et al., 2020, 2021), silica nanoparticles (Almeida et al., 2019), and layered double hydroxides (LDHs) (Saifullah et al., 2016). Inorganic clays, such as palygorskite (Akyuz et al., 2010; E. Carazo et al., 2018; Damasceno Junior et al., 2019), montmorillonite (Mtt) (Akyuz & Akyuz, 2008; Esperanza Carazo et al., 2018), hectorite, and halloysite (E. Carazo et al., 2017; Esperanza Carazo et al., 2019), have also been employed, either alone or in combination with polymers (Banik et al., 2012, 2014; G. Chen et al., 2018; Saikia et al., 2015).

1.2 State of the Art

1.2.1 Clays as Drug Delivery Vehicles

The medicinal use of clays dates back to prehistoric times, when they were applied to treat wounds, skin irritations, and gastrointestinal ailments (Carretero, 2002; Gomes & Silva, 2007). Over the years, clays have found extensive use in pharmaceutical formulations, both as active ingredients and as excipients in tablets, creams, and ointments (Aguzzi et al., 2007). Montmorillonite (Mtt), for example, is commonly employed to facilitate pill disintegration through swelling, to act as a lubricating agent during manufacturing, and to serve as an inert base in cosmetics and emulsions (Carretero, 2002; Choy et al., 2007).

The role of clays in modifying drug release and improving stability became evident in the mid-20th century, when researchers observed that clay–drug interactions could alter release kinetics, often slowing drug dissolution and thereby minimizing systemic side effects (Aguzzi et al., 2007; Hulbert et al., 1972). The effectiveness of a clay as a drug carrier depends on multiple factors, including its morphology, microstructure, chemical composition, and surface charge, as well as the physicochemical properties and ionization state of the drug (Hoyo, 2007).

Drug adsorption onto clay typically involves multiple steps: diffusion across the particle surface, migration into internal pores, and interaction with functional sites. Figure 1.4 shows a scheme of how the adsorption in clay samples may occur: via cation exchange in interlamellar regions (Figure 1.4b), often increasing the basal spacing, or through hydrogen

bonding and van der Waals forces in inter-tactoid voids (Figure 1.4c). While these mechanisms have been well documented (Reinholdt et al., 2013; Tan & Hameed, 2017; Zhu et al., 2016), the specific influence of pore volume on drug release, particularly in pharmaceutical contexts, remains underexplored. Most related studies have instead focused on gas sorption in shale-like materials (Feng et al., 2018; X. Wang et al., 2020).

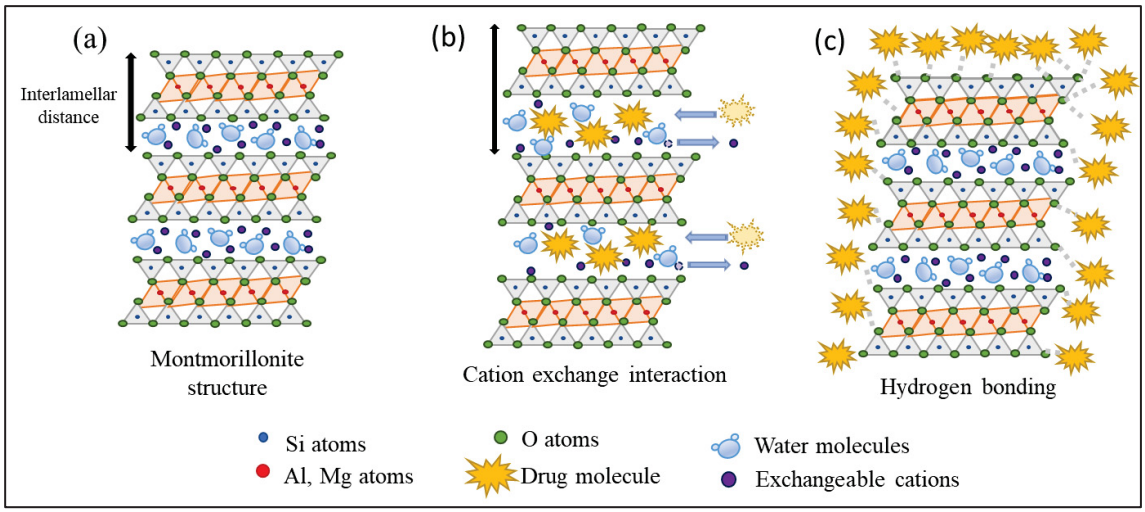

Figure 1.4 Schematic representation of (a) clay layered structure; (b) clay/INH interaction via cation exchange; and (c) clay/INH interaction via hydrogen bonding or van der Waals forces
Taken from de Carvalho Arjona et al. (2024, p. 2)

In recent years, clays have been investigated as nanocarriers for a wide range of therapeutic agents, including anticancer (L. Zheng et al., 2019) and antibiotics (Peng et al., 2018; S. Wang et al., 2012). Their appeal lies in their low toxicity, chemical stability, and cost-effectiveness (E. Carazo et al., 2017, 2018; Esperanza Carazo et al., 2018; Damasceno Junior et al., 2019). Drug-clay hybrids are typically synthesized in aqueous media, where variables such as pH (Damasceno Junior et al., 2019) and temperature (Esperanza Carazo et al., 2018) play key roles. Cationic drugs are particularly well-suited for clay interaction due to the negatively charged surfaces of most clay minerals (Kiaee et al., 2022).

1.2.2 Clays and Other Inorganic Particles as Drug Vehicle for Isoniazid

Akyuz & Akyuz (2008) was one of the first studies that demonstrated the potential of natural clays to adsorb INH, although details such as adsorption efficiency and drug-to-clay ratios were often not reported. After years, multiple types of clay minerals have been tested for INH loading (Almeida et al., 2019; E. Carazo et al., 2017, 2018; Esperanza Carazo et al., 2018; Damasceno Junior et al., 2019; Souza et al., 2021). The overview of research papers that used clays as a vehicle for controlled release of INH is shown in Table 1.2.

Table 1.2 Overview of research articles employing clays for the controlled delivery of INH.

Aim of the Study	Vehicle	Key Findings / Contributions
Evaluate the use of organobentonite in the removal of INH from water waste	Bentonite	Modification of bentonite with glycine enhanced INH adsorption capacity by approximately 60%. Adsorption was strongly pH-dependent, with capacity increasing over 1000% at pH 2 compared to pH 8 (Çalışkan Salihi et al., 2019).
Thermodynamic study of INH adsorption	Halloysite (nanotubes)	Adsorption was found to be spontaneous and endothermic. Contact time had minimal effect on capacity, which increased with rising temperature and initial INH concentration (Carazo et al., 2017).
Study the biocompatibility and drug stability	Halloysite (nanotubes)	While halloysite did not support controlled release, it effectively protected INH from degradation and showed no cytotoxicity (Esperanza Carazo et al., 2019).
Synthesis of layered double hydroxide (LDH) for INH controlled release	LDH	LDH nanoparticles enhanced INH biocompatibility, with more sustained release observed at pH 7.4 due to the basic nature of LDH (Saifullah et al., 2016).
Investigate the interactions between INH and montmorillonite through FTIR spectra	Montmorillonite	The interaction between INH and montmorillonite is primarily basic, driven by hydrogen bonding between the clay surface and INH's nitrogen and oxygen atoms. Pyridine and hydrazide groups play a key role in this interaction (Akyuz & Akyuz, 2008).
Thermodynamic study of INH adsorption	Montmorillonite	Adsorption was spontaneous and exothermic, with capacity increasing alongside temperature and initial INH concentration (Esperanza Carazo et al., 2018).

Aim of the Study	Vehicle	Key Findings / Contributions
Thermodynamic study of INH adsorption	Palygorskite	Adsorption is spontaneous and exothermic. Higher temperatures improved INH retention. Equilibrium was reached after 48 hours, with capacity increasing at higher initial INH concentrations (E. Carazo et al., 2018).
Develop a pH-responsive adsorption system	Palygorskite	Optimized conditions revealed that lower pH enhances INH incorporation, reduced clay mass increases adsorption capacity (mg/g), and higher initial drug concentration improves loading (Damasceno Junior et al., 2019).
Process optimization for INH adsorption	Silica nanoparticles	Adsorption increased with higher INH concentration, greater silica mass, and lower pH. Equilibrium was achieved within a short contact time (Almeida et al., 2019).
Study INH adsorption and release optimization	Zeolite	Equilibrium was reached within 4 hours, with maximum INH incorporation at pH 3. Lower drug concentrations led to higher adsorption efficiency. A burst release governed by Fickian diffusion was observed, followed by limited desorption due to strong drug–clay interactions (Souza et al., 2021).

In all those studies, the adsorption process typically involves dispersing clays in aqueous INH solutions, where parameters such as stirring, pH (Almeida et al., 2019; Damasceno Junior et al., 2019; Souza et al., 2021), and temperature influence drug uptake (E. Carazo et al., 2017, 2018; Esperanza Carazo et al., 2018). To evaluate the adsorption behavior and capacity of clays, thermodynamic adsorption studies are commonly performed (E. Carazo et al., 2017, 2018; Esperanza Carazo et al., 2018). In this method, a fixed amount of clay is added to INH solutions of varying concentrations. For each concentration, the system is allowed to reach equilibrium under controlled conditions. Afterward, the amount of INH adsorbed onto the clay and the amount remaining in solution are quantified. This procedure is repeated with fresh clay samples and progressively higher INH concentrations.

The resulting thermodynamic adsorption test data are used to construct adsorption isotherms, which plot the amount of drug adsorbed per gram of clay against the equilibrium concentration of INH in the solution. These isotherms help to understand the adsorption mechanism and evaluate the maximum adsorption capacity of the material. For example,

papers using halloysite, palygorskite, and montmorillonite have provided insights into enthalpy, entropy, and activation energy changes during INH adsorption (E. Carazo et al., 2017, 2018; Esperanza Carazo et al., 2018). Adsorption isotherms for Mtt, for example, follow a Giles L3 profile (Çalışkan Salihi et al., 2019; Esperanza Carazo et al., 2018; C. H. Giles et al., 1960; Charles H. Giles & Smith, 1974), indicating monolayer formation followed by surface precipitation. Temperature was shown to affect adsorption efficiency, with higher temperatures increasing INH uptake, likely due to enhanced molecular mobility and interaction potential.

As discussed in 1.1.5 Section, the results reported in the literature and in Table 1.2 reported that the adsorption is highly dependent on the pH level (Almeida et al., 2019; Damasceno Junior et al., 2019; Souza et al., 2021). Indeed, INH exhibits a pH-dependent protonation state, which, together with the clay negative surface charge, can modify its interaction with this particle. Acidic environments favor protonation and enhance electrostatic interactions with negatively charged clay surfaces, increasing adsorption (Almeida et al., 2019; Damasceno Junior et al., 2019; Kiaee et al., 2022).

The results of the literature show that, similar to adsorption, INH release from clays and other inorganic carriers also depends on environmental pH. Materials with negatively charged surfaces, such as zeolites (Souza et al., 2021), palygorskite (Damasceno Junior et al., 2019), and silica nanoparticles (Almeida et al., 2019), tend to exhibit lower release rates and reduced cumulative INH release at acidic pH, especially around pH 2, compared to neutral or basic environments. This is likely due to enhanced electrostatic interactions between the protonated INH and the negatively charged surfaces, which hinder drug detachment. In contrast, layered double hydroxides (LDHs), which possess a positive surface charge, show higher release rates under acidic conditions (Saifullah et al., 2016).

However, from all the studies, while adsorption efficiency and pH responsiveness have been demonstrated in several studies (Almeida et al., 2019; Çalışkan Salihi et al., 2019; Damasceno Junior et al., 2019; Souza et al., 2021), most clay and other inorganic particle systems failed to prolong INH release, with complete drug release typically occurring in under 15 minutes (Esperanza Carazo et al., 2019; Damasceno Junior et al., 2019; Souza et al., 2021). However, these systems have shown potential to protect INH in acidic

environments, such as the stomach, and to prevent drug degradation in multi-drug formulations (Esperanza Carazo et al., 2019).

1.2.3 Polymeric Systems for Isoniazid Controlled Release

Approximately 75% of sustained-release oral drug delivery systems are based on hydrophilic polymers configured as matrix tablets. In these systems, the drug is dispersed within the polymer matrix, where water molecules infiltrate the polymer network upon ingestion. As hydration occurs, the polymer chains relax and swell, enabling gradual drug diffusion through the matrix and providing a more controlled release compared to conventional dosage forms (Perrie et al., 2019). Table 1.3 listed some of the recent studies focused on polymer-based drug delivery systems for INH.

Table 1.3 Summary of Recent Studies on INH Controlled-Release Systems Using Polymeric Matrices

Aim of the Study	Matrix	Method of Preparation	Kind of release	Release behavior
Investigate the influence of cellulose whiskers (CW) in gelatin nanoparticles for the release of INH.	Gelatin and cellulose whiskers	Desolvation method followed by crosslinking	Oral release	At higher pH, gelatin relaxation increases, enhancing INH cumulative release. The addition of CW hinders gelatin swelling, reducing release at both acidic and basic pH, and contributing to more controlled delivery (Sarmah et al., 2016).
Obtaining an inhale system for controlled release of INH using lipid-polymer nanoparticles (LPNs).	PLGA (poly(lactide-co-glycolide))	Double emulsification method: water/oil	Oral release	At neutral pH, both PLA and INH exhibit higher solubility, resulting in faster drug release compared to acidic pH. A burst release was observed due to the drug being surface-bound rather than encapsulated, and the hydrophilic nature of the polymer matrix (Bhardwaj et al., 2016a).

Aim of the Study	Matrix	Method of Preparation	Kind of release	Release behavior
Study the release of INH and RIF (rifampicin) blended with PEO (polyethylene oxide) filaments recovered by PLA (polylactic acid) shell and sealed on top by PVA (polyvinyl alcohol).	PVA, PLA, and PEO	3D printing	Oral release	At pH 1.2, only the system with a sealed cap prevented INH release during the first 2 hours. Once the PVA cap dissolved, release accelerated rapidly, reaching completion within 5 hours (Genina et al., 2017).
Study the influence of the different ratios of the copolymer in the incorporation and release of INH	Citrate-PEG (Polyethylene glycol)-PLGA copolymer	Double emulsification method: water/oil/water	Oral release	INH release plateaued after 10 hours for all copolymer compositions. Higher citrate-PEG content led to greater cumulative release over time, attributed to the hydrophobic nature of PLGA (Gajendiran et al., 2019).
A study by atomistic molecular dynamics simulation of the interaction among nanoparticles of two different polymers and INH	PLA and PLGA	Computer simulation	Oral release	Rapid INH release occurred due to diffusion from the nanoparticle core, facilitated by weak drug–polymer interactions (Stipa et al., 2021).
Obtaining tablets for the release of INH and RIF in different pH to avoid drug interactions	Hydroxypropyl cellulose (HPC) to cover INH and hydroxypropyl methylcellulose (HMP) to cover RIF	3D printing	Oral release	INH showed rapid release at low pH, while RIF exhibited slower release at neutral pH (Ghanizadeh Tabriz et al., 2021).

Aim of the Study	Matrix	Method of Preparation	Kind of release	Release behavior
Encapsulate and release INH in a biopolymer matrix by a microfluid platform	Egg white and carrageenan	Droplet-based microfluidics bed followed by microwave irradiation for crosslinking.	Oral release	Higher irradiation power reduced INH release due to more effective crosslinking. Release was more controlled at neutral pH compared to acidic conditions (Marengo et al., 2021).
Development of microcapsules for the release of INH, verifying the influence of chitosan molecular weight.	Chitosan	Spray dryer	Pulmonary release	Non-crosslinked microcapsules showed burst release, whereas crosslinked ones sustained INH release over time (Oliveira et al., 2017).
Obtaining INH incorporated in microcapsules for inhalable antitubercular therapy.	Locust bean gum (polysaccharide)	Spray dryer	Pulmonary release	A burst release was observed, with approximately 90% of INH released within the first 30 minutes (Alves et al., 2016).
Obtaining a system to release INH by transdermal delivery	Elastic liposomes and gel	Dispersion of INH, surfactants, gel, and crosslinked agent.	Transdermal release	The glass transition temperature (Tg) of surfactants influenced gel release behavior. Surfactants with Tg below body temperature enabled faster INH release due to increased molecular flexibility (Altamimi et al., 2020).
Obtaining a membrane of core-shell PLLA microfibers for sustained release of RIF and INH	PLLA (poly-L-lactic acid)	Electrospinning	Transdermal release	At pH 7, a burst release was observed for both INH (core) and RIF (shell) in the nanofibers. INH release was lower due to core localization, reaching equilibrium within one hour with no further increase thereafter (C. Li et al., 2022)

One of the earliest reports on controlled-release systems for INH dates back to 1992. Ishino et al. (1992) developed a pulsatile-release system comprising a core tablet containing INH and a disintegrant, coated with a poorly water-permeable shell. The outer layer delayed the onset of drug release until the core swelled sufficiently to rupture the shell. This approach did not ensure controlled diffusion but allowed for delayed release by modulating the lag before drug liberation.

Several technologies have been developed for the non-conventional release of INH, including 3D printing (Genina et al., 2017; Ghanizadeh Tabriz et al., 2021), spray drying (Alves et al., 2016; Oliveira et al., 2017), emulsion techniques (Bhardwaj et al., 2016b; Gajendiran et al., 2019), electrospinning (C. Li et al., 2022), dispersion methods (Altamimi et al., 2020), desolvation (Sarmah et al., 2016), and microfluidics (Marengo et al., 2021). These studies reflect three primary administration routes for INH delivery systems: oral (Bhardwaj et al., 2016b; Gajendiran et al., 2019; Genina et al., 2017; Marengo et al., 2021; Sarmah et al., 2016; Stipa et al., 2021), pulmonary (inhalable) (Alves et al., 2016; Oliveira et al., 2017), and transdermal (Altamimi et al., 2020; C. Li et al., 2022). Oral systems are typically evaluated at acidic and neutral pH, around 1.2 and 7.4 pH levels, respectively, simulating different regions of the gastrointestinal tract. Transdermal and inhaling systems are commonly tested at pH 7.4, either using a buffer solution or membrane-separated setups.

In recent years, the most common polymeric matrices studied for INH controlled release include PLA (polylactic acid) (Gajendiran et al., 2019; Genina et al., 2017; Stipa et al., 2021), chitosan (Oliveira et al., 2017), gelatin (Sarmah et al., 2016), and other biopolymers (Altamimi et al., 2020; Alves et al., 2016; Ghanizadeh Tabriz et al., 2021; Marengo et al., 2021). However, from the studies reported in the literature, not all biopolymers can be considered for this kind of application, since several parameters affect the efficiency of drug release. Two factors must be taken into consideration: the interaction between the polymer and INH, and the mobility of the polymer chains.

The interaction strength between isoniazid (INH) and the polymer matrix plays a key role in achieving sustained drug release. Stipa et al. (2021) using atomistic molecular dynamics simulations, found that polymers like PLA and PLGA (poly(lactide-co-glycolide)) exhibit weak interactions with INH, resulting in rapid diffusion from the nanoparticle core. Due to

INH's high affinity for water and ions through ion–dipole interactions, carriers with greater hydrophobicity or larger structures may be necessary to improve drug retention and reduce release rates.

The mobility of polymer chains also significantly influences drug diffusion. Polymers with reduced mobility, either because of a higher glass transition temperature (Tg) or crosslinking, tend to slow down the release of INH. Studies by Altamimi et al. (2020) and Marengo et al. (2021) showed that surfactants or crosslinkers with high Tg values effectively decrease the drug release rate. Likewise, Sarmah et al. (2016) demonstrated that cellulose whiskers hinder gelatin swelling, thereby modulating the drug release behavior. Crosslinking is frequently used to mitigate burst release in hydrophilic polymer matrices and can be introduced chemically or via irradiation. The extent and effectiveness of crosslinking, strongly influenced by irradiation dose or intensity, directly affect the drug release profile (Marengo et al., 2021; Oliveira et al., 2017).

Regarding the results of release tests found in the literature, most studies report a burst release profile, especially when the matrix and drug are both water-soluble. The release rate is strongly pH-dependent, with higher INH solubility and faster release generally occurring at neutral pH, especially in matrices such as gelatin, PLA, PVA (polyvinyl plcohol), and chitosan. However, certain systems show higher release in acidic media due to enhanced interactions between polymer chains and protons (H^+), as seen with HPC (Ghanizadeh Tabriz et al., 2021) and egg white–carrageenan biopolymers (Marengo et al., 2021).

As discussed in this section, a variety of polymers have been explored for drug delivery applications, particularly in extended-release formulations. Some of these materials are well established and widely studied; however, their use can be limited by factors related to their origin, including concerns about animal-derived components, which may not align with certain dietary practices, religious beliefs, or ethical preferences. These considerations highlight the growing demand for alternative biocompatible polymers that offer broad acceptability and promote patient compliance (Foox & Zilberman, 2015). In this context, pullulan emerges as a promising candidate. Derived from renewable biomass waste, it

combines environmental sustainability with excellent biocompatibility, making it a strong contender for next-generation drug delivery systems.

1.2.4 Pullulan in Biomedical Applications

Pullulan, a polysaccharide biopolymer derived from microbial fermentation of biomass, has garnered significant attention as a versatile material for biomedical applications. Owing to its excellent water solubility, biocompatibility, and film-forming ability, it has been employed in a range of pharmaceutical formulations, including as a nanoemulsion stabilizer (Ferreira et al., 2015), in fast-dissolving films (Murata et al., 2010), for taste masking in oral drug delivery (Krieser et al., 2020), and in capsule production (Garbacz et al., 2014). In this thesis, the focus is on pullulan's role as a matrix for drug delivery, particularly in hydrogel form. Although high solubility is beneficial for many formulations, it can cause undesirable burst release in controlled delivery systems, thus necessitating structural modification to reduce its water solubility. This happens because body fluids are mainly composed of water, and highly soluble polymers would be dissolved, rapidly releasing the drug at an uncontrolled rate. Table 1.4 presents recent studies that detail various chemical modification strategies used to tailor pullulan for biomedical applications.

Table 1.4 A list of the latest papers regarding pullulan modification for bio applications

Pullulan modifier agent	Modification	Application
Acetic anhydride	Acetylation of pullulan to produce flexible films (Hernandez-Tenorio; Giraldo-Estrada, 2022).	Biomaterials.
Carboxymethyl and tyramine	Crosslinking with pullulan to form hydrogels (F. Chen et al., 2016).	Hydrogel scaffolds for cartilage tissue engineering.
Dextran	Crosslinking of pullulan by sodium trimetaphosphate under alkaline conditions to obtain hydrogels (Grenier et al., 2023).	Hydrogel scaffolds for cell culture.
Epichlorohydrin	Water/oil emulsion crosslinking with pullulan to form microspheres, followed by succinoylation (Constantin et al., 2007).	Microspheres for oral delivery of anionic drugs.

Pullulan modifier agent	Modification	Application
Gelatin (via activator in DMSO)	Chemical reaction between modified pullulan and gelatin to form hydrogels (Han; Lv, 2019).	Nanogel for drug delivery.
Glycidyl trimethylammonium chloride and dimethylformamide sulfate	Dual modification: sulfation (negatively charged) and alkylation (positively charged) of pullulan (Dionísio et al., 2013).	Nanoparticles for transmucosal protein delivery.
Methacrylic anhydride	Methacrylation followed by UV-induced crosslinking to form hydrogels (Bae et al., 2011).	3D-printed hydrogels for tissue engineering.
Methacrylic anhydride	Methacrylation and UV-crosslinking to produce hydrogels (Mugnaini et al., 2021).	3D printing hydrogel.
Methacrylic anhydride and PEGDA (polyethylene glycol diacrylate)	Methacrylation and crosslinking with PEGDA under UV light (Della Giustina et al., 2019).	3D-printed hydrogel scaffolds for tissue engineering.
Methacrylic anhydride and PEGDA	Copolymerization of methacrylated pullulan and PEGDA to form hydrogels (Qin et al., 2021).	Hydrogels for cartilage repair and regeneration.
Methacrylic anhydride and beta-cyclodextrin	Methacrylation followed by conjugation with β-cyclodextrin and UV-crosslinking (Nonsuwan et al., 2023).	Hydrogels for curcumin-controlled release in wound healing.
Monochloroacetic acid.	Carboxymethylation of pullulan in isopropanol/NaOH medium (Bera et al., 2020).	ZnO-based nanocomposites for delivery of erlotinib (anti-cancer drug).

Pullulan modifier agent	Modification	Application
PVA (polyvinyl alcohol)	Emulsion crosslinking technique (Soni; Ghosh, 2017).	Controlled release of pirfenidone for pulmonary fibrosis.
Spermine	Chemical conjugation with pullulan in DMSO (Seki et al., 2008).	Enhancing pulmonary insulin absorption.
S. foetida	Water-in-oil emulsification and crosslinking with pullulan to produce microparticles (Hadke; Khan, 2021).	Microparticles for controlled release of amoxicillin.
2-(Butoxymethyl)oxirane	Grafting onto pullulan to create hydrophobic nanoparticles (Bostanudin et al., 2021).	Nanocarriers for percutaneous delivery.

To reduce its solubility and enhance its performance in drug delivery systems, pullulan can be either physically blended with other polymers (De Arce Velasquez et al., 2014; Göttel et al., 2020; Priyadarshi et al., 2021; Vishwanath et al., 2012) or chemically modified. The latter strategy, especially crosslinking and functional group modification, is more widely applied in biomedical fields. These include crosslinking agents such as epichlorohydrin or methacrylic anhydride as well as functionalization with charged or hydrophobic groups to adjust solubility, mechanical strength, and biofunctionality.

Among these strategies, methacrylation of pullulan using methacrylic anhydride (MA), first reported by Bae et al. (2011), has been extensively studied. This modification introduces methacrylate groups that can undergo UV-induced crosslinking to form hydrogels (Figure 1.5).

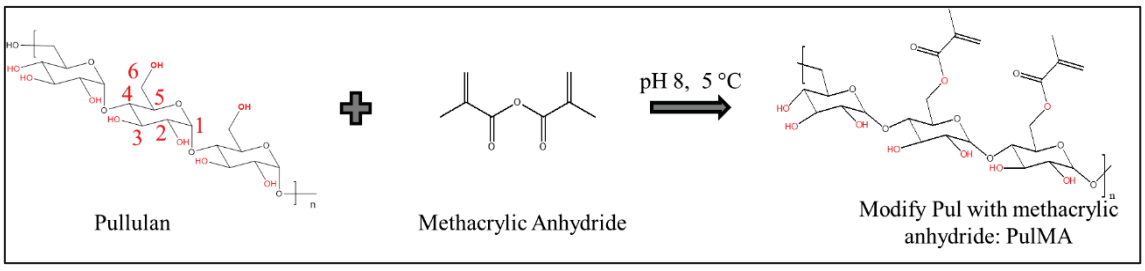

Figure 1.5 Reaction scheme of pullulan and methacrylic anhydride

The reaction is typically carried out in aqueous solution at pH 8 and 5 °C, where MA reacts preferentially with the hydroxyl group at the C6 position due to steric accessibility. The extent of substitution, or methacrylation degree, depends on the initial MA concentration and is generally quantified by ^{1}H-NMR analysis. However, the methodology for this quantification varies significantly between studies (Table 1.5), making direct comparison challenging.

Table 1.5 Methacrylation degree calculation and results of different references in the literature

Reference	Methacrylation degree calculation	Equation	Initial amount of MA	Methacrylation degree
(Bae et al., 2011)	The ratio between the area under the peaks 1.8-2.0, 5.7-5.9, and 6.1-6.3 (from methacrylate group), by the area under the peaks 3.3-4.1, 4.9-5.0, and 5.2-5.5 (from pullulan).	No provided.	0.25% (v/v)	3.6%
			0.5% (v/v)	6.4%
			1.50% (v/v)	16.5%
(Della Giustina et al., 2019)	Area under the peaks 1.85, 5.7–5.9, 6.1–6.3 ppm (I_{MA} corresponding to all the protons from methacrylic) divided by the area under the peaks 3.3–4.1, 4.8–5.0, 5.2–5.5 ppm (I_{Pul} is the integral of all pullulan protons).	$MD = 100 \cdot \frac{7 \cdot I_{MA}}{5 \cdot I_{Pul}}$	0.5% (v/v)	3.38%
(Mugnaini et al., 2021)	Area under the peak 1.90 ppm divided by the area under the peaks 4.02-3.35 ppm.	$FD = 6 \cdot \frac{I_{1.90\ ppm}}{I_{4.02-3.35\ ppm}}$	0.5% (v/v)	27%
(Qin et al., 2021)	Integral ratio between 5.71-6.28 double bond peak and 4.92-5.51 ppm pullulan backbone.	No provided.	54% (w/w)	10%
(Nonsuwan et al., 2023)	Area under the peaks 5.71-6.15, 5.25, and 5.56 ppm divided by the area under the peaks at 5.38-4.44 ppm (anomeric protons of pullulan).	No provided.	1.875% (w/v)	38.2%

Following modification, the methacrylated pullulan (PulMA) is typically dissolved in water or DMSO along with a photoinitiator, such as Irgacure 2959. Upon UV exposure, the photoinitiator generates radicals that initiate crosslinking via the methacrylate double bonds, forming a hydrogel network (Figure 1.6).

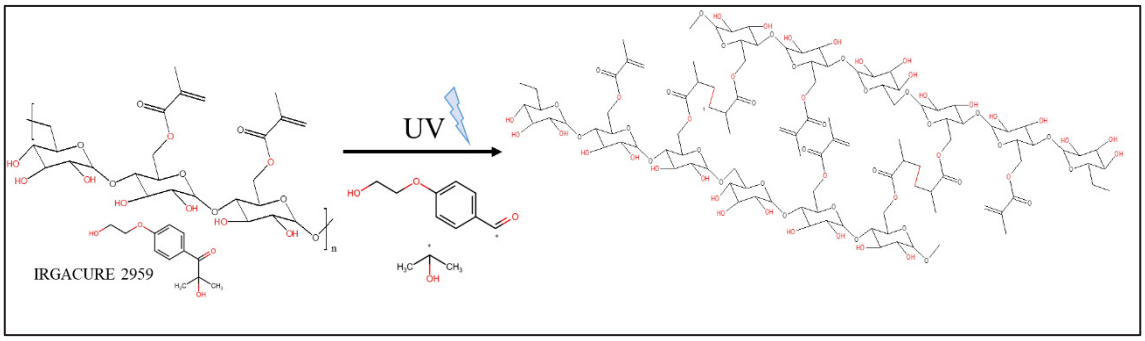

Figure 1.6 Reaction scheme of PulMA hydrogel

PulMA hydrogels have been explored primarily for tissue engineering and drug delivery systems. Key characterizations for these applications include swelling behavior, cytotoxicity, and cell adhesion. Swelling is directly related to the pore structure and crosslink density of the hydrogel, and it plays a crucial role in modulating drug release kinetics. Studies show that both the initial PulMA concentration and methacrylation degree inversely affect swelling, where more densely crosslinked networks swell less and consequently release less drug (Bae et al., 2011; Nonsuwan et al., 2023).

From a biological perspective, PulMA hydrogels are non-toxic, as demonstrated in multiple cytocompatibility studies (Bae et al., 2011; Nonsuwan et al., 2023; Qin et al., 2021). However, cell adhesion and proliferation on unmodified PulMA surfaces are typically low. This limitation can be addressed by incorporating adhesion-promoting biopolymers, such as GelMA (gelatin methacrylate), or by blending with proteins, as shown by Bae et al. (2011) and Della Giustina et al. (2019).

In summary, modifying pullulan with methacrylic anhydride provides a robust and tunable platform for developing hydrogels with tailored swelling, mechanical, and biological properties, suitable for use in advanced drug delivery systems and regenerative medicine.

CHAPTER 2

OBJECTIVES

Based on the findings presented in the literature review, the main objective of this work is to develop controlled drug delivery (DD) systems for tuberculosis treatment by investigating two distinct platforms for the release of isoniazid (INH): clay-based carriers and pullulan-based hydrogels. The specific objectives are:

1. To develop a clay-based drug delivery system, through:

    a. Characterizing clay physicochemical properties, including pore volume, to understand their influence on INH incorporation and release.

    b. Evaluation of process parameters such as pH and drug concentration, as well as the spatial distribution of INH within clay agglomerates, and how these factors affect the release profile.

    c. Investigation of the role of clay surface charge on INH adsorption and release dynamics.

2. To develop a pullulan-based hydrogel system, through:

    a. Assessment of the reproducibility of the pullulan modification reaction under laboratory-scale conditions.

    b. Analysis of hydrogel rheological properties, particularly crosslinking density and UV exposure time, to understand their effects on gel structure.

    c. Evaluation of hydrogel swelling behavior and the corresponding INH release kinetics.

CHAPTER 3

METHODOLOGY

This chapter describes the experimental procedures and techniques employed to achieve the objectives of this study. It is organized into three main parts. The first section presents the materials used throughout the project. The second details the characterization techniques applied to evaluate the physical and chemical properties of the selected materials. The third section outlines the experimental protocols used to develop the drug delivery systems, divided into two parts: (i) the preparation and testing of clay-based systems for isoniazid (INH) adsorption and release, and (ii) the chemical modification of pullulan, hydrogel formation, and evaluation of its performance as an INH delivery platform.

To address the objectives of this thesis, two complementary methodological approaches were followed: one centered on clay-based carriers and the other on pullulan-based hydrogels. Methodology 1 investigates clays as potential vehicles for the controlled release of isoniazid (INH), including the analysis of physicochemical properties (Chapter 4), the effects of environmental and process parameters such as pH and drug concentration (Chapter 5), and the role of surface charge in drug-clay interactions (Chapter 6). Methodology 2 focuses on the development of a hydrogel system based on chemically modified pullulan, covering the reproducibility of the modification process, the analysis of rheological behavior (e.g., crosslinking density and UV exposure time), and the evaluation of swelling and drug release performance (Chapter 7).

The schematic (Figure 3.1) visually summarizes how each methodological path is linked to the thesis objectives and how the corresponding experimental chapters contribute to the development of robust INH delivery systems.

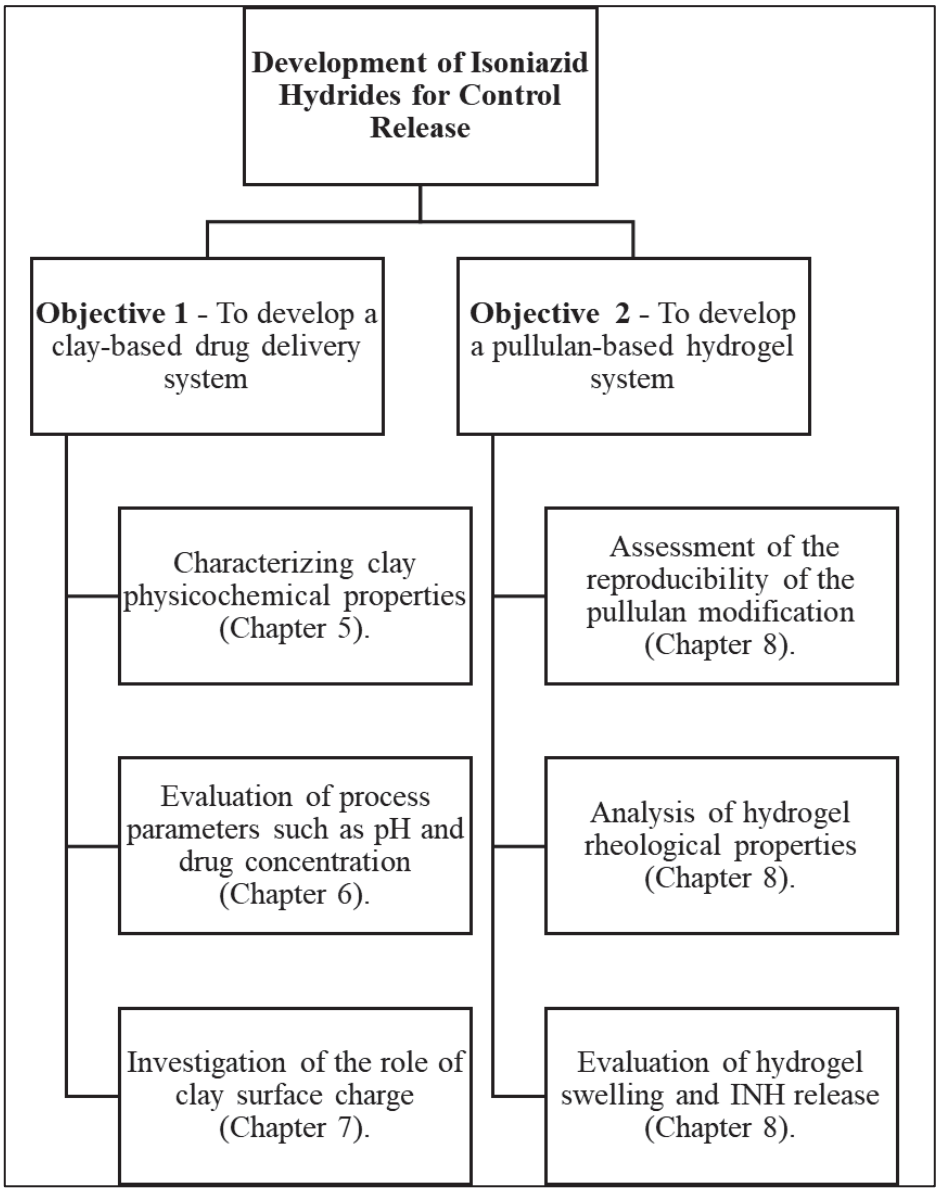

Figure 3.1 Methodological framework for the development of isoniazid delivery systems, highlighting the experimental steps and corresponding thesis chapters for each approach

3.1 Materials

Isoniazid (INH), sodium phosphate ($NaHPO_4$), sodium chloride (NaCl), sodium hydroxide (NaOH), and hydrochloric acid (HCl, 37% solution) were purchased from Sigma-Aldrich (USA) and used without further purification. Dimethyl sulfoxide (DMSO) (99.9%), IRGACURE 2949, a UV-sensitive photoinitiator, and methacrylic anhydride, used to chemically modify pullulan by introducing crosslinkable methacrylate groups, were also

obtained from Sigma-Aldrich. Ethyl alcohol anhydrous from commercial alcohols (Canada).

Details of the clay samples used in this study are presented in Table 3.1. Cloisite® and Laponite® are commercial smectite clays kindly supplied by BYK Additives and Instruments (Germany). The remaining samples are natural, unmodified clays. To obtain the VR, VVm, and VVd samples, a raw smectite from the northeastern region of Brazil (Vitória da Conquista, Bahia) was used. The clay was dispersed in water (15% w/w) and homogenized at 14,000 rpm for 20 minutes. After resting, the dispersion spontaneously separated into three visually distinct phases, which were carefully collected and labeled as VR, VVm, and VVd (de Carvalho Arjona et al., 2024; Silva-Valenzuela et al., 2018).

Table 3.1 Clay Samples Used in This Study: Acronym, Name, Type, and Country of Origin

Acronym	Name	Type	Country / Supplier
CL	Cloisite	Natural clay	United States / BYK Additives and Instruments
LP	Laponite	Synthetic clay	United States / BYK Additives and Instruments
VL	Verde Lago	Raw clay	Argentina
VC	Verde Claro	Raw clay	Brazil
VR	Verde Rosa	Raw clay	Brazil
VVm	Verde Vermelho	Raw clay	Brazil
VVd	Verde Verde	Raw clay	Brazil

Pullulan (food grade, $M_n \approx 134{,}000$ g/mol, Mw ≈ 807,000 g/mol), a water-soluble and biodegradable polysaccharide commonly used in biomedical applications, was provided by Nagase (Japan).

3.2 Characterization Techniques

This section presents the characterization techniques employed throughout the development of the drug delivery systems proposed in this work. Some techniques were applied across multiple stages of the study to ensure methodological consistency, while others were used in specific steps depending on the material or objective. To facilitate the reader's understanding of when and why each technique was used, Table 3.2 provides a

summary of the techniques, their purposes, and the corresponding chapters in which they were applied.

Table 3.2 Characterization techniques used in this study, with their respective purposes and chapters of application

Characterization Techniques	Chapter 4	Chapter 5	Chapter 6	Chapter 7
XRD	Used to analyze the mineralogical composition of clays and evaluate INH incorporation and structural changes after drug loading.	Evaluate INH incorporation	Evaluate INH incorporation	–
XRF	Determine the elemental composition of pristine clays and chemical analysis.	–	–	–
ICP-OES	Quantify Pb and Cd content.	–	Quantify Pb, Cd, and Li content	–
N_2 Adsorption/ Desorption	Determine clay's surface area, pore volume, and pore type.	–	–	–
FTIR	Identify shifts in vibrational modes due to interactions between INH and clay.	Identify shifts in vibrational modes due to INH-clay interactions	Identify changes in vibrational modes of certain bonds due to interactions	Confirm chemical modification of pullulan after reaction with methacrylic anhydride
TGA	Assess the thermal stability and mass loss of pristine clay and hybrid to verify INH incorporation	Evaluate mass loss to confirm INH incorporation into hybrids	Evaluate the mass loss of pristine clay and hybrid	Assess thermal decomposition of pullulan, PulMA films, and hydrogels
Zeta Potential	Evaluate the surface charge of VVd at pH 2 and 7.	Evaluate surface charge of CL and LP at pH 2 and 7	–	–

Characterization Techniques	Chapter 4	Chapter 5	Chapter 6	Chapter 7
UV-Vis Spectrophotometry	Quantify INH in adsorption and release tests.	Quantify INH in adsorption and release tests.	Quantify INH in adsorption and release tests.	Quantify INH released from hydrogels
^{1}H NMR	–	–	–	Confirm the degree of pullulan modification with methacrylic anhydride.
Rheology	–	–	–	Analyze UV-light exposure time and crosslinking density to evaluate hydrogel structure.
Swelling Test	–	–	–	Determine swelling behavior and INH release capacity of pullulan-based hydrogels.
UV-vis spectroscope	Measure the amount of INH intake and release by clays.	Measure the amount of INH intake and release by clays.	Measure the amount of INH intake and release by clays.	Measure the amount of INH release by hydrogels.

This structure allows the reader to follow the logical flow of the experimental design and its connection to the thesis objectives. It also highlights the scientific rigor of the work: the techniques used in Chapters 4, 5, and 6 support already published results. Chapter 7 presents new, unpublished data that builds on previous findings and highlight directions for future research. The results are being prepared for manuscript submission.

The detailed parameters and experimental conditions for each technique are described in the following subsections.

3.2.1 X-ray Diffraction (XRD)

The mineralogical composition of clay particles was determined by X-ray diffraction (XRD) using a Malvern Panalytical Empyrean DY-2516 diffractometer equipped with a Cu Kα radiation source. For structural identification, scans were recorded in the 2θ range of 2.5°–90° at a step size of 0.004°/min. Crystalline phases were identified by comparison with standard patterns from the International Centre for Diffraction Data (ICDD) and the Inorganic Crystal Structure Database (ICSD).

To assess whether INH was intercalated into the interlayer space of clays, additional XRD scans were performed in the 2θ range of 3°–30° at a step size of 0.013°/min.

3.2.2 X-ray Fluorescence (XRF)

Quantitative chemical analysis of pristine clays was performed by X-ray fluorescence (XRF) using a Zetium Malvern Panalytical instrument. Lithium tetraborate-fused pellets were used to assess the major oxides present, including SiO_2, Al_2O_3, Fe_2O_3, MnO, MgO, CaO, Na_2O, K_2O, TiO_2, and P_2O_5. The loss on ignition (LOI) was measured by gravimetric analysis after heating at 1020 °C for 2 hours, as described by Ulsen et al. (2019).

3.2.3 Inductively Coupled Plasma Optical Emission Spectroscopy (ICP-OES)

Trace elemental analysis of Pb and Cd in clay samples was conducted using an iCAP 6300 Duo ICP-OES system (Thermo Scientific), following multi-acid digestion.

3.2.4 Nitrogen Adsorption/Desorption (N_2 Isotherms)

Specific surface area and pore structure were evaluated via low-pressure N_2 adsorption/desorption isotherms at 77 K using a Micromeritics ASAP 2020 Plus system. Measurements were recorded over a relative pressure range of P/Po = 0.05–1.0 (Shah et al., 2013). Surface area was calculated using the BET method; pore volume and pore diameter were derived from the BJH model (David Avnir & Mieczyslaw Jaroniec, 1989). Pore types were interpreted based on isotherm shapes (Sing et al., 1985). Before analysis, samples were oven-dried at 90 °C for 48 hours, stored in vacuum desiccators for 3 days, and degassed at 200 °C for 12 hours.

3.2.5 Fourier Transform Infrared Spectroscopy (FTIR)

FTIR spectra were recorded using a PerkinElmer Spectrum Two spectrometer to analyze the interaction between INH and clay and to confirm pullulan modification. Spectra were acquired in the 4000–600 cm^{-1} range with a resolution of 4 cm^{-1} and 10 scans.

3.2.6 Thermogravimetric Analysis (TGA)

TGA was carried out using a Pyris Diamond TG/DTA analyzer (PerkinElmer). Mass loss was measured under an air flow of 100 mL/min, from 40 to 800 °C for clays and INH-clay hybrids, and from 40 to 600 °C for pure INH. The heating rate was 10 °C/min.

3.2.7 Differential Scanning Calorimetry (DSC)

DSC measurements were performed with a DSC 2500 TA Discovery instrument under a nitrogen atmosphere (50 mL/min). Samples were sealed in hermetic aluminum pans and heated from 40 to 230 °C at a rate of 10 °C/min.

3.2.8 Zeta Potential

The surface charge of CL, LP, and VVd was measured using a Malvern Zetasizer Nano system. Dispersions (0.1% w/v) were prepared at pH 2 and 7, then sonicated for 10 minutes. For each clay, three independent aliquots were measured, and each was tested in triplicate.

3.2.9 ^{1}H Nuclear Magnetic Resonance (^{1}H-NMR)

^{1}H NMR analysis was performed to confirm the modification of pullulan by methacrylic anhydride. Samples were dissolved in deuterium oxide (D_2O) at 0.8 mg/mL, and spectra were recorded using a Bruker Ultrashield 300 (300 MHz) spectrometer.

3.2.10 Rheological Analysis

Rheological measurements were performed using an Anton Paar Physica MCR 301 rheometer with a plate-plate geometry (gap: 0.1 mm, strain: 1%, frequency: 1 rad/s). PulMA

solutions (10% and 20% w/v) were analyzed in the linear viscoelastic range. A UV lamp (λ = 360 nm) was used to initiate crosslinking, and changes in the storage (G′) and loss (G″) moduli were monitored over 15 minutes. An additional set of samples (0.5% w/v PulMA) was exposed to UV for 1 or 10 minutes, followed by rheological testing to assess post-exposure effects. All experiments were conducted in triplicate.

3.2.11 Hydrogel Swelling Test

Swelling behavior was assessed by immersing dried hydrogels in phosphate buffer (pH 7.4) for 24 hours. The samples were air-dried for 48 hours, weighed (W_d), and then submerged in the buffer. After 24 hours, swollen weights (W_s) were recorded. The swelling ratio was calculated using the equation (3.1), and all measurements were performed in triplicate.

$$Swelling\ ratio\ (\%) = \frac{W_s - W_d}{W_d} \cdot 100 \tag{3.1}$$

3.2.12 Ultraviolet Spectroscopy (UV-vis)

UV-Vis spectroscopy was employed to quantify the concentration of isoniazid (INH) in adsorption and release studies from both clays and pullulan-based hydrogels. All measurements were performed using an Agilent Cary 60 UV-Vis spectrophotometer. To ensure accurate quantification across different pH environments, four calibration curves were generated based on the absorbance of INH at varying concentrations and wavelengths, depending on the solution pH. These curves were used to correlate absorbance (Abs) with INH concentration (C) for each experimental condition. The calibration equations (equations (3.2), (3.3), (3.4), and (3.5)), their respective wavelengths, and corresponding pH values are presented in Table 3.3.

Table 3.3 Calibration curves used for INH quantification at different pH levels and wavelengths

INH solution	Wavelength (nm)	Calibration Curve Equation	Equation Label
Deionized water	263	$Abs = 3.820 \cdot C, R^2 = 1.000$	(3.2)
pH 2.0 (buffer)	265	$Abs = 4.783 \cdot C, R^2 = 0.999$	(3.3)
pH 6.8 (buffer)	261	$Abs = 3.631 \cdot C, R^2 = 0.999$	(3.4)
pH 7.4 (buffer)	261	$Abs = 3.511 \cdot C, R^2 = 0.999$	(3.5)

3.3 Experimental Protocols

3.3.1 Clay Pre-Treatment And Fraction

As previously described, the VR, VVm, and VVd samples were obtained from a raw smectite clay sourced from the northeastern region of Brazil (Vitória da Conquista, Bahia). The raw clay was dispersed in deionized water at 15% (w/w) and homogenized using a high-shear mixer at 14000 rpm for 20 minutes to form a uniform suspension.

After resting undisturbed, the dispersion spontaneously separated into three visually distinct phases, which were carefully decanted and collected. These fractions were labeled as VR, VVm, and VVd, based on their coloration and settling behavior (De Carvalho Arjona et al., 2024; Silva-Valenzuela et al., 2018). To ensure phase stability, each fraction was gently stirred at 1500 rpm and allowed to rest overnight. No further visible separation occurred, confirming the reproducibility of the fractionation process.

Following separation, each clay fraction was dried at 60 °C, ground, and passed through a 200-mesh sieve to ensure uniform particle size. The processed samples were then stored in sealed containers at room temperature until further use.

3.3.2 Adsorption Kinetic Studies

Adsorption experiments were conducted to evaluate the isoniazid (INH) uptake over time by various clay samples. Each test was performed in triplicate. In each experiment, 25 mL of a 4% (w/w) aqueous dispersion of the clay sample was stirred magnetically at 1550 rpm

for 15 minutes. Subsequently, 25 mL of an aqueous INH solution (0.02 mol/L) was added. This concentration was selected to remain below the estimated monolayer adsorption capacity of smectites, as suggested by Carazo et al. (2018b). The mixtures were stirred for six-time intervals: 0.75, 1.5, 3, 6, 12, and 24 hours, to determine the equilibrium time for INH adsorption. At the end of each interval, the samples were centrifuged at 5000 rpm in a Sorvall ST 16 ThermoScientific centrifuge, and the supernatant was analyzed using UV-Vis spectroscopy. The remaining solid was dried at 60 °C and stored for further analysis (XRD, FTIR, and TGA).

The amount of incorporated INH per gram of clay (n_{ab}) was calculated based on the difference between the initial INH concentration (Q_i) and the residual concentration in the supernatant (Q_m), as shown in equation (3.6), both were measured by a UV-vis spectrometer.

$$n_{ab} = \frac{Q_i - Q_m}{m} \tag{3.6}$$

To assess the kinetics of INH adsorption onto the clay particles, the experimental data were fitted to three kinetic models: pseudo-first order (PFO), pseudo-second order (PSO), and adsorption-diffusion model (ADM) given by the equations (1.4), (1.5), and (1.6), respectively.

3.3.3 Clay Drug Adsorption Isotherms

Adsorption isotherm experiments were performed using three clay samples: Cloisite® (CL), Laponite® (LP), and VVd. Tests were conducted at two pH levels (pH 2 and pH 7) to evaluate the influence of acidity on drug–clay interactions. A fixed amount of dry clay (0.1 g) was enclosed within a cellulose dialysis membrane (cut-off: 14,000 Da) and immersed in 10 mL of INH solutions with varying concentrations ranging from 68.5 to 3082.5 mg/L (0.5 to 22.5 mmol/L).

The systems were stirred magnetically for 3 hours, based on the equilibrium time determined in kinetic studies (de Carvalho Arjona et al., 2024). Following incubation, the residual INH concentration in the solution was quantified using UV-Vis spectroscopy, referencing the appropriate calibration curves at each pH (see (3.2) and (3.3)).

The amount of INH incorporated per gram of clay (n_{ab}) was calculated using equation (3.6), as previously described. Experimental isotherm data were expressed as n_{ab} versus C_e, where C_e represents the equilibrium concentration of INH in solution. The resulting curves were fitted to the Langmuir and Freundlich isotherm models using nonlinear regression, based on the minimization of the sum of squared residuals (SSR) for each model.

Model fitting accuracy was evaluated by calculating the sum of squared residuals (SSR), defined as equation (3.7). Where $q_{i,exp}$ and $q_{i,model}$ are, respectively, the experimental and model-predicted adsorption values:

$$SSR = \sum_{i=1}^{m} \left(q_{i,exp} - q_{i,model}\right)^2 \quad (3.7)$$

For the Langmuir model, the separation factor (R_L) was also calculated (3.8) to assess the favorability of the adsorption process at each pH. Where Qm is the theoretical maximum adsorption capacity (mmol/g) and K_L is the Langmuir constant related to adsorption affinity (L/mmol):

$$R_L = \frac{1}{1+Q_m K_L} \quad (3.8)$$

3.3.4 Kinetic Drug Release Test

Two different INH release protocols were developed to assess the drug release kinetics from clay–INH hybrids and pullulan hydrogels:

1. Single-pH exposure test: Samples were immersed in a buffer of fixed pH to evaluate release under constant environmental conditions. For clay-based systems, the test duration was set to 5 hours, while for pullulan hydrogels, release was monitored for 8 hours to assess the influence of pH on the release profile.

2. Simulated gastrointestinal (GI) release test: A sequential pH-shift protocol was implemented to simulate oral drug delivery. The sample was immersed for 2 hours in pH 2.0 buffer (gastric environment), followed by 2 hours in pH 6.8 buffer (proximal small intestine), and finally 4 hours in pH 7.4 buffer (distal small intestine), for a total of 8 hours (480 minutes).

In both protocols, 100 mg of clay–INH hybrid or pullulan hydrogel was placed inside a cellulose dialysis membrane (molecular weight cut-off: 14,000 Da). The dialysis bags were immersed in 50 mL of the appropriate buffer solution under magnetic stirring. The release medium was sampled after 10 minutes, and subsequently at 30-minute intervals. After each withdrawal, the volume was maintained constant by replenishing with fresh buffer.

Buffer solutions were prepared based on the formulation by Almeida et al. (2019), as follows:

- pH 2.0: 1 g NaCl + 0.5 mL HCl in 1000 mL deionized water.
- pH 6.8: 0.4 g NaOH + 2.0 g $NaH_2PO_4 \cdot H_2O$ + 3.1 g NaCl in 1000 mL deionized water.
- pH 7.4: pH 6.8 solution adjusted with 2.5 mol/L NaOH.

All experiments were conducted in triplicate.

3.3.4.1 Similarity Factor (f_2) Comparison

To compare the release profiles of different clays, the similarity factor (f_2) was calculated using equation (3.9). This metric evaluates the closeness between two dissolution curves and is widely accepted by the FDA and EMA for pharmaceutical comparison. Two profiles are considered similar when f_2 lies between 50 and 100 (Muselík et al., 2021; Tekmen et al., 2006).

$$f_2 = 50 \cdot log\left\{\left[1 + \frac{1}{n}\sum_{t=1}^{n}(C1_t - C2_t)^2\right]^{-0.5} \cdot 100\right\} \quad (3.9)$$

Where:

- C_{1t}, C_{2t} = percentage of drug released at time t from systems 1 and 2
- n = number of time points sampled

3.3.4.2 Mathematical Modeling of Release Kinetics

The experimental release data were fitted to three commonly used drug release models to describe the release mechanism: zero order model (1.1), Higuchi model (1.2), and Korsmeyer–Peppas model (1.3).

3.3.5 In Vitro Cytotoxicity Assays

In vitro assays were performed by the students of Professor Dayane Tada at the Universidade Federal de São Paulo (UNIFESP) to assess the cytotoxicity of the VVd clay and its corresponding INH-loaded hybrid (VVd–INH). The tests were conducted using L929 fibroblast cells following the indirect contact method outlined in ISO 10993-5:2009.

Sample extracts were prepared in Dulbecco's Modified Eagle Medium (DMEM), supplemented with 10% fetal bovine serum (FBS), by suspending the powders at a concentration of 0.2 g/mL, as recommended by ISO 10993-12:2007 for irregularly shaped powder materials. Cell culture medium without any sample served as the negative control and was maintained under the same incubation conditions.

L929 cells were seeded at a density of 0.25×10^4 cells/well in 96-well plates containing DMEM supplemented with 10% FBS (v/v), 0.1 g/L streptomycin, and 0.025 g/L ampicillin. After reaching 80% confluence, cells were exposed to the extracts and incubated for 24 hours at 37 °C in a humidified atmosphere with 5% CO_2.

Cell viability was assessed using the MTT assay. After incubation, the medium was aspirated, and each well was rinsed with phosphate-buffered saline (PBS, pH 7.0). Then, 100 µL of MTT solution (0.5 mg/mL in PBS) was added to each well. The cells were incubated for 3 hours to allow for formazan crystal formation. Subsequently, the MTT solution was replaced with 100 µL of DMSO to solubilize the crystals. After 30 minutes of

gentle shaking, absorbance was measured at 480 nm using a microplate reader (BioTek Synergy 2).

Cell viability (%) was calculated using (3.10), with the absorbance of the negative control (untreated cells) considered as 100% viability. Where Abs_{sample} is the absorbance at 480 nm for sample-treated cells and $Abs_{control}$ is the average absorbance at 480 nm for negative control wells.

$$Cell\ Viability\ (\%) = \frac{Abs_{sample}}{Abs_{control}} \cdot 100 \tag{3.10}$$

The assay was performed in quintuplicate.

L929 fibroblasts were chosen due to their widespread use in biocompatibility testing, as recommended by ISO 10993 standards. Their rapid proliferation and consistent response facilitate reproducible and comparative assessments. Moreover, as fibroblasts are involved in tissue remodeling and wound healing, their use is relevant for evaluating materials intended for tuberculosis-related applications, which may involve inflammatory and fibrotic tissue environments.

3.3.6 Pullulan Modification

Pullulan was chemically modified with methacrylic anhydride (MA) following the procedure described by Bae et al. (2011), with minor adaptations. To verify reproducibility, the reaction was performed in triplicate.

Initially, pullulan was dissolved in a pH 8.0 phosphate buffer and left under constant stirring at room temperature for approximately 24 hours. The solution was then cooled in an ice bath for 1 hour, reaching a temperature of approximately 5 °C. Following this, the desired volume of methacrylic anhydride was added dropwise under continuous stirring.

The pH was monitored hourly and maintained at 8.0 using a 2.5 mol/L NaOH solution when necessary to adjust the solution pH level. The reaction was considered complete when the pH stabilized at 8.0 over two consecutive measurements. The concentration of MA and the corresponding reaction times are shown in Table 3.4.

Table 3.4 Conditions of pullulan modification reactions and corresponding sample labels

Amount of MA (v/v)	Reaction time (hours)	Modified pullulan name
0.5%	15 ± 1	PulMA 0.5%
1.5%	35 ± 4	PulMA 1.5%
3.0%	49 ± 2	PulMA 3.0%

After the reaction was completed, the PulMA solution was dried under vacuum at room temperature. The resulting film was then dissolved in DMSO at 18% (w/v) and stirred for 24 hours. This solution was slowly precipitated in cold ethanol (10:1 (v/v)), and the precipitated product was subsequently dried under vacuum. The precipitation and drying steps were repeated once to improve purification. The final product was dialyzed against distilled water for five days to remove residual DMSO and ethanol, followed by vacuum drying at room temperature to form casting films. These films were characterized by FTIR and ^{1}H-NMR analyses.

3.3.7 Pullulan-Based Hydrogels

Hydrogels were synthesized from each PulMA formulation using a standardized photopolymerization method. PulMA was dissolved in deionized water under magnetic stirring for 6 hours to obtain 10% and 20% (w/v) solutions. Subsequently, 1% (w/w) of the photoinitiator IRGACURE 2949 was added, and the mixture was stirred for an additional 12 hours to ensure homogeneity.

Aliquots of 0.2 mL of each PulMA solution were then cast into Petri dishes and exposed to UV light (λ = 365 nm) for 15 minutes. The resulting hydrogels were left to air dry at room temperature for at least 48 hours, until their weight stabilized. To calculate the hydrogels' crosslinking density (δ_{cros}), the rubber elasticity theory was used, (3.11). Where G' is the storage modulus (Pa), R is the universal gas constant, and T is the temperature (K).

$$\delta_{cros} = \frac{G'}{R \cdot T} \tag{3.11}$$

3.3.8 INH Loaded Pullulan-Based Hydrogels

INH was incorporated into the pullulan hydrogels following the same procedure described in Section 3.3.7, with the addition of isoniazid directly into the PulMA solution before photo crosslinking. A drug loading ratio of 1% and 5% (w/w) relative to the total polymer mass was used. The INH-loaded solution was then processed under identical conditions to form drug-loaded hydrogels.

3.3.9 Additional Experiments Consideration

Negative controls were included in all experimental designs to ensure proper baseline comparisons. In release tests, unloaded clay and hydrogel samples were used under identical conditions. For cytotoxicity assays, both unloaded VVd and INH alone were evaluated alongside the VVd–INH hybrid. Blank matrices were also characterized separately by FTIR, TGA, XRD, and swelling tests to isolate material behavior from drug-related effects.

Statistical analysis of quantitative results was performed using ANOVA ($p < 0.01$) single factor, with data processed in Microsoft Excel. All experiments were conducted in triplicate or quintuplicate and reported as mean ± standard deviation.

While INH degradation was not directly monitored, UV-Vis scans showed no shift in the absorbance spectrum during testing, and all incorporation and release samples were analyzed on the same day to minimize degradation risks. UV-Vis calibration curves were validated within their linearity range using Agilent software.

To ensure reproducibility, all pullulan modifications were synthesized in triplicate and characterized individually via ^{1}H NMR, FTIR, and swelling analysis. All hybrid and polymeric samples were stored in airtight containers at –15 °C and protected from light prior to testing.

CHAPTER 4

INFLUENCE OF SMECTITE CLAY'S PORE VOLUME ON ISONIAZID ADSORPTION AND RELEASE

Jessica de Carvalho Arjona[a], Carina Ulsen[b], Francisco Rolando Valenzuela-Diaz[c], Nicole Raymonde Demarquette[d],

[a,c]Departamento de Engenharia Metalúrgica e de Materiais, Escola Politécnica, Universidade de São Paulo, Av. Professor Mello Moraes, 2463, São Paulo, SP 05508-030, Brazil
[a,d]Mechanical Engineering Department, École de Technologie Supérieure, 1100 R. Notre Dame O, Montréal, QC H3C 1K3, Canada
[b]Departamento de Engenharia de Minas e de Petróleo, Escola Politécnica, Universidade de São Paulo,Av. Prof. Mello Moraes, 2373, São Paulo, SP 05508-030, Brazil

Paper published in *Applied Clay Science*, May 2024

4.1 Introduction

This chapter is based on the work published in Applied Clay Science (de Carvalho Arjona et al., 2024) and addresses the first research objective: to develop a clay-based drug delivery system, through characterizing clay physicochemical properties, including pore volume, to understand their influence on INH incorporation and release.

In general, drug adsorption onto clays involves the diffusion of molecules across the particle surface, migration into internal pores, and interaction with functional sites. These interactions may occur through cation exchange in the interlamellar regions, resulting in increased basal spacing, or via hydrogen bonding and van der Waals forces in the inter-tactoid voids. While such mechanisms are well documented (Reinholdt et al., 2013; Tan & Hameed, 2017; Zhu et al., 2016), the role of clay pore volume in controlling drug release remains underexplored in pharmaceutical applications. Most prior investigations have focused on gas adsorption in shale materials (Feng et al., 2018; X. Wang et al., 2020).

In this chapter, we demonstrate that pore volume significantly affects INH release kinetics, suggesting that this often-overlooked property should be considered in the rational design of clay-based drug delivery systems (Kiaee et al., 2022).

4.2 Results and Discussion

4.2.1 Clay Sample Characterization

The chemical composition and mineralogical profiles of the seven clay samples used in this study are summarized in Table 4.1. All samples are based on smectite clays, with accessory minerals such as kaolinite, quartz, calcite, albite, and gibbsite present in the natural raw samples. Among them, VL, VC, VR, VVm, and VVd showed variable accessory mineral content, while the commercial clays, Cloisite® (CL) and Laponite® (LP), were comparatively purer.

LP presented the most distinct chemical composition, consistent with its classification as a synthetic clay of the hectorite group (BYK Additives & Instruments, 2014). Unlike montmorillonite, which is rich in Al_2O_3 and Fe_2O_3, hectorite has a predominance of MgO in the octahedral sheet, partially substituted by Li_2O (Brigatti et al., 2006). This structural difference explains the significantly lower Al_2O_3 and Fe_2O_3 contents observed in LP. Importantly, all clay samples exhibited minimal levels of potentially toxic elements such as Mn, Ti, P, Pb, and Cd, supporting their suitability for biomedical applications, particularly in drug delivery systems.

Table 4.1 Clay mineral phases, oxide composition, and pore volumes of the studied clay samples

Analyte	**CL**	**LP**	**VL**	**VC**	**VR**	**VVm**	**VVd**
Clay minerals	Smectite	Smectite	Smectite, kaolinite, quartz, calcite	Smectite, quartz, albite, gibbsite	Smectite, kaolinite	Smectite, kaolinite	Smectite, kaolinite
SiO_2 (%)	59.50	58.30	61.60	56.20	55.20	56.10	56.20
Al_2O_3 (%)	21.30	0.11	19.00	19.30	24.10	21.10	21.10
Fe_2O_3 (%)	4.24	<0.10	4.61	6.03	6.41	7.94	7.94
MnO (%)	<0.10	<0.10	<0.10	<0.10	<0.10	<0.10	<0.10
MgO (%)	2.37	27.20	3.01	2.31	3.23	3.80	3.60
CaO (%)	0.47	0.14	1.31	3.49	0.19	0.23	0.21
Na_2O (%)	3.84	2.93	3.06	0.24	0.11	<0.10	<0.10
K_2O (%)	<0.10	<0.10	0.40	0.90	<0.10	<0.10	<0.10
TiO_2 (%)	0.12	<0.10	0.31	0.65	0.11	0.22	0.75
P_2O_5 (%)	<0.10	<0.10	<0.10	<0.10	<0.10	<0.10	<0.10
Ignition loss (%)	7.03	11.00	6.15	10.70	10.90	10.30	10.30
Pb (ppm)	52	1	40	54	36	33	33
Cd (ppm)	<6	<6	<6	<6	<6	<6	<6

The N_2 adsorption–desorption isotherms of the seven samples are shown in Figure 4.1. In each graph, the quantity of nitrogen adsorbed by each sample is in function of its relative pressure. All clays exhibited type IV isotherms, indicative of mesoporous materials, as evidenced by the observed hysteresis loops. Monolayer adsorption was achieved at a relative pressure (P/Po) near 0.2, followed by multilayer adsorption and capillary condensation occurring above P/Po = 0.4 (Sing et al., 1985).

Analysis of the hysteresis loops revealed distinct pore morphologies. LP exhibited a type H2 hysteresis loop, suggesting the presence of ink-bottle-shaped pores, typically associated with pore-blocking or complex pore networks. In contrast, all other clays displayed type H3 hysteresis, characteristic of aggregates of plate-like particles forming slit-shaped pores

(Sing et al., 1985). This morphological distinction aligns with the structural difference between synthetic LP and the natural smectite-based clays.

According to IUPAC classification, the presence of macropores significantly alters the tail of the isotherm (Sing et al., 1985). Curves without macropores remain nearly horizontal at high relative pressures, whereas curves with a broad distribution of macropores exhibit a steep rise near P/Po ≈ 1. The curves observed here suggest that the clays are predominantly mesoporous, with micropores contributing to the low-pressure region (P/Po < 0.35) and macropores appearing above P/Po > 0.95 (Chang et al., 2022; Shah et al., 2018).

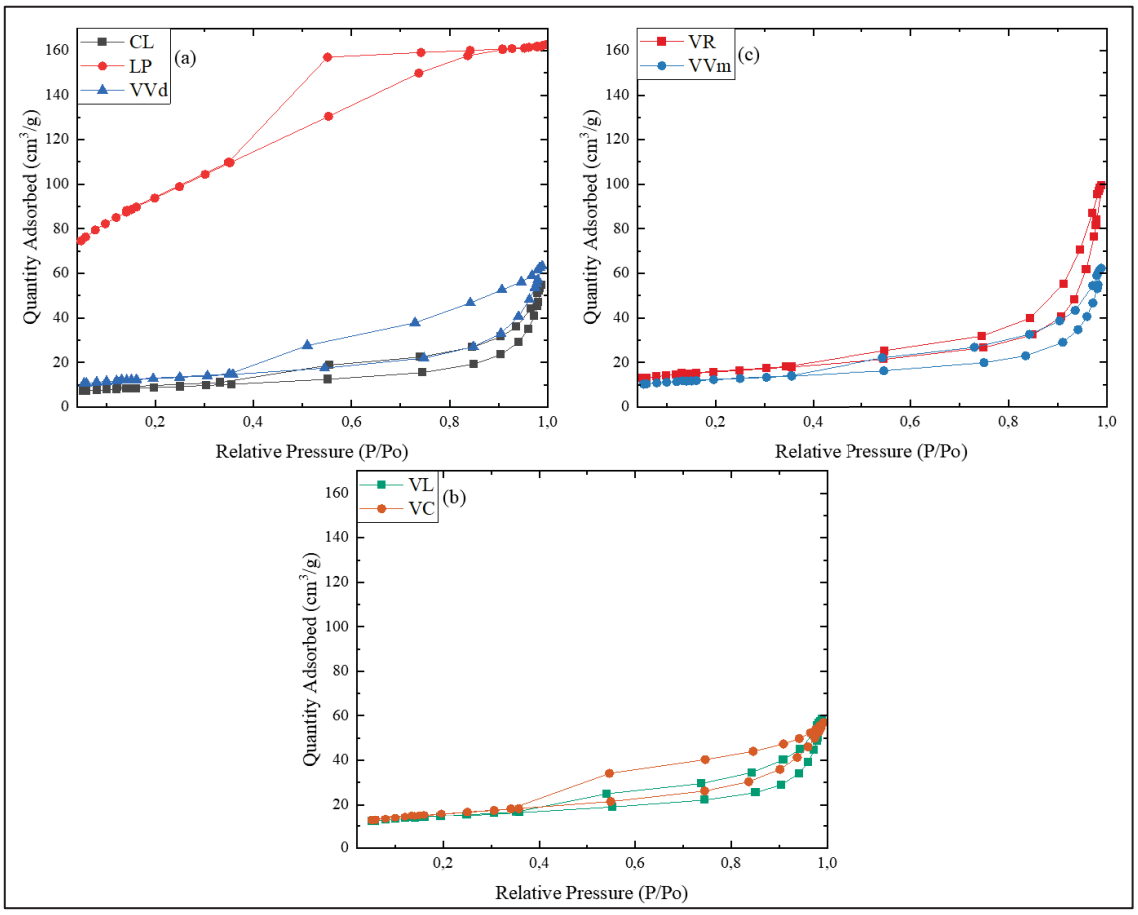

Figure 4.1 N_2 adsorption/desorption curves of the seven clays used in this work

4.2.2 Kinetics Adsorption Studies

Figure 4.2 shows the kinetic profiles of INH adsorption onto the six clay samples evaluated. The graph shows the INH mass adsorbed by clay in mg/g over time. In all cases, adsorption

approached a plateau after approximately 3 hours, confirming that the 24-hour adsorption period selected for subsequent experiments was more than sufficient to reach equilibrium. This kinetic behavior aligns with previous studies (Esperanza Carazo et al., 2018; Damasceno Junior et al., 2019; Souza et al., 2021). Despite the non-purified nature of most clay samples, triplicate experiments exhibited low standard deviations, indicating consistent adsorption behavior across replicates.

The adsorption capacity varied significantly depending on the clay, ranging from approximately 15 mg/g for Laponite® (LP) to 47 mg/g for the VVd sample. These results suggest a clear influence of clay physicochemical properties on INH uptake.

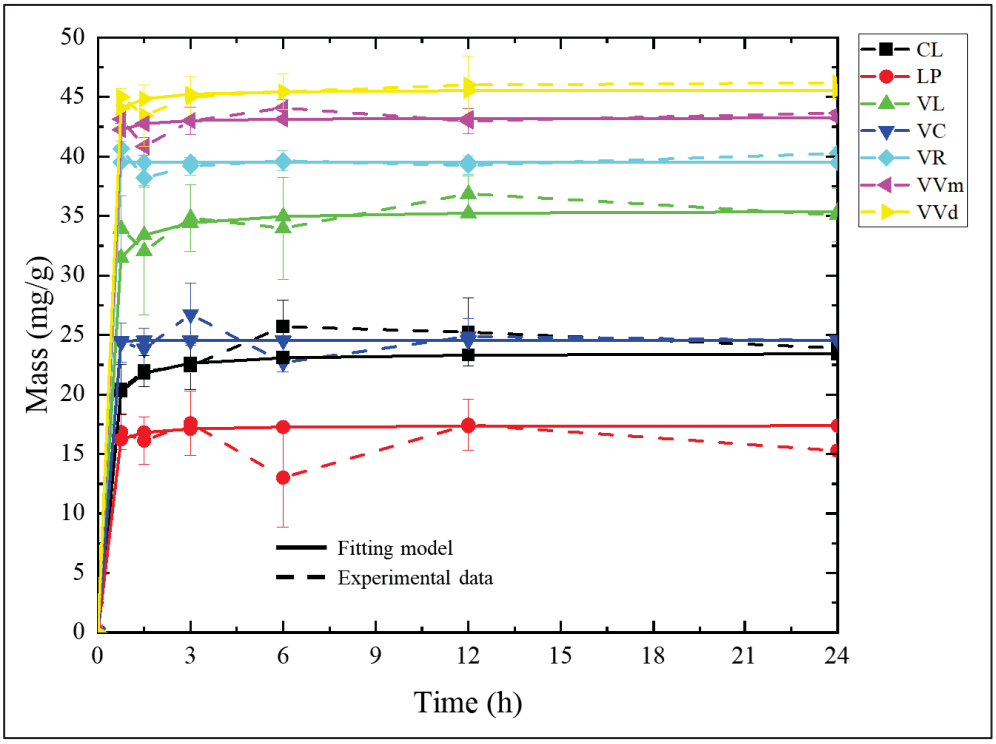

Figure 4.2 Fitting of the pseudo-second-order (PSO) model to INH adsorption kinetics for the six clay samples

Kinetic modeling of the experimental data was performed using three commonly applied models: pseudo-first-order (PFO), pseudo-second-order (PSO), and adsorption-diffusion

model (ADM) and the fitted data are listed in Table 4.2. For all clays, the PSO model provided the best fit, with R^2 values exceeding 0.930. The PFO model showed reasonable correlation only for VVm and VVd, while the ADM exhibited poor fitting across all samples, with R^2 values below 0.550 in most cases.

These findings are consistent with previous studies and suggest that INH adsorption occurs predominantly via chemisorption, involving active site interaction and saturation rather than superficial accumulation (Souza et al., 2021). The suitability of the PSO model further implies that the rate-limiting step is likely associated with interaction at specific adsorption sites within the clay structure.

Table 4.2 Fitting parameters of the pseudo-first-order (PFO), pseudo-second-order (PSO), and adsorption–diffusion model (ADM) for INH adsorption onto different clay samples

Samples		**CL**	**LP**	**VL**	**VC**	**VR**	**VVm**	**VVd**
PFO	R^2	0.869	0.088	0.225	0.001	0.059	0.995	0.994
	k_1	0.212	0.068	0.276	0.001	0.010	0.018	0.025
	q_e	25.057	17.354	44.054	24.447	39.512	43.246	45.603
PSO	R^2	0.984	0.933	0.994	0.983	0.997	0.997	0.997
	k_2	0.352	1.049	0.296	99.741	99.741	1.290	0.828
	q_e	23.549	17.429	35.528	24.538	39.521	43.275	45.639
ADM	R^2	0.445	0.104	0.531	0.002	0.059	0.220	0.550
	k_d	7.407	5.174	7.799	6.624	6.936	8.954	7.242

4.2.3 Hybrids Characterization

The presence of INH adsorbed onto the clay samples was confirmed through thermal, vibrational, and structural analyses. Thermogravimetric analysis (TGA) curves for INH, pristine clays, and selected clay–INH hybrids are shown in Figure 4.3. Two representative hybrid profiles are presented: CL (similar to VC) and VVd (similar to VL, VR, VVm, and LP). In all cases, pristine clays exhibited a characteristic three-stage mass loss: surface water loss around 100 °C, loss of hydration water up to 400 °C, and a sharp loss above 400 °C due to dehydroxylation.

Pure INH showed a one-step degradation profile, with an initial 5% mass loss of around 220 °C and complete degradation by 360 °C, leaving no residual mass at 600 °C. In comparing pristine and hybrid clays, only CL and VC exhibited more surface water in their hybrid forms than in their pristine counterparts. This suggests competitive adsorption between INH and water molecules, which generally results in decreased water retention in the presence of INH (Charles H. Giles & Smith, 1974; Souza et al., 2021). The reversed behavior observed for CL and VC suggests a higher affinity for water, possibly due to specific surface characteristics.

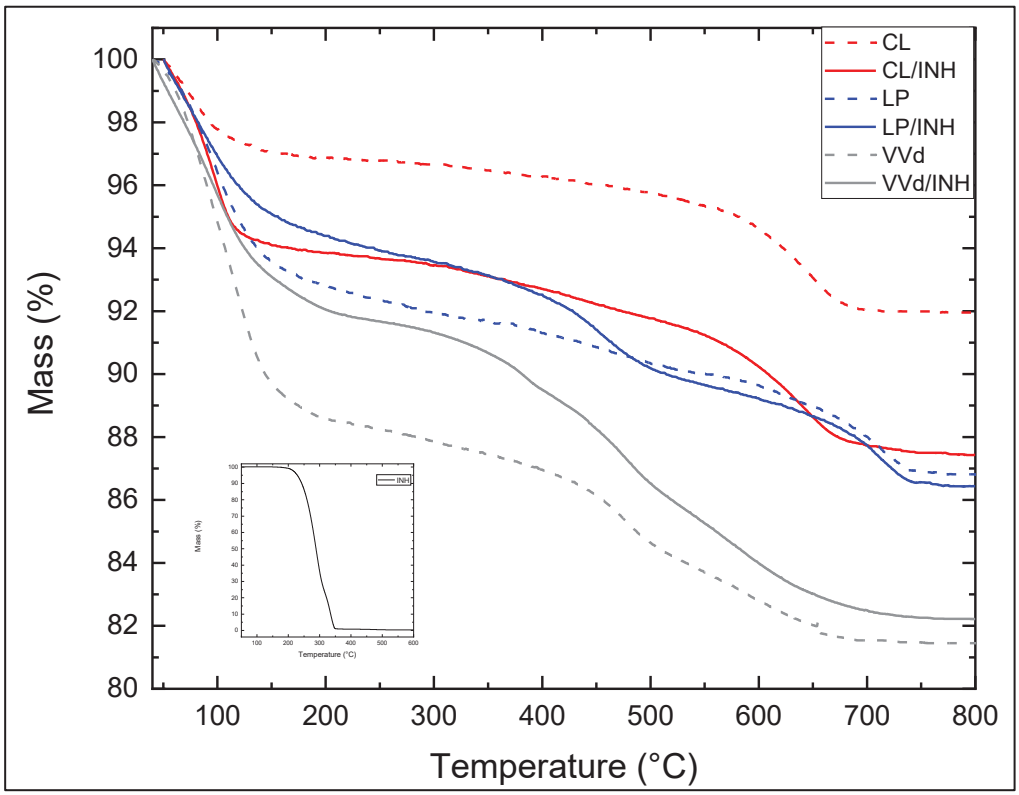

Figure 4.3 TGA curves for INH, CL, CL/INH, VVd, and VVd/INH

TGA data in Table 4.3 show that, except for CL and VC, the hybrid samples presented an additional DTG peak above 380 °C corresponding to INH degradation. For CL and VC, this peak was not distinct; however, the hybrid samples still exhibited higher weight loss

than their pristine counterparts above 400 °C, indicating INH decomposition within this range. The thermal shift of INH degradation to higher temperatures supports the conclusion that the drug was protected within the clay structure, consistent with prior studies (Carazo et al. 2018b).

Table 4.3 DTG peak temperatures and corresponding mass losses for pristine clays and hybrid samples

Sample	1st peak DTG		2nd peak DTG		3rd peak DTG	
	Temperature (°C)	Mass loss (%)	Temperature (°C)	Mass loss (%)	Temperature (°C)	Mass loss (%)
CL	90	3.0	637	6.5	-	-
CL/INH	103	2.3	637	10.9	-	-
VC	60	2.8	470	9.9	655	13.4
VC/INH	67	2.8	478	11.1	669	15.3
LP	94	2.7	711	12.3	-	-
LP/INH	90	2.4	452	8.7	711	12.7
VL	86	4.6	645	12.3	-	-
VL/INH	74	2.9	397	8.4	631	11.9
VR	85	4.6	475	13.9	-	-
VR/INH	70	0.8	377	8.0	481	11.5
VVm	109	6.1	484	14.0	-	-
VVm/INH	104	4.0	388	10.4	484	12.7
VVd	102	5.4	475	14.6	-	-
VVd/INH	94	4.6	384	10.1	475	12.6

FTIR analysis provided further insight into the interaction between INH and the clay surface (Figure 4.4). The pristine clay spectra showed characteristic OH stretching bands around 3470 cm^{-1} and, in the case of dioctahedral smectites, a band at 3621 cm^{-1} (Alabarse et al., 2011; Djomgoue & Njopwouo, 2013). LP lacked the latter due to its trioctahedral structure with Mg^{2+} substituting Al^{3+} (Kiaee et al., 2022).

In the INH FTIR spectra, bands related to the hydrazine group for stretching vibrations of N-H bonds are characteristic of INH (Angadi et al., 2010; Batalha et al., 2019; E. Carazo et al., 2018; Esperanza Carazo et al., 2018; Damasceno Junior et al., 2019; Pandey et al.,

2016). In the hybrid spectra, the more intense peaks were related to the clays' chemical bonds (Almeida et al., 2019; Esperanza Carazo et al., 2018). The characteristic INH bands observed in the hybrids can be included:

- C=O bending and N–H amide group around 1660 cm^{-1},
- Ring C–C symmetric stretching at ~1431 cm^{-1}.
- C-H and C-C groups indicated the presence of the aliphatic part
- Distinct changes in bands at 730 and 831 cm^{-1}, indicating interaction between the INH ring and the clay framework (Damasceno Junior et al., 2019).

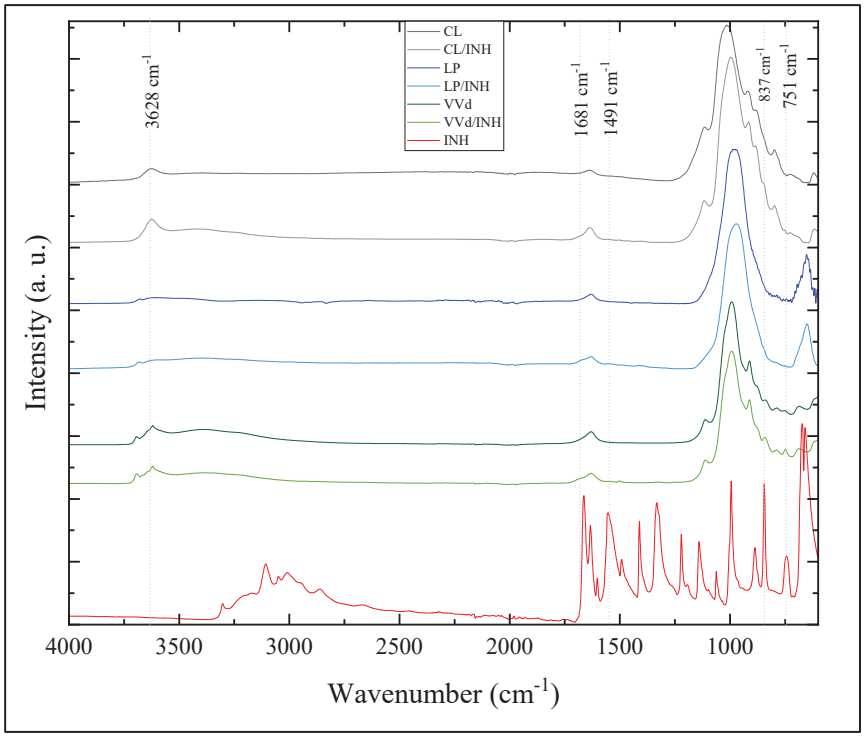

Figure 4.4 FTIR spectra of INH, CL, CL/INH, LP, LP/INH, VVd, and VVd/INH

XRD analysis is shown in Figure 4.5 and it revealed no significant changes in basal spacing upon INH incorporation, suggesting that INH was not intercalated into the interlayer galleries. Instead, adsorption likely occurred on external surfaces or in the mesopores. This is consistent with studies where no interlayer expansion was detected after drug loading, including similar findings for tetracycline (Li et al., 2010). In contrast, other studies have reported intercalation of INH, indicating that such behavior may depend on parameters such as pH, drug concentration, and temperature (Akyuz & Akyuz, 2008; Almeida et al., 2019).

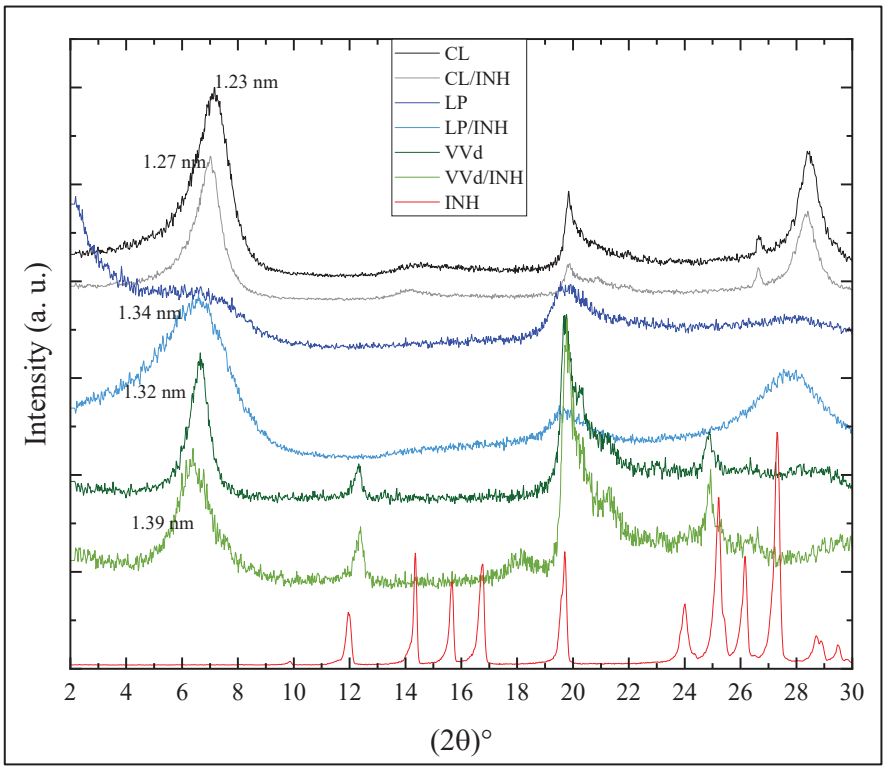

Figure 4.5 XRD patterns of pristine clays, INH, and selected clay–INH hybrids

Together, these results support that INH was not incorporated into the interlamellar regions but was likely retained within pores or adsorbed on external surfaces. FTIR data confirmed chemical interactions between the INH ring and the clay matrix, while TGA data demonstrated the thermal protection of INH by the clay network (Esperanza Carazo et al., 2018).

To further explore the role of pore volume in adsorption efficiency, a correlation was plotted between the adsorption capacity and total pore volume of each clay (Figure 4.6). The curve

suggested that a pore volume near 0.100 cm^3/g resulted in optimal INH adsorption. Below this value, the limited porosity likely hinders drug diffusion and access to adsorption sites. Above this threshold, reduced surface interaction or weak retention within overly large pores may have diminished the trapping of INH molecules.

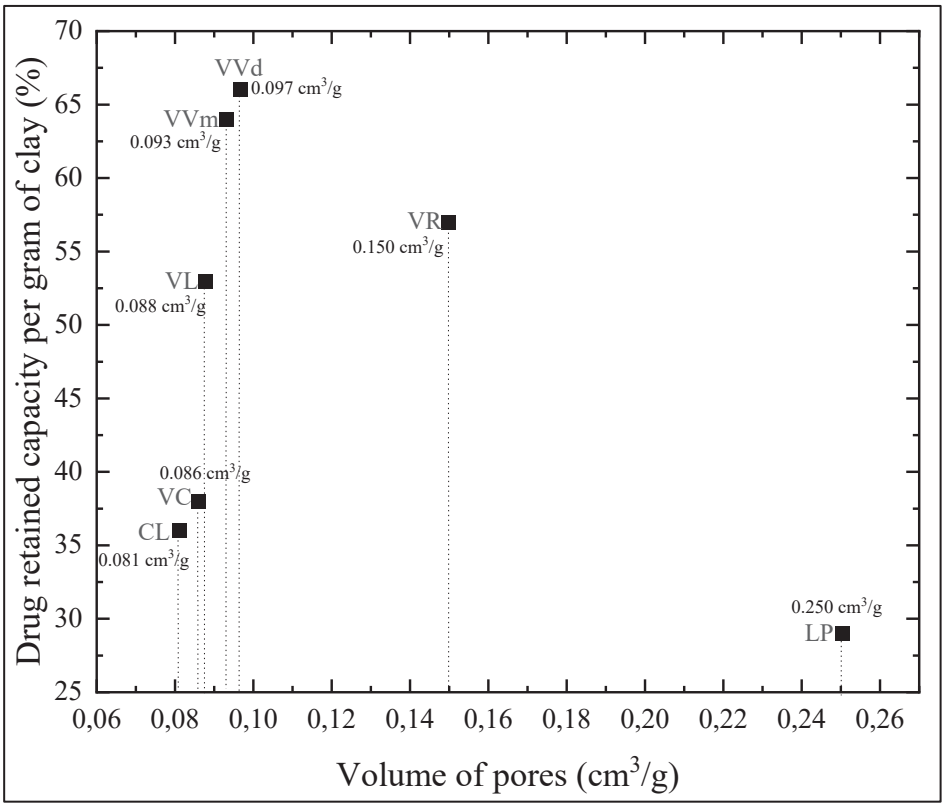

Figure 4.6 Correlation between the volume of pores and INH adsorption efficiency

4.2.4 Drug Release Profile

To investigate the release behavior of INH under physiological conditions, drug release experiments were conducted on three selected clay–INH hybrids: LP, CL, and VVd. These samples were chosen due to their distinct pore volumes, which were previously shown to influence adsorption kinetics. This experiment aimed to simulate the drug release in buffer pH 7.4.

The release profiles are presented in Figure 4.7, where the drug cumulative release (%) is function of the time (min). The data revealed that the hybrid with the highest pore volume, LP (0.250 cm^3/g), exhibited the fastest release rate in the first 90 minutes and the highest cumulative drug release. In contrast, CL (0.081 cm^3/g) and VVd (0.097 cm^3/g) displayed slower release kinetics and lower total release. All samples reached a release plateau by 240 minutes, indicating that most of the drug had been released by that time.

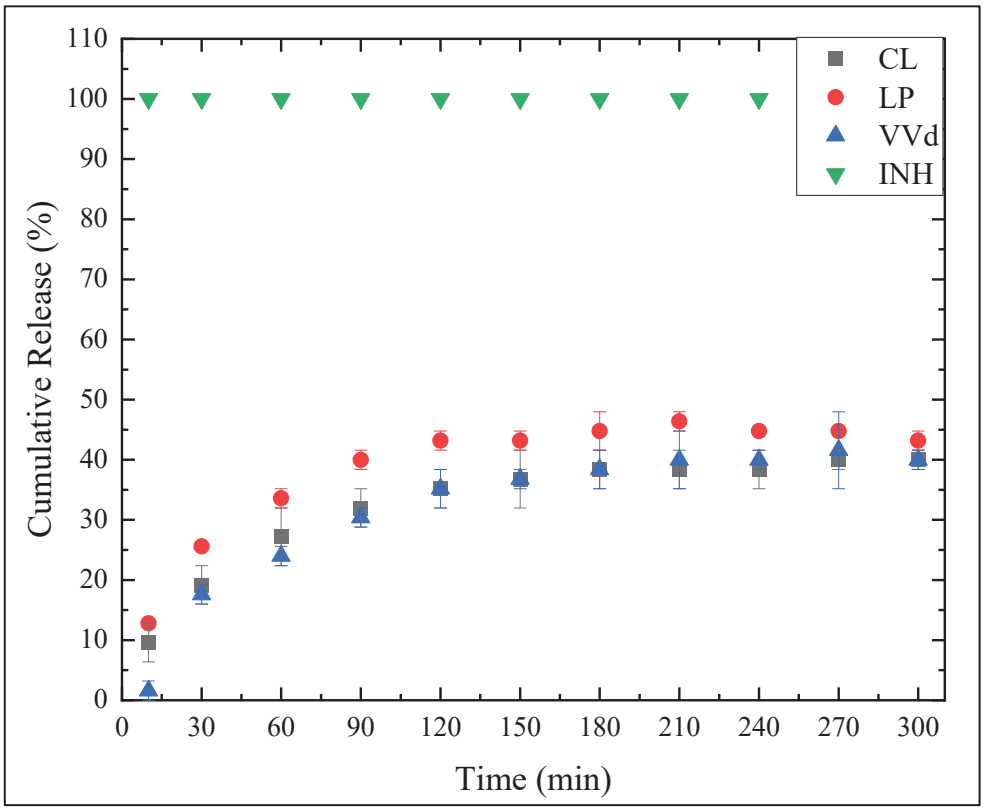

Figure 4.7 INH release profiles from LP, CL, and VVd hybrids in pH 7.4 buffer solution

To better understand the mechanism of release, the experimental data were fitted to two kinetic models: Korsmeyer–Peppas and Higuchi. The results regarding the fitted parameters can be seen in Table 4.4. For all samples, the release exponent n in the Korsmeyer–Peppas model was below 0.5, indicating Fickian diffusion as the dominant release mechanism (Korsmeyer et al., 1983). The Higuchi model also showed a strong fit, with R^2 values above 0.89, confirming the diffusion-controlled nature of release from porous matrices.

Table 4.4 Fitting parameters for Korsmeyer–Peppas and Higuchi models for INH release at pH 7.4

Sample	Korsmeyer-Peppas			Higuchi	
	R^2	n	K	R^2	K_H
CL	0.975	0.238	14.533	0.947	4.269
LP	0.931	0.218	19.226	0.957	5.428
VVd	0.970	0.125	23.244	0.898	4.095

To assess the overall similarity of the release profiles, the similarity factor (f_2) was calculated, and their results are listed in Table 4.5. All comparison pairs yielded f_2 values greater than 50, indicating that the release profiles were statistically similar. The closest similarity was observed between CL and VVd, which had the most comparable pore volumes (0.081 and 0.097 cm^3/g, respectively). In contrast, LP's significantly higher pore volume (0.250 cm^3/g) contributed to more distinct early-stage release behavior. After 180 minutes, however, all three systems exhibited similar cumulative release plateaus.

Table 4.5 Similarity factor (f_2) for dissolution profile comparisons

Comparison Pair of Dissolution Profile	Similarity factor (f2)
CL-LP	59.7
CL-VVd	76.3
LP-VVd	56.3

4.3 Conclusion

This chapter demonstrated that isoniazid (INH) can be efficiently incorporated into smectite clays to develop controlled drug delivery systems. Seven smectite-based clays were evaluated, six of natural origin and one synthetic (Laponite®, LP), to investigate their adsorption, retention, and release behaviors.

Adsorption kinetics at neutral pH revealed that equilibrium was reached within three hours, with maximum adsorption capacities reaching up to 46 mg/g. XRD analysis indicated that INH was not intercalated into the interlayer space of the clays, but rather adsorbed onto external surfaces and within inter-tactoid pores. A pore volume of approximately 0.100 cm^3/g was identified as optimal for INH adsorption.

To further explore this relationship, three clays with distinct pore volumes (CL: 0.081 cm^3/g, VVd: 0.097 cm^3/g, and LP: 0.250 cm^3/g) were selected for release studies at pH 7.4. The release profiles confirmed that pore volume significantly influences both the rate and extent of INH release. These findings emphasize the importance of considering pore volume as a key parameter in the design of clay-based drug delivery systems.

In the next chapter, VVd, the clay that exhibited the highest adsorption capacity, will be further examined to assess the influence of pH and initial drug concentration on the adsorption and release behavior of INH.

CHAPTER 5

THE INFLUENCE OF INH ADSORPTION ON CLAY-DRUG INTERACTIONS AND RELEASE

Jessica de Carvalho Arjona[a], Carina Ulsen[b], Dayane Tada[c], Francisco Rolando Valenzuela-Diaz[d], Nicole Raymonde Demarquette[e],

[a,d]Departamento de Engenharia Metalúrgica e de Materiais, Escola Politécnica, Universidade de São Paulo, Av. Professor Mello Moraes, 2463, São Paulo, SP 05508-030, Brazil
[a,e]Mechanical Engineering Department, École de Technologie Supérieure, 1100 R. Notre Dame O, Montréal, QC H3C 1K3, Canada
[b]Departamento de Engenharia de Minas e de Petróleo, Escola Politécnica, Universidade de São Paulo, Av. Prof. Mello Moraes, 2373, São Paulo, SP 05508-030, Brazil
[c]Universidade Federal de São Paulo, Brazil Laboratory of Nanomaterials and Nanotoxicology, Rua Talim, 300, São José dos Campos, SP 12231-280, Brazil

Paper published in *Journal of Drug Delivery Science and Technology*, June 2025

5.1 Introduction

This chapter is based on the work published in Journal of Drug Delivery Science and Technology (De Carvalho Arjona et al., 2025). Building on the results of Chapter 4, the clay with the highest INH adsorption capacity, VVd, was selected for further investigation. The aim was to assess how the pH during adsorption affects drug–clay interactions and subsequent release behavior.

To this end, INH was incorporated into VVd under two different pH conditions: acidic (pH 2) and neutral (pH 7). At pH 2, INH is protonated and positively charged, which enhances its electrostatic attraction to the negatively charged clay surface, leading to increased loading. At pH 7, where INH remains predominantly neutral, a biphasic adsorption process was observed, indicating a shift in the mechanism of interaction.

The release behavior of INH from montmorillonite (Mtt) was also examined, focusing on how the adsorption environment influences the retention and release dynamics. Adsorption isotherms were interpreted using Giles' classification model (C. H. Giles et al., 1960;

Charles H. Giles & Smith, 1974), which categorizes adsorption mechanisms based on the shape of the isotherm curve.

These findings contribute valuable insights into the design of clay-based drug delivery systems, demonstrating the importance of pH not only in release environments but also during drug incorporation. Optimizing adsorption conditions could enhance drug retention and controlled release performance.

5.2 Results and Discussion

5.2.1 Adsorption studies

Figure 5.1 shows the adsorption curves of isoniazid by VVd at pH 2 and 7. In the graph, the amount of INH adsorbed (mg/g) is plotted as a function of the remaining INH concentration (mg/L) on the solution after the adsorption. The results demonstrate that pH strongly influences both the adsorption capacity and the mechanism of interaction between the drug and clay surface (C. H. Giles et al., 1960; Charles H. Giles & Smith, 1974).

At pH 7, the isotherm exhibits an L3-type shape according to Giles' classification, which is associated with low initial affinity between adsorbate and adsorbent, followed by enhanced adsorption as concentration increases. The adsorption curve initially rises sharply and reaches a short plateau around 20 mg/g (point a), suggesting monolayer formation. This behavior, also reported by Carazo et al. (2018b) and (Souza et al., 2021), likely results from hydrogen bonding between the neutral INH molecules and hydroxyl groups on the clay surface. As concentration continues to increase, a second adsorption phase is observed (point b), indicating multilayer deposition of INH on previously adsorbed drug molecules.

At pH 2, the isotherm follows an H2-type pattern, typical of strong initial interactions. In this acidic environment, INH becomes doubly protonated at both the endocyclic and exocyclic nitrogen sites, enhancing electrostatic attraction to the negatively charged clay surface. Complete INH adsorption occurs at initial concentrations below 800 mg/L, with the curve reaching a plateau at approximately 100 mg/g (point c). After this point, additional adsorption is limited, likely due to electrostatic repulsion between adjacent protonated INH molecules on the clay surface (Almeida et al., 2019; Damasceno Junior et al., 2019; Souza et al., 2021).

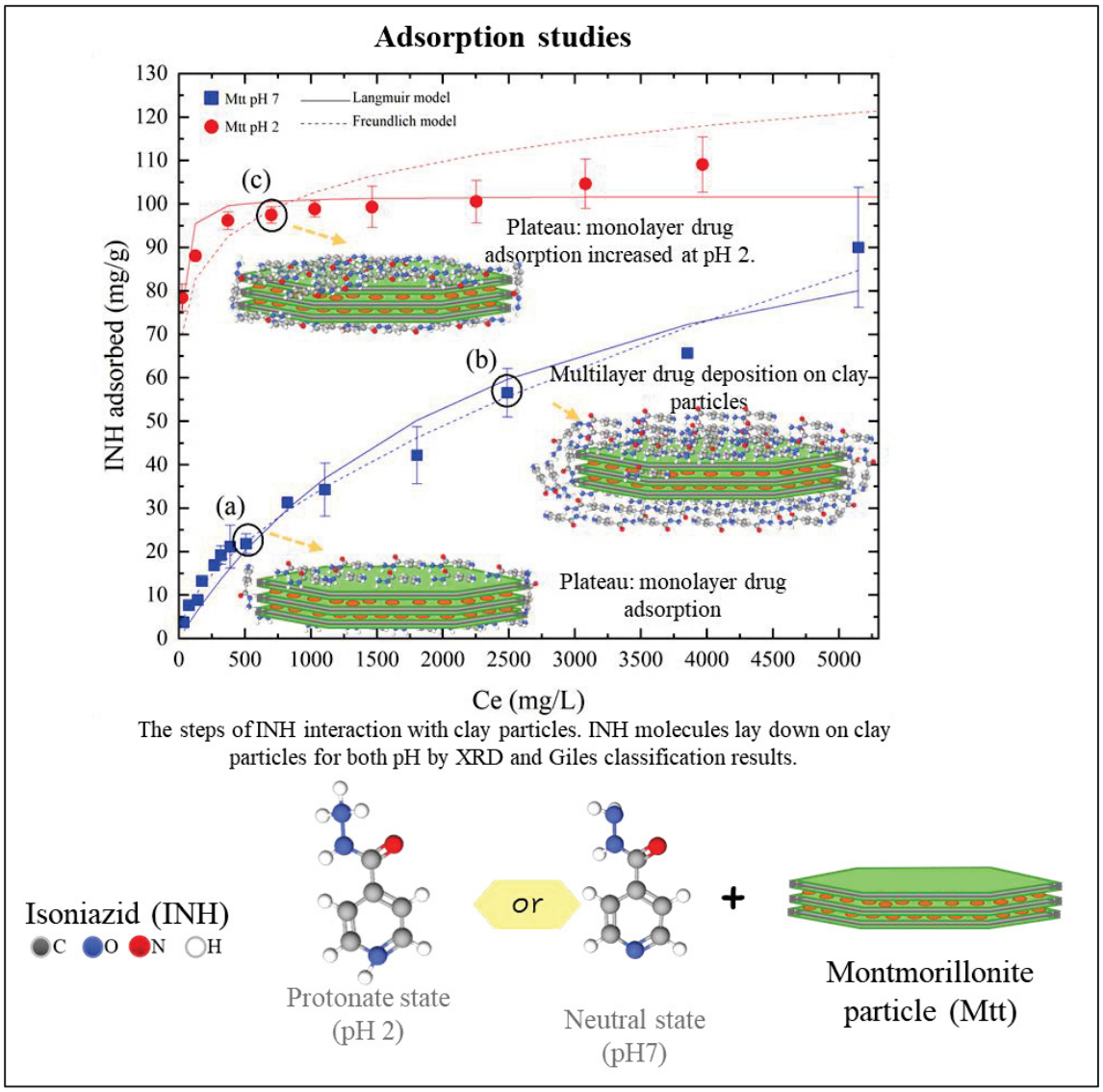

Figure 5.1 Adsorption isotherms of INH onto VVd at pH 2 and pH 7. Points a–c correspond to adsorption phases defined by Giles' classification. A schematic representation of clay–drug interactions is also included (modified from De Carvalho Arjona et al., 2025a)

To better understand these interactions, the adsorption data were fitted to both the Langmuir and the Freundlich models (Table 5.1). The Freundlich model provided the best fit (R^2 = 0.956 at pH 2 and R^2 = 0.987 at pH 7), indicating a heterogeneous adsorption process

involving a range of binding energies across the clay surface (Calabrese et al., 2013). These include interactions at basal surfaces, edges, and interparticle pores.

Although the Langmuir model yielded a reasonable fit at pH 7 ($R^2 = 0.965$), its performance was lower at pH 2 ($R^2 = 0.744$), suggesting that monolayer adsorption on a uniform surface does not fully describe the process under strongly acidic conditions. The Langmuir-derived maximum adsorption capacities (Q_M) were 101.8 mg/g at pH 2 and 117.7 mg/g at pH 7, aligning with experimental saturation trends. The R_L factor further confirmed favorable adsorption at both pH levels, especially at pH 2 ($R_L = 0.0756$).

Table 5.1 Fit model parameters of INH adsorption by VVd at pH 2 and pH 7

Model	Equation	Eq.	Parameters	pH	
				2	7
Langmuir	$C_s = \frac{Q_M \cdot K_L \cdot C_e}{1 + K_L \cdot C_e}$	(5.1)	K_L(L/mg)	0.1201	0.0004
			Q_M (mg/g)	101.8349	117.7125
			R_L	0.0756	0.9536
			R^2	**0.7442**	**0.9648**
Freundlich	$C_s = K_F \cdot C_e^n$	(5.2)	K_F	50.4232	0.6115
			N_F	9.7450	1.7330
			R^2	**0.9555**	**0.9873**

These findings suggest that pH-dependent changes in INH charge and clay–drug interaction mechanisms strongly influence adsorption efficiency. Acidic environments enhance electrostatic binding, while neutral pH conditions favor hydrogen bonding and multilayer formation.

5.2.2 FTIR

The FTIR spectra of INH, pristine VVd, and VVd–INH hybrids are presented in Figure 5.2. The spectrum of VVd shows typical montmorillonite features, including a strong Si–O stretching vibration near 998 cm^{-1} (Bekaroğlu et al., 2018), and an Al–Al–OH deformation band around 910 cm^{-1}. Broad absorption bands near 3600 cm^{-1} are attributed to O–H stretching of interlayer and adsorbed water (Silva-Valenzuela et al., 2018).

The VVd–INH hybrids displayed characteristic INH bands whose intensity and number increased with drug loading. In VVd–INH (a), which had the lowest INH content, only one distinct INH band was observed at 1437 cm^{-1}, attributed to ring C–C stretching (Akyuz & Akyuz, 2008; Esperanza Carazo et al., 2018). In VVd–INH (b), additional bands appeared at 1668, 1539, 1502, 1428, and 841 cm^{-1}, corresponding to ring vibrations and stretching modes of C–N and N–H groups. In the hybrid with the highest INH content, VVd–INH (c), further peaks were detected at 1692 and 1248 cm^{-1}. The 1692 cm^{-1} band represents a shifted C=O vibration, originally observed at 1668 cm^{-1} in pure INH, and is attributed to hydrogen bonding interactions between INH and the clay surface (Akyuz et al., 2010).

The band near 1632 cm^{-1}, corresponding to the O–H bending vibration of water in pristine VVd, shifted down to 1630, 1625, and 1622 cm^{-1} for hybrids (a), (b), and (c), respectively. This progressive shift supports the formation of hydrogen bonds between INH and structural water (Alabarse et al., 2011; Esperanza Carazo et al., 2018). Likewise, a shift in the Si–O band from 998 cm^{-1} in pristine VVd to 1003 cm^{-1} in VVd–INH (c) reflects changes in clay platelet orientation, possibly due to electrostatic interactions with the protonated drug molecules (Akyuz & Akyuz, 2008).

The FTIR results confirm that drug loading induces specific structural changes in the clay and indicate chemical interactions involving INH's carboxyl, hydrazine, and pyridine groups with the silicate framework of VVd. These findings are consistent with previous studies on drug–clay hybrid formation (Akyuz & Akyuz, 2008; Esperanza Carazo et al., 2018).

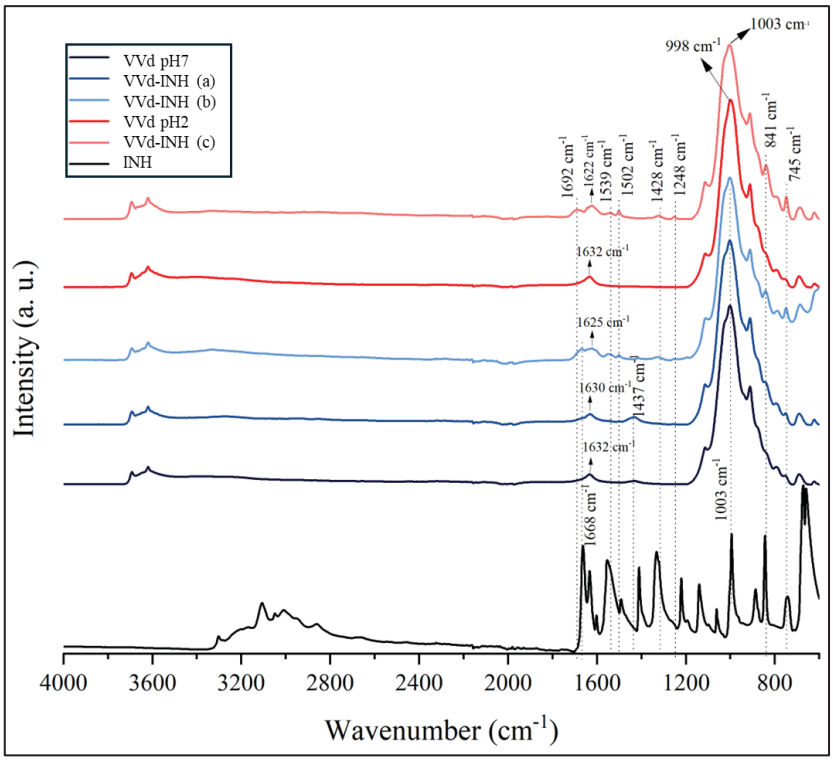

Figure 5.2 FTIR spectra of INH, pristine VVd, and VVd–INH hybrids with increasing INH loading

5.2.3 XRD

Figure 5.3 presents the XRD patterns of pristine VVd, its INH-loaded hybrids, and pure INH. No distinct peaks of crystalline INH were detected in the hybrid patterns, suggesting that the drug was either amorphous or molecularly dispersed on the clay surface. Alternatively, the INH crystallites may have been too disordered or small to produce detectable diffraction signals. These findings are consistent with previous studies where drug molecules, especially small ones like INH, did not produce identifiable peaks in clay-based hybrids (Calabrese et al., 2013; Kevadiya et al., 2012).

Following INH incorporation, a reduction in interlayer spacing was observed. For the hybrids prepared at pH 7, the d_{001} spacing decreased from 1.50 nm to 1.38 nm, and for VVd–INH (c) (adsorbed at pH 2), from 1.43 nm to 1.28 nm. This contraction suggests that drug incorporation displaced water molecules from the interlamellar space—an effect also reported for other drug–clay systems (Bromberg et al., 2011; Calabrese et al., 2013, 2017;

Cavalcanti et al., 2019). The reduced interlayer water likely reflects a stronger affinity of INH for the clay surface, outcompeting water for adsorption (Charles H. Giles & Smith, 1974).

The lack of interlayer expansion aligns with studies showing that significant d_{001} shifts typically occur only with bulky organic molecules, such as organoammonium salts with long alkyl chains (de Paiva et al., 2008). Given the compact structure of INH, its adsorption may occur predominantly on external surfaces or within edge and defect sites rather than through intercalation.

Interestingly, new peaks emerged around 20.0°, 26.5°, 28.1°, 28.7°, and 29.0° (2θ), accompanied by increased peak intensity. These features may suggest partial crystallization of INH on the clay surface, as previously proposed for similar hybrid systems (Gulen & Demircivi, 2020). This implies that some INH molecules, particularly at higher loading, organize into short-range ordered domains without fully integrating into the clay lattice.

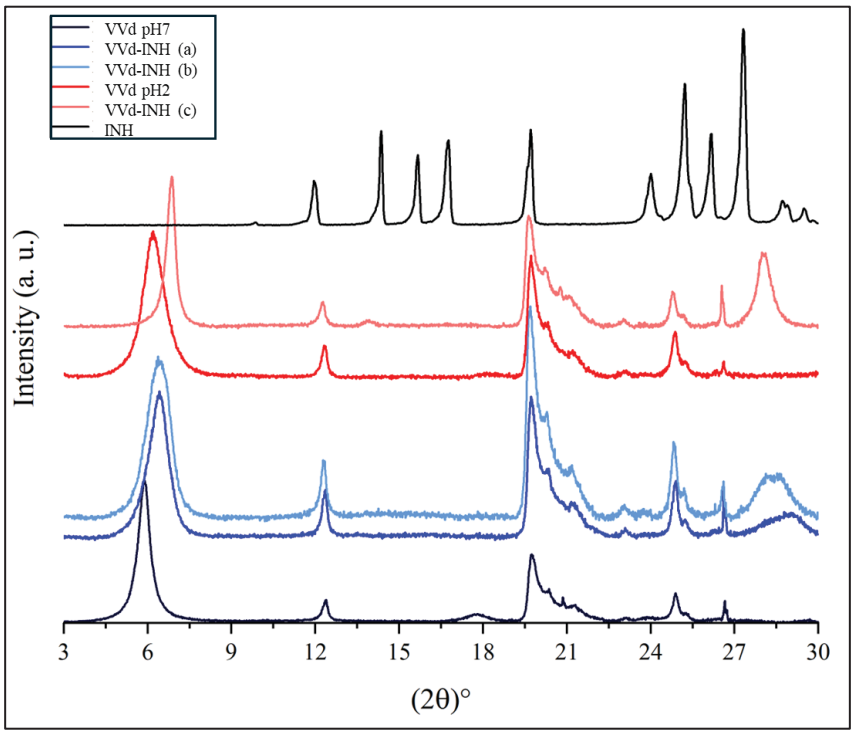

Figure 5.3 XRD patterns of pristine VVd, VVd–INH hybrids, and pure INH

Together, these findings reinforce the conclusion that INH interacts strongly with the clay surface, primarily through external adsorption, and that the observed structural changes are driven by displacement of water molecules and weak crystallization tendencies of surface-deposited drug.

5.2.4 TGA

Figure 5.4 presents the TGA curves for pure INH, pristine VVd, and the VVd–INH hybrids. The thermal degradation of INH occurred in a single step between 126 °C and 350 °C, leaving no residual mass. In contrast, VVd and its hybrids exhibited the typical three-stage thermal degradation behavior of smectite clays: (i) surface water evaporation, (ii) loss of interlayer or structural water, and (iii) dehydroxylation. VVd at pH 2 presented a reduction in surface water compared to VVd due to the incorporation of H^+ on the clay surface in the acidic pH (Swartzen-Allen & Matijevic, 1974).

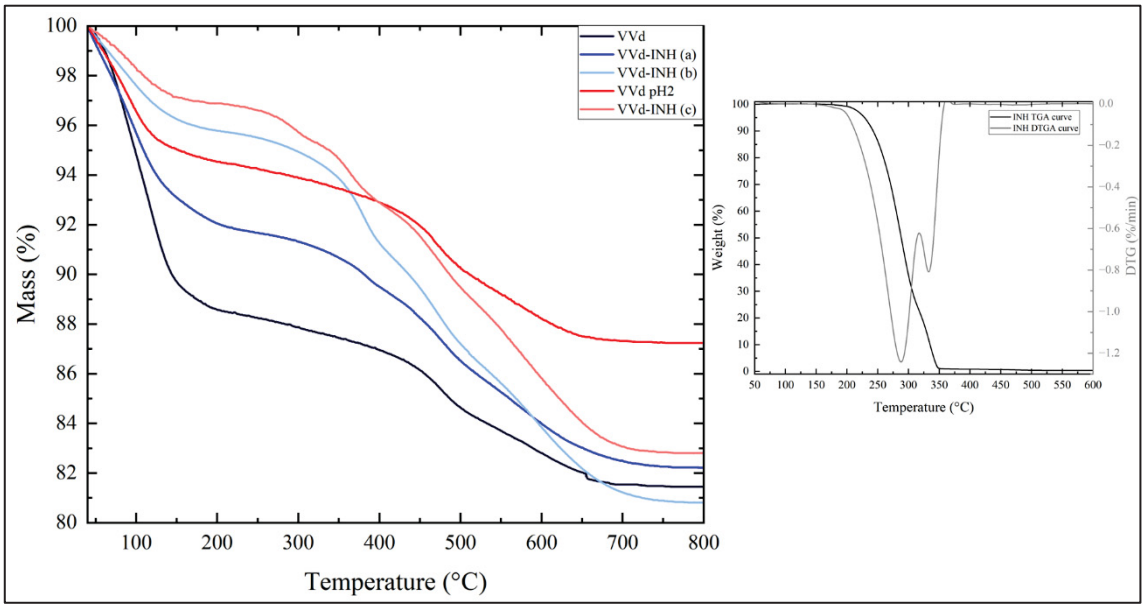

Figure 5.4 TGA curves of pure INH, pristine VVd, and VVd–INH hybrids

Incorporation of INH significantly influenced all three degradation stages. As summarized in Table 5.2, increasing drug content led to a progressive reduction in surface water loss in the first stage, from 10.3% in pristine VVd to 2.8% in VVd–INH (c). This reduction is

consistent with the hypothesis that INH outcompetes water for adsorption sites, as previously discussed in the adsorption and XRD sections.

The second degradation stage, related to internal water molecules, also narrowed in temperature range and showed reduced weight loss in drug-loaded samples. Notably, VVd–INH (c), the hybrid with the highest INH content, exhibited this transition over the narrowest temperature range (146–266 °C), further supporting the idea that INH replaces inner water molecules within the pore structure.

The third stage, associated with both dehydroxylation and INH degradation, showed an increase in mass loss proportionate to the amount of drug incorporated. The presence of INH was confirmed by the emergence of additional DTG peaks between 295 °C and 580 °C, corresponding to drug decomposition. These peaks were shifted to higher temperatures compared to pure INH (typically 287 °C and 332 °C), indicating that INH was thermally stabilized upon incorporation, likely due to strong drug–clay interactions.

Table 5.2 TGA weight loss (%) of pristine VVd and VVd–INH hybrids at each stage of thermal degradation

Stage		1st stage	2nd stage	3rd stage				
VVd	Temp. range (°C)	40 - 149	149 - 439	439 - 494	494 - 675	-	-	-
	Weight loss (%)	10.3	3.3	1.7	3.1	-	-	-
VVd-INH (a)	Temp. range (°C)	40 - 144	144 - 349	349 - 433	433 - 497	497 - 668	-	-
	Weight loss (%)	6.7	2.6	1.9	2.2	3.8	-	-
VVd-INH (b)	Temp. range (°C)	40 - 133	133 - 336	336 - 400	400 - 444	444 - 489	489 - 667	-
	Weight loss (%)	3.4	2.3	3.1	1.5	2.3	5.8	-
VVd pH 2	Temp. range (°C)	40 - 132	132 - 415	415 - 502	502 - 643	-	-	-
	Weight loss (%)	4.7	2.6	2.5	2.6	-	-	-
VVd-INH (c)	Temp. range (°C)	40 - 146	146 - 266	266 - 338	338 - 434	434 - 495	495 - 557	557 - 680
	Weight loss (%)	2.8	0.8	1.4	2.9	1.7	2.8	4.3

The DTG analysis in Table 5.3 further supports these interpretations. INH degradation peaks around 300–380 °C became more pronounced with increasing drug content. The presence of multiple DTG peaks in VVd–INH (c), especially those at 295, 367, and 580 °C, also suggests that INH was distributed in distinct environments, some more tightly bound and thermally stabilized than others. Since INH degradation typically shows peaks around 287 and 332 °C. The shift to higher temperatures in the decomposition of INH may indicate drug intercalation.

Table 5.3 Temperature and weight loss for INH, VVd, and their hybrids

DTG Peak		1	2	3	4	5
VVd	Temperature (°C)	105	477	-	-	-
	Weight loss (%)	5.8	14.7	-	-	-
VVd/INH (a)	Temperature (°C)	93	386	477	583	-
	Weight loss (%)	6.4	10.1	12.6	15.6	-
VVd/INH (b)	Temperature (°C)	87	381	473	597	-
	Weight loss (%)	1.9	7.7	11.6	16.1	-
VVd pH 2	Temperature (°C)	85	476	-	-	-
	Weight loss (%)	2.4	9.0	-	-	-
VVd/INH (c)	Temperature (°C)	95	295	367	473	580
	Weight loss (%)	1.6	4.2	6.1	9.5	13.4

These results demonstrate that the thermal behavior of the clay–drug hybrid system is significantly altered by drug incorporation, both in terms of stability and degradation profile. The absence of a clear INH melting point in DSC analysis (not shown here) supports the formation of a stable hybrid complex, rather than a simple physical mixture (Esperanza Carazo et al., 2018).

5.2.5 DSC

Figure 5.5 shows the DSC thermograms of pure INH, pristine VVd (at pH 7 and pH 2), and the VVd–INH hybrids. The curve for pure INH displayed a distinct endothermic peak at approximately 175 °C, corresponding to the drug's melting point, as previously reported (Esperanza Carazo et al., 2018).

For the clay samples (VVd and VVd pH 2), broad endothermic events were observed below 150 °C, which are attributed to the loss of adsorbed surface water. These thermal events

were less intense in the hybrids, indicating a reduction in surface water content following INH incorporation, corroborating the results from TGA analysis.

Notably, none of the VVd–INH hybrids exhibited the melting peak of INH, regardless of the drug loading or the pH used during adsorption. This absence suggests that INH was no longer in its crystalline form and instead existed in either an amorphous state or a strongly bound molecularly dispersed form within the clay matrix. Similar behavior has been observed in other drug–clay systems and is often interpreted as evidence of high drug–clay affinity, consistent with the formation of a stable hybrid structure rather than a simple physical mixture (Esperanza Carazo et al., 2018).

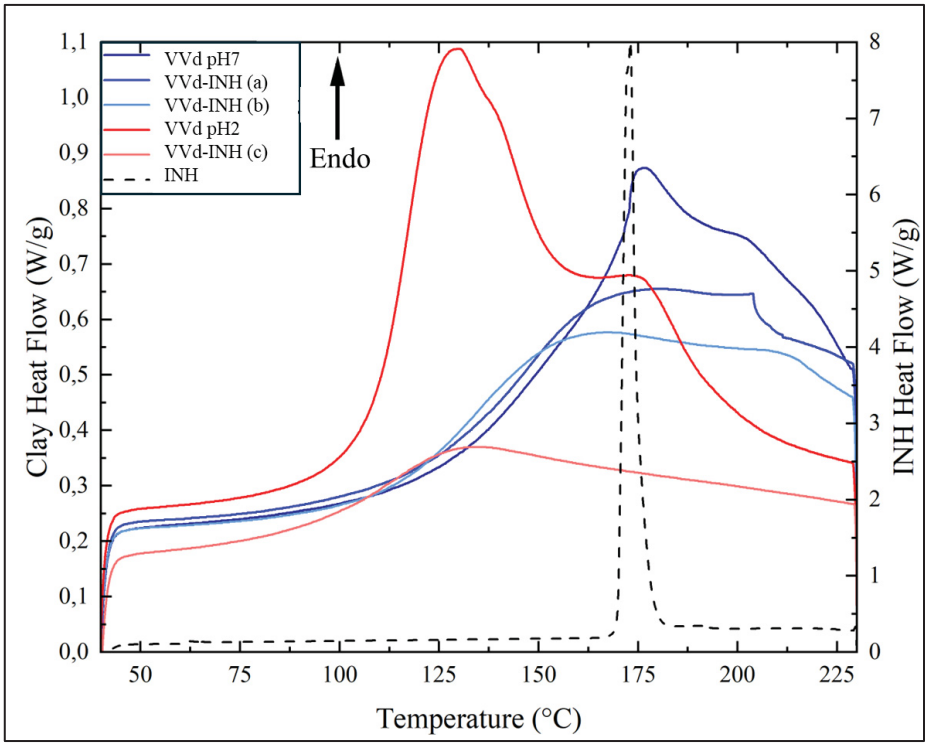

Figure 5.5 DSC curves of pure INH, pristine VVd (pH 7 and pH 2), and VVd–INH hybrids

Together with the TGA and XRD results, these DSC findings further support that INH is incorporated into VVd via interactions that suppress crystallinity and enhance thermal stability, which are desirable features for developing controlled-release drug delivery systems.

5.2.6 Release test

The cumulative release profiles are shown in Figure 5.6, where the cumulative release of INH by the hybrids VVd-INH (a), (b), and (c) over time is displayed. In the first two hours, the release was made in pH 2.0, mimicking the stomach; the following 2 hours, at pH 6.8, followed by 4 hours in pH 7.4. The results demonstrate a strong pH dependence in the release behavior. VVd–INH (a), prepared under monolayer adsorption conditions at pH 7, released no detectable INH at pH 2, likely due to the strong electrostatic interactions between the protonated INH molecules and the negatively charged clay surface. In contrast, VVd–INH (b) and VVd–INH (c), which contained multilayered or equilibrium-loaded drug, showed appreciable release at acidic pH, with hybrid (b) releasing ~40% of its total INH content during this phase. This early release can be attributed to outer-layer drug molecules weakly adsorbed or loosely deposited atop more strongly bound INH layers.

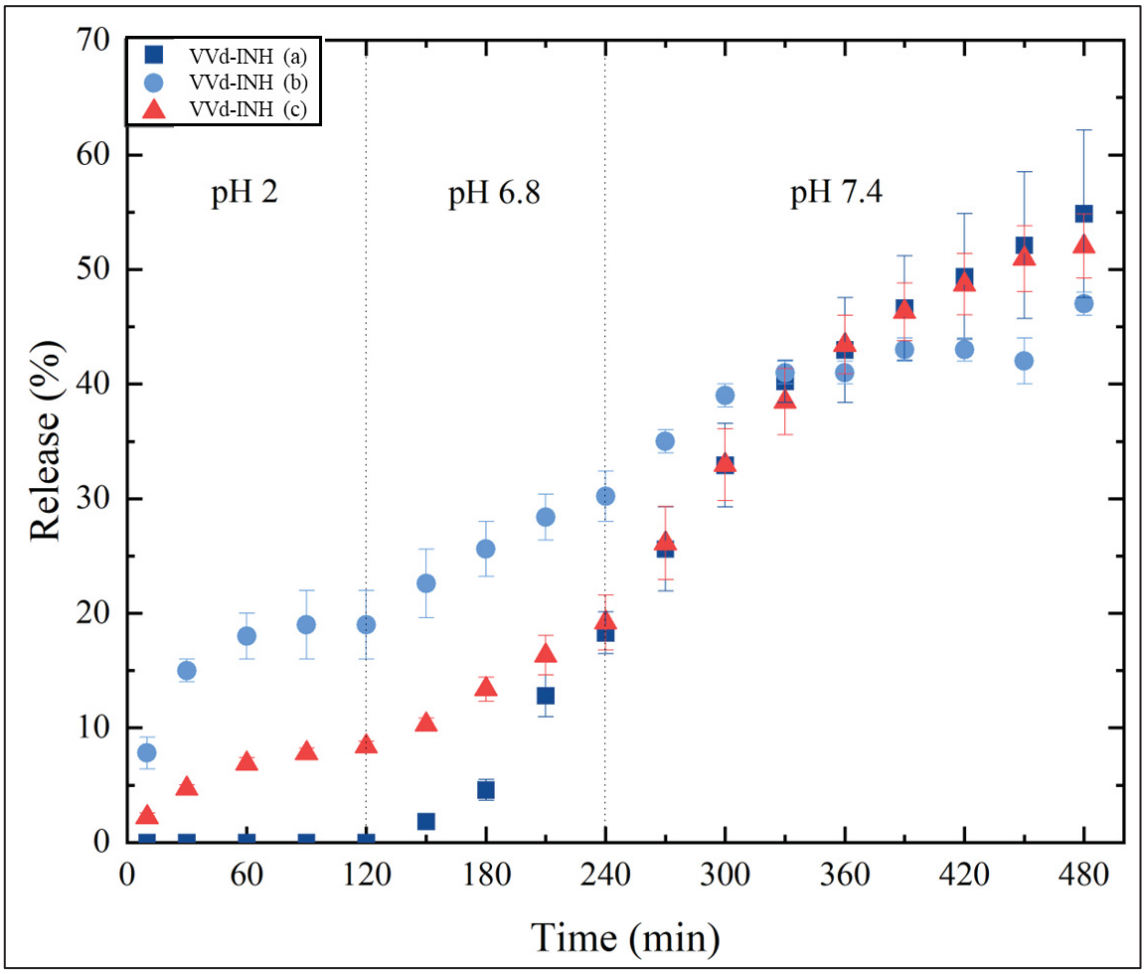

Figure 5.6 Release profile of INH from VVd–INH hybrids under simulated oral conditions

The results demonstrate a strong pH dependence in the release behavior. VVd–INH (a), prepared under monolayer adsorption conditions at pH 7, released no detectable INH at pH 2, likely due to the strong electrostatic interactions between the protonated INH molecules and the negatively charged clay surface. In contrast, VVd–INH (b) and VVd–INH (c), which contained multilayered or equilibrium-loaded drug, showed appreciable release at acidic pH, with hybrid (b) releasing ~40% of its total INH content during this phase. This early release can be attributed to outer-layer drug molecules weakly adsorbed or loosely deposited atop more strongly bound INH layers.

Upon transitioning to pH 6.8 and 7.4, all hybrids demonstrated increased release rates, consistent with reduced protonation of INH and diminished electrostatic interactions. While

the percentage of INH released was comparable across all samples by the end of the test, the total mass of drug released varied significantly. VVd–INH (c), having the highest loading (~100 mg/g), released the greatest absolute amount (51.1 mg/g), whereas VVd–INH (a) released the least (11.0 mg/g). Detailed release values and standard deviations are provided in Table 5.4, where the amount of INH released by the hybrids.

Table 5.4 Cumulative INH release (mg/g) from VVd–INH hybrids under pH-controlled conditions

pH	Time (min)	VVd-INH (a)		VVd-INH (b)		VVd-INH (c)	
		Release (mg/g)	Dev.	Release (mg/g)	Dev.	Release (mg/g)	Dev.
2.0	10	0.0	0.0	4.7	0.1	2.2	0.3
	30	0.0	0.0	9.0	0.1	4.6	0.3
	60	0.0	0.0	10.8	0.2	6.8	0.5
	90	0.0	0.0	11.4	0.3	7.7	0.4
	120	0.0	0.0	11.4	0.3	8.2	0.4
6.8	150	0.4	0.0	13.6	0.4	10.1	0.6
	180	0.9	0.0	15.4	0.4	13.1	1.0
	210	2.6	0.0	17.0	0.3	16.0	1.7
	240	3.7	0.1	18.1	0.4	18.8	2.3
7.4	270	5.1	0.2	21.0	0.2	25.6	3.1
	300	6.6	0.2	23.4	0.2	32.4	3.1
	330	8.0	0.1	24.6	0.2	37.8	2.9
	360	8.6	0.4	24.6	0.2	42.6	2.5
	390	9.3	0.4	25.8	0.3	45.5	2.5
	420	9.9	0.5	25.8	0.3	47.8	2.6
	450	10.4	0.7	25.2	0.5	50.0	2.8
	480	11.0	0.8	28.2	0.3	51.1	2.7

To better understand the release mechanisms, the experimental data were fitted to three kinetic models: Zero-order, Higuchi, and Korsmeyer–Peppas (Table 5.5). The Higuchi model yielded the best overall fit, suggesting that Fickian diffusion was the predominant release mechanism (Damasceno Junior et al., 2019). However, for VVd–INH (b) at pH 7.4 and VVd–INH (c) at pH 2, the Korsmeyer–Peppas model provided a better fit ($R^2 = 0.826$ and 0.986, respectively), with n-values < 0.5, again supporting diffusion-driven release.

Of particular interest, VVd–INH (c) exhibited a release profile closely following the Zero-order model at both pH 6.8 and 7.4 (R^2 = 0.996 and 0.936, respectively), indicating that drug release was independent of concentration and occurred at a constant rate. This behavior is ideal for controlled-release applications and reinforces the conclusion that strong drug–clay interactions, as observed in VVd–INH (c), lead to more stable and sustained delivery profiles.

Table 5.5 Release fitting parameters of VVd hybrids made at pH 2 and pH 7 in three different models: Zero-order, Higuchi, and Korsmeyer-Peppas

Hybrid	pH	Zero order		Higuchi		Korsmeyer-Peppas		
		k_o	R^2	K_h	R^2	K_o	n	R^2
VVd-INH (a)	2.0	-	-	-	-	-	-	-
	6.8	0.052	0.891	0.708	0.960	3.629	0.188	0.954
	7.4	0.115	0.951	2.259	0.966	1.897	0.530	0.965
VVd-INH (b)	2.0	0.207	0.716	2.047	0.844	1.895	0.520	0.839
	6.8	0.135	0.700	1.923	0.994	1.056	0.613	0.993
	7.4	0.108	0.813	2.141	0.824	4.370	0.380	0.826
VVd-INH (c)	2.0	0.084	0.893	0.814	0.969	1.860	0.310	0.986
	6.8	0.077	0.996	1.076	1.000	2.778	0.321	0.999
	7.4	0.113	0.936	2.219	0.954	1.894	0.527	0.953

Together, these findings underscore the importance of adsorption conditions, particularly pH and loading level, in governing not only the amount of drug incorporated but also the release dynamics. The controlled release observed for VVd–INH (c), combined with its high adsorption capacity and bio-inert clay matrix, highlights its promise as a viable oral DDS for INH, with potential to minimize dosing frequency and improve patient compliance. Similar incomplete release profiles were also reported in other INH–clay systems (Calabrese et al., 2013; Saifullah et al., 2016; Souza et al., 2021).

5.2.7 Cell viability

To assess the biocompatibility of the clay and its hybrid system, an MTT cytotoxicity assay was performed using L929 fibroblast cells exposed to extracts of pristine VVd and the VVd–INH (c) hybrid. The results, presented in Figure 5.7, show the cell viability for both particles. VVd alone did not exhibit any cytotoxic effect; in fact, it slightly enhanced cell

viability, a phenomenon that has been previously observed for some natural clays. In contrast, VVd–INH (c), which incorporated the highest INH concentration (~100 mg/g), resulted in a modest 20% decrease in viability, likely attributed to the presence of isoniazid. Despite this reduction, cell viability remained above 80%, which is the accepted threshold for non-cytotoxicity according to ISO 10993 standards.

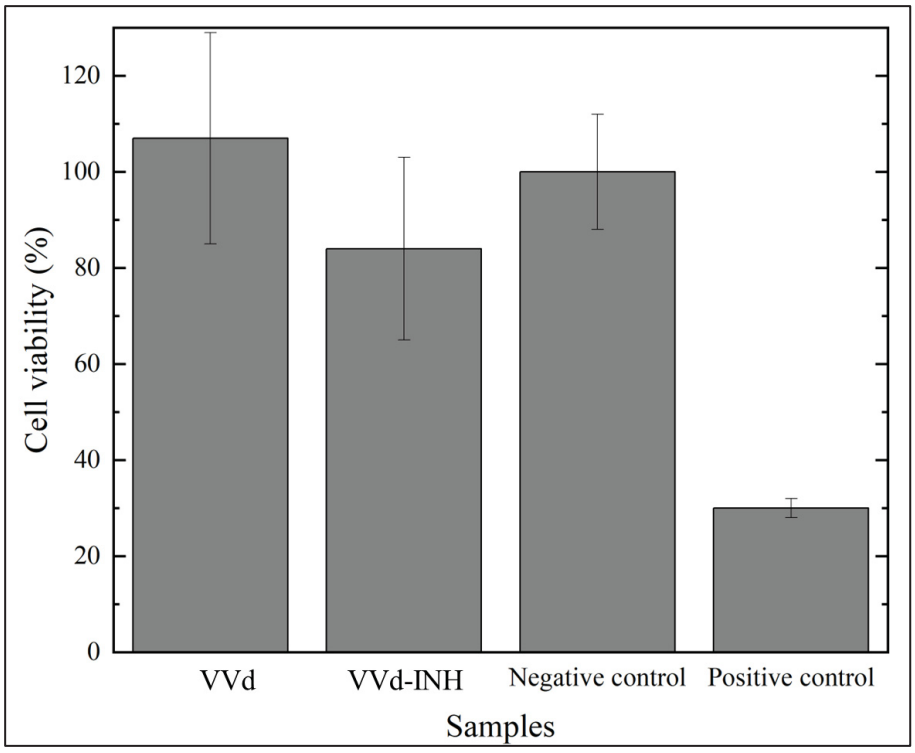

Figure 5.7 Cell viability of L929 fibroblasts exposed to extracts of VVd and VVd–INH (c), compared to negative and positive controls. Error bars represent standard deviation

These findings are critical in confirming the biosafety of the developed hybrid system, particularly for potential oral or topical administration. Given that VVd–INH (c) also showed the highest drug loading and the most sustained release profile, its non-cytotoxic behavior supports its suitability as a candidate for controlled-release tuberculosis therapy.

Furthermore, this result aligns with preclinical safety data for VVd: a 1.5 g/day dose has been reported safe in children (Mitchell et al., 2014), and adult rats tolerated up to 40 mg/kg/day without toxic effects (Maisanaba et al., 2015). Altogether, these findings reinforce that VVd–INH (c) is both effective in drug delivery and safe for further development as a drug delivery system for isoniazid.

5.3 Conclusions

This study provides new insights into the mechanisms of drug-clay interactions by investigating the adsorption and release behavior of isoniazid (INH) onto montmorillonite (VVd) under varying pH conditions. Through comprehensive structural, morphological, and thermodynamic analyses, we demonstrated that the mechanism of INH incorporation at pH 2 and pH 7 differs fundamentally, with direct implications for drug release performance.

At pH 7, where INH exists in a neutral state, adsorption occurred in two phases: (i) monolayer adsorption, reaching saturation at ~20 mg/g, characterized by strong surface binding; and (ii) multilayer deposition, enabling a total loading of up to ~110 mg/g. While multilayer incorporation increased drug content, it weakened drug–clay interactions and led to undesirable burst release, with ~20% of the drug released in acidic conditions. In contrast, monolayer adsorption, with stronger binding affinity, effectively prevented premature release in acidic media, a key requirement for oral drug formulations.

At pH 2, where INH is protonated, adsorption was driven by electrostatic attraction to the negatively charged clay surface. However, repulsion between protonated drug molecules restricted the system to monolayer adsorption (~100 mg/g), with no multilayer formation. This configuration resulted in minimal release at low pH (~8%) and produced a zero-order release profile at higher pH levels (6.8 and 7.4), indicating consistent, controlled drug delivery, a highly desirable characteristic for sustained-release systems.

Spectroscopic (FTIR) analysis revealed that INH interacts with clay surfaces via its hydrazine, pyridine, and carbonyl groups, binding to Si–O and O–H functional groups on the clay. TGA and DSC data confirmed that the clay matrix offers thermal protection, delaying drug degradation and preventing melting, consistent with strong drug–clay binding.

Together, these findings clarify the role of electrostatic and molecular interactions in defining both drug loading efficiency and release kinetics. The work provides a solid reference framework for future research involving neutral and cationic drugs and establishes a path toward the rational design of clay-based drug delivery systems, especially for oral formulations where acid stability is essential.

Moreover, the Brazilian natural clay (VVd) used in this study demonstrated no cytotoxicity, further supporting its potential as a cost-effective, safe, and scalable material for pharmaceutical applications, particularly for diseases like tuberculosis, where accessibility and affordability remain major global challenges.

Importantly, the adsorption process developed here, consisting of room temperature dispersion of clay in aqueous INH solution, is highly scalable and compatible with conventional pharmaceutical processing technologies. While industrial upscaling may introduce variables such as heat transfer and flow dynamics, these can be addressed through process optimization (e.g., mixing intensity and residence time) to ensure consistent performance at production scale.

CHAPTER 6

THE INFLUENCE OF CLAY SURFACE CHARGE ON INH INCORPORATION AND RELEASE

Jessica de Carvalho Arjona[a], Mazen Samara[b], Carina Ulsen[c], Francisco Rolando Valenzuela-Diaz[d], Nicole Raymonde Demarquette[e],

[a,c]Departamento de Engenharia Metalúrgica e de Materiais, Escola Politécnica, Universidade de São Paulo, Av. Professor Mello Moraes, 2463, São Paulo, SP 05508-030, Brazil
[a,b,d]Mechanical Engineering Department, École de Technologie Supérieure, 1100 R. Notre Dame O, Montréal, QC H3C 1K3, Canada
[c]Departamento de Engenharia de Minas e de Petróleo, Escola Politécnica, Universidade de São Paulo, Av. Prof. Mello Moraes, 2373, São Paulo, SP 05508-030, Brazil

Paper published in Materials Chemistry and Physics, October 2025.

6.1 Introduction

This chapter is based on a paper published in Materials Chemistry and Physics (de Carvalho Arjona, Samara, et al., 2025). Building upon the findings presented in Chapter 4, this section focuses on improving the drug adsorption capacity of CL (Cloisite) and LP (Laponite), the two clay samples that exhibited the lowest INH adsorption performance in our study. Notably, these samples also represent the extremes in pore volume, with CL having the lowest and LP the highest pore volume among all tested clays.

While INH adsorption and release at neutral pH were previously discussed, this chapter investigates the effect of environmental pH on drug incorporation and release behaviors for these clays. The results presented here reveal that, when compared to the literature, the INH–clay hybrids developed in this work demonstrate superior drug-loading efficiency and a more pronounced pH-responsive release behavior, particularly under acidic conditions (pH 2). This responsiveness is highly relevant for oral drug delivery applications, where protection from gastric acidity and subsequent release in the intestinal tract is essential to enhance drug bioavailability.

6.2 Results and Discussion

6.2.1 Zeta Potential

Table 6.1 summarizes the zeta potential measurements for CL and LP at pH 2 and 7. As expected, both clays exhibited negative zeta potential in acidic and neutral environments (Ghorbel-Abid et al., 2016). At pH 2, the zeta potential increased significantly, from -37.3 to -12.6 mV for CL and from -25.5 to -2.5 mV for LP. This behavior aligns with earlier studies (Ghorbel-Abid et al., 2016; M. Chorom & P. Rengasamy, 1995). The variation in zeta potential between CL and LP can be attributed to their mineralogical differences: CL is a montmorillonite-type clay, while LP is hectorite-type. These structural differences influence their chemical composition and the nature of isomorphic substitutions. In acidic pH, the increase in the surface charge can be explained by the replacement of Na^+ ions, which are naturally present in the clay's interlayer space, with H^+ ions. Due to their smaller ionic radius, H^+ ions can be more densely packed within the interlayer region and adsorbed more effectively onto negatively charged sites. This ion exchange leads to a more efficient neutralization of surface charges and a consequent reduction in the overall negative zeta potential (Delgado et al., 1986).

Table 6.1 Zeta potential of CL and LP at pH 2 and pH 7

Sample	pH 7		pH 2	
	Average (mV)	Dev.	Average (mV)	Dev.
CL	-37.3	1.8	-12.6	0.1
LP	-25.5	4.1	-2.5	0.7

6.2.2 Adsorption Studies

Figure 6.1 presents the INH adsorption isotherms of CL and LP at pH 2 and 7, measured at room temperature. The adsorbed INH per gram of clay (n_{ab}, mg/g) is plotted against the equilibrium concentration (C_e, mg/L). Error bars under ±4% indicate minimal variance. Adsorption capacity for both clays increased under acidic conditions, consistent with enhanced acid-base interactions (Almeida et al., 2019; Çalışkan Salihi et al., 2019; Damasceno Junior et al., 2019; Souza et al., 2021). CL adsorption rose from 15 to 115 mg/g, and LP, from 25 to 50 mg/g.

At pH 2, CL exhibited an H2-type curve and LP an L2-type curve, per Giles classification (C. H. Giles et al., 1960; Charles H. Giles & Smith, 1974). L2 curves signify reduced adsorption with increasing surface saturation, while H2 curves reflect strong adsorbate-adsorbent interactions, as observed for CL at $C_e < 685$ mg/L. Once monolayer capacity was reached, adsorption ceased due to electrostatic repulsion from the protonated INH layer (C. H. Giles et al., 1960; Charles H. Giles & Smith, 1974). The higher adsorption capacity of CL (115 mg/g) compared to LP (50 mg/g) correlates with zeta potential results, where more negative surface charges reduced electrostatic repulsion (Çalışkan Salihi et al., 2019).

At pH 7, CL exhibited an L3-type isotherm, while LP showed an S3-type curve. L3 isotherms are associated with stable adsorption of individual molecules or small clusters, whereas S3 isotherms indicate a predominance of cluster adsorption (C. H. Giles et al., 1960). This could explain LP's higher adsorption at pH 7. Initially, the drug fills a monolayer on the clay surface until saturation is achieved. Further addition of the drug forms additional multilayers, consistent with the findings of other works (Carazo et al., 2018b; De Carvalho Arjona et al., 2025). The shape of the adsorption curves varied depending on both the clay type and the pH of the environment (Figure 6.1). Indeed, pH influences the protonation state of the drug and the surface charge of the clay, thereby affecting their interaction. INH protonation appears to enhance drug–clay affinity, as reflected in the increased adsorption capacity observed at pH 2 and 7.

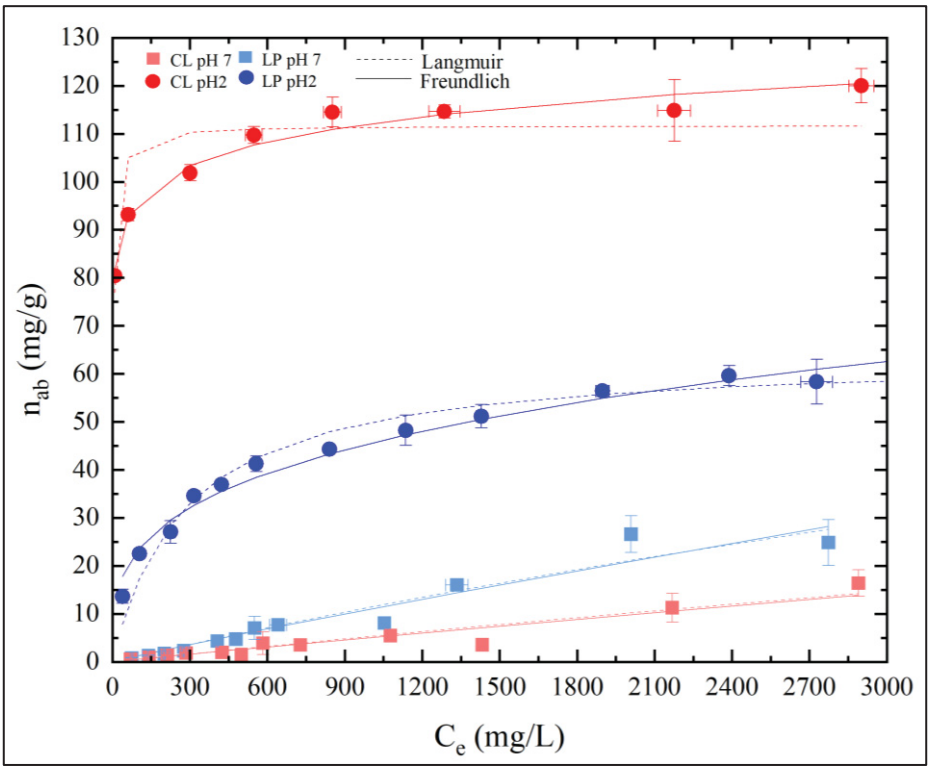

Figure 6.1 INH adsorption isotherms for CL and LP at pH 2 and pH 7. The adsorption data of LP and CL were discriminated by the colors blue and red, respectively, while squares and circles represent the hybrids made at pH 7 and 2, respectively

The adsorption results were analyzed by fitting them into two different models: the Langmuir and the Freundlich models. The fitted parameters for these models are presented in Table 6.2. The experimental data fitted better into the Freundlich model, indicating that adsorption occurred on a heterogeneous surface, consistent with the clay's structure.

Table 6.2 Adsorption parameters of isoniazid (INH) fitted using Langmuir and Freundlich models for CL and LP clays at pH 2 and pH 7

Clay			**CL**		**LP**	
pH			**2**	**7**	**2**	**7**
Model	Langmuir	K_L (L/mg)	0.2561	$4.0\ 10^{-5}$	0.0036	0.0001
		Q_m (mg/g)	111.7226	133.9961	64.0037	136.8915
		R_L	0.0338	0.9945	0.8147	0.9877
		R^2	0.7420	0.9138	0.9674	0.9375
	Freundlich	K_F	70.4641	0.0070	6.1457	0.0186
		N_F	14.8634	1.0500	3.4473	1.0822
		R^2	0.9747	0.9192	0.9807	0.9312

6.2.3 Drug Release Tests

To simulate oral drug release, the INH *in vitro* release profile from CL and LP was evaluated in three media with varying pH: gastric buffer (pH 2) and intestinal buffers (pH 6.8 and 7.4), as shown in Figure 6.2 (a). Only samples prepared at pH 2 were used due to their higher adsorption capacity compared to those prepared at pH 7. The cumulative release profiles are expressed as percentages. Consistently small error bars for all samples indicate high precision and reliability. CL/INH exhibited steadily lower cumulative release than LP-INH for all investigated pH levels, particularly at pH 2, where CL showed greater INH affinity. Similar results were observed by other researchers as well, using montmorillonite as a carrier for INH and other drugs (Calabrese et al., 2013; De Carvalho Arjona et al., 2025; Sciascia et al., 2021). The cumulative release of INH increased with pH, reflecting weaker clay-drug interactions. CL released 40% of INH adsorbed, while LP released 55%, with neither hybrid achieving full release; the percentages refer to the values of INH adsorbed. The stronger adsorption of INH when using CL likely explains its lower release compared to LP.

To eliminate carryover effects between pH conditions, the release test was performed by exposing the samples separately to pH 2.0 and pH 7.4 for 5 hours each. Figure 6.2 (b) and (c) show, respectively, the release of INH by LP/INH and CL/INH during 5 hours at pH 2

and 7.4. In this study, we managed to remove the influence caused by the previous environment on the release. As can be seen, for both clays, the release at pH 2 followed the tendency observed in the oral release curve, Figure 6.2 (a). At the beginning of the release, the INH reached a plateau, and no further release was observed. This result corroborates the adsorption at pH 2. Drug protonation influenced the interaction between the cationic drug and the clay's negative surface charge. As was observed, the lower the clay surface charge, as in CL, the lower the drug release in acidic pH. Indeed, for CL which presented a surface charge of -12.6 mV the release was less than 10% while for Laponite, which presented a surface charge of -2.5 mV, the release was 25%. At pH 7.4, for both clays, as expected, the release of the drug increased due to the neutralization of isoniazid and reduced electrostatic interactions. Although few studies have reported on pH-responsive release for comparable systems, the available data suggest our formulation exhibits improved release behavior. For example, Murath et al. (2023) (Muráth et al., 2023) reported pH-dependent release of valsartan and atorvastatin from LDH, with limited release at acidic pH and a slight increase after 5–6 minutes. Zauska et al (2022) (Zauška et al., 2022) observed that the acidic form of naproxen had strong interactions with negatively charged surfaces, limiting its release across pH levels. In the case of isoniazid, zeolites released the drug entirely within 10 minutes with no further increase (Souza et al., 2021). In contrast, the clay-based systems investigated here demonstrated a more sustained and controlled release profile, suggesting potential for enhanced therapeutic performance.

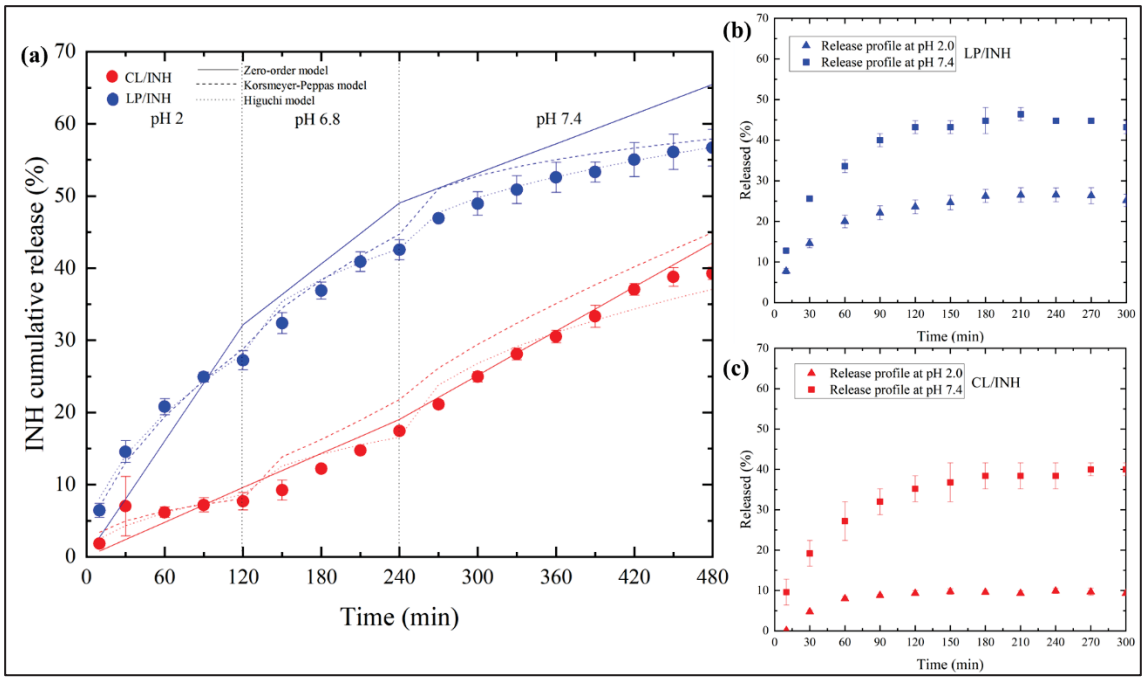

Figure 6.2 INH release profiles from CL-INH (red) and LP-INH (blue) hybrids. (a) The release test simulated the oral gastrointestinal pathway, with the medium adjusted to pH 2.0 for 0–120 min, pH 6.8 for 120–240 min, and pH 7.4 for 240–480 min. (b) and (c) show the release profiles at a single pH medium for 300 min, using LP and CL, respectively. Squares represent release at pH 7.4, while triangles indicate release at pH 2.0

Table 6.3 summarizes the cumulative amount of INH released per gram of clay over time for both hybrids studied in the present work. At the end of the release test, CL released approximately 43 mg/g, while LP released 31 mg/g. Within the first 120 minutes, at pH 2, LP released approximately 15 mg/g of INH, accounting for nearly 50% of the total drug release. In contrast, during the same period, the release of CL-INH was less than 20% of the total amount released, demonstrating a more prolonged release profile. While other carriers such as nanoparticles of silica (Almeida et al., 2019) and palygorskite (Damasceno Junior et al., 2019), have shown controlled release behavior, they achieved a lower cumulative amount of drug compared to our system. Zeolite carriers exhibited pH-responsive behavior; however, the drug was almost completely released within 10 minutes,

with no further increase observed thereafter (Souza et al., 2021). For LDHs, only minimal pH-dependent differences were reported, likely due to testing at pH 4.8, where the protonation effect is less pronounced (Saifullah et al., 2016). Collectively, these comparisons underscore the relevance of our findings: the clay-based systems studied here combine sustained release with higher cumulative drug delivery, offering a potentially more effective platform for oral drug administration.

Table 6.3 The release of INH in mg/g for the two hybrids studied in oral drug release media: <120 min, pH 2, simulating stomach environment; 120 min < t < 240 min, at pH 6.8, simulating first part of small intestine; t > 240 min, at pH 7.4, simulating the second part of small intestine

Time	pH	CL/INH		LP/INH	
		INH released (mg/g)	S.D.	INH released (mg/g)	S.D.
10	2.0	2.0	0.0	3.5	0.0
30		7.7	0.3	7.9	0.1
60		6.8	0.0	11.2	0.1
90		7.9	0.1	13.5	0.1
120		8.5	0.1	14.7	0.2
150	6.8	10.2	0.1	17.5	0.3
180		13.5	0.1	19.9	0.2
210		16.3	0.1	22.1	0.3
240		19.2	0.0	23.0	0.3
270	7.4	23.3	0.1	25.3	0.0
300		27.5	0.2	26.4	0.4
330		31.0	0.3	27.5	0.5
360		33.6	0.3	28.4	0.6
390		36.7	0.6	28.8	0.4
420		40.8	0.3	29.7	0.7
450		42.7	0.6	30.3	0.7
480		43.3	0.4	30.6	0.8

The release data were fitted to 3 models: zero-order, Korsmeyer-Peppas, and Higuchi. The fitted parameters are provided in Table 6.4. For CL/INH, at pH 2, none of these models fit the data adequately ($R^2 < 0.670$). For LP/INH, the Higuchi model provided the best fit ($R^2 = 0.984$). The release for CL/INH at pH 6.8 was best described by the zero-order model ($R^2 = 0.999$). At pH 7.4, the release data for both hybrids fit the Higuchi model best, indicating that the driving force for release was diffusion, $R^2 > 0.990$. Release behavior was pH-

dependent for both clays, though CL was more sensitive to pH changes. At pH 2, CL released only 8% of INH within the first 2 hours, compared to 25% for LP. This suggests that CL offers enhanced protection for INH in acidic environments, releasing more in response to pH changes. At pH 2, the release profile of CL-INH plateaued within 30 minutes, with no model providing a strong fit. At pH 6.8, CL-INH followed a Zero-order model, indicating a constant release rate independent of drug concentration. In contrast, LP-INH release was diffusion-driven, fitting the Higuchi model. These findings highlight the significant role of clay-drug interactions and release conditions in controlling INH release, with CL providing greater stability in acidic environments compared to LP.

Table 6.4 Release fitting of CL/INH and LP/INH hybrids made at pH 2 and 7

Release pH	Hybrid	Zero Order		Korsmeyer-Peppas			Higuchi	
		K_o	R^2	k_1	n	R^2	K_o	R^2
pH 2.0	CL/INH	0.080	0.557	1.516	0.349	0.706	0.788	0.670
	LP/INH	0.268	0.922	1.884	0.570	0.978	2.567	0.984
pH 6.8	CL/INH	0.079	0.999	0.032	1.195	0.995	1.324	0.990
	LP/INH	0.141	0.964	0.450	0.744	0.979	0.905	0.996
pH 7.4	CL/INH	0.102	0.978	0.290	0.799	0.987	1.324	0.990
	LP/INH	0.069	0.976	1.877	0.356	0.994	0.905	0.996

6.2.4 TGA

Figure 6.3 displays the TGA curves for the pristine clays and their respective hybrids. The weight loss of the clays occurred in three major steps: first, due to the loss of surface water molecules; second, from the loss of hydration water, and finally, due to dehydroxylation (Esperanza Carazo et al., 2018). The TGA curves for CL/INH and LP/INH exhibited additional degradation steps due to the incorporation of INH.

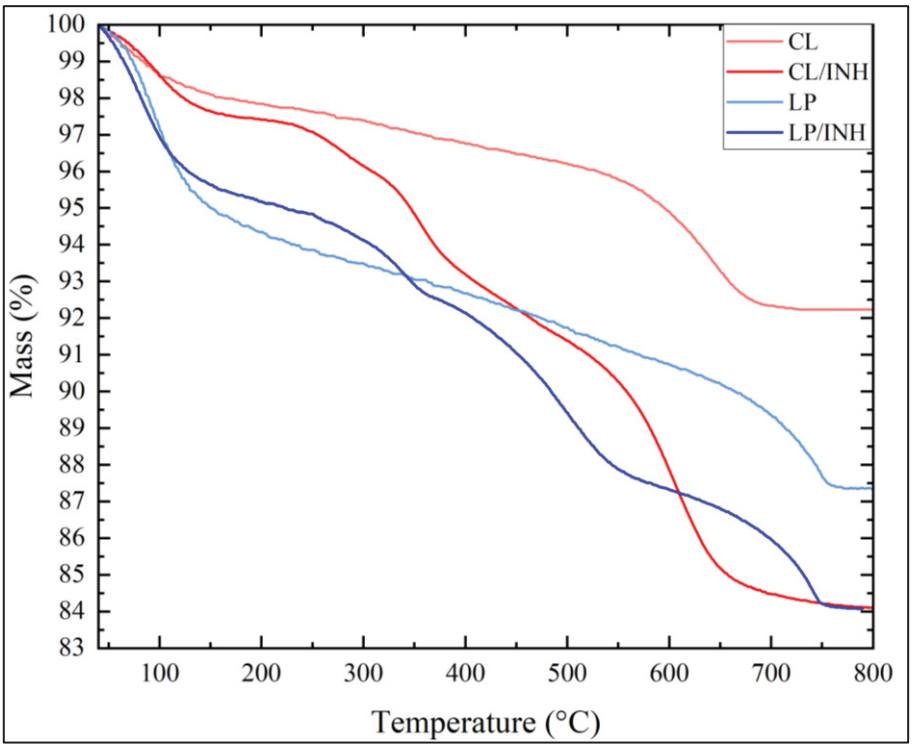

Figure 6.3 TGA of pristine clays and their respective hybrids made at pH 2

The mass loss of pristine clays and their respective hybrids is summarized in Table 6.5. The weight loss during the first stage of clay degradation was similar for each clay and its corresponding hybrid. Most differences emerged in the second stage: CL lost 3.1% of its mass, and CL/INH lost 7.1%. Similarly, LP lost 6.2%, while LP/INH lost 10.4%. This increase in weight loss can be attributed to the degradation of INH by around 220 °C (de Carvalho Arjona et al., 2024).

Table 6.5 Weight loss of CL, LP, and their hybrids

Stage	CL		CL/INH		LP		LP/INH	
	Temp. range (°C)	**Weight loss (%)**	**Temp. range (°C)**	**Weight loss (%)**	**Temp. range (°C)**	**Weight loss (%)**	**Temp. range (°C)**	**Weight loss (%)**
1st stage	40 – 110	1.5	40 – 146	2.3	40 – 133	4.5	40 – 121	3.8
2nd stage	120 – 579	3.1	146 – 237	0.5	133 - 705	6.2	121 - 309	2.2
			237 – 340	2.0			309 - 356	1.3
			340 – 554	5.1			356 - 548	4.8
							548 - 706	2.1
3rd stage	579 – 684	3.0	554 – 657	5.2	705 - 756	1.9	706 - 751	1.6

Figure 6.4 shows the DTG curves for INH, pristine clays, and their respective hybrids. The degradation of INH occurred with two peaks at approximately 237 °C and 305 °C. The curves for the pristine clays exhibited only two peaks, corresponding to the mass loss of surface water, around 100 °C, and dehydroxylation, around 636 °C and 730 °C, for CL and LP, respectively. For CL/INH, the emergence of a peak around 356 °C and the downward shift of dehydroxylation from 639 to 600 °C are likely attributable to the overlapping of the decomposition of INH and the dehydroxylation process. In the case of LP/INH, two peaks appeared around 346 and 505 °C for the same reason (Joshi et al., 2010). This phenomenon, the increase of INH degradation, may have occurred due to the thermal protection provided by LP and CL, which enhanced the degradation of INH. Similar results were observed in other studies as well (Souza et al., 2021). According to these studies, the peak around 350 °C corresponds to the degradation of weakly adsorbed INH, while the degradation observed at higher temperatures indicates that a portion of INH is strongly bound to the clay particles.

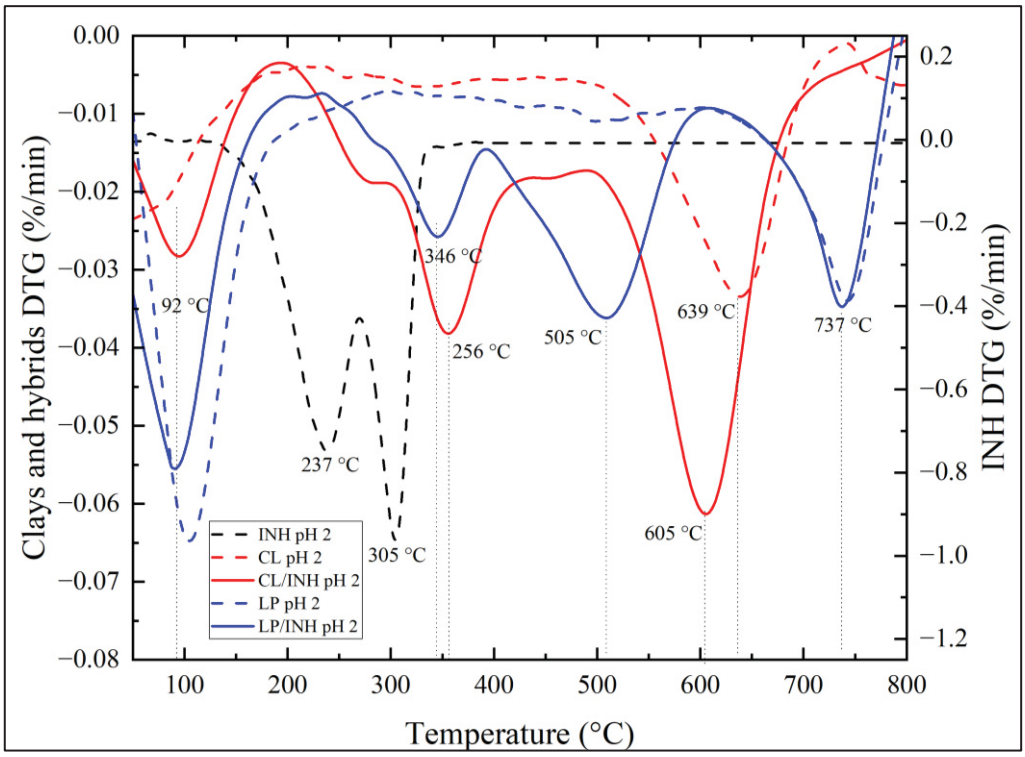

Figure 6.4 DTG of LP, LP/INH, CL, and CL/INH prepared at pH 2, and DTG of INH after being treated at pH 2

6.2.5 FTIR

The FTIR spectra of INH, pristine clays, and their respective hybrids are shown in Figure 6.5. The CL/INH spectra exhibited more prominent INH bands than the LP/INH spectrum, which can be attributed to the higher amount of INH incorporated by the former. The bands 751, 851, 1324, and 1681 cm^{-1} were common to both hybrids, while CL/INH also presented the bands around 1545, 1496, and 891 cm^{-1}. Additionally, the Si-OH peaks for both clays shifted after INH incorporation: from 995 to 1013 cm^{-1} for LP, and from 999 to 1004 cm^{-1} for CL. Furthermore, the peak at 1681 cm^{-1} that appeared in both hybrid spectra corresponds to a band shift of 1663 cm^{-1} of INH indicating the interaction between the clay and INH (Akyuz & Akyuz, 2008; Esperanza Carazo et al., 2018). The INH bands in both clay/INH spectra indicated an interaction between the drug and the clays. The band around 1663 cm^{-1}, attributed to amide carbonyl vibrations of INH, shifted to 1683 cm^{-1} for both hybrids. This positive shift suggests the formation of H-bonds between the drug and clay. The band shifted around 1000 cm^{-1} in both clays to 1004 for CL and 1013 cm^{-1} for LP, further

indicating an interaction between drug and siloxane clay groups (Si-O-Si) (Almeida et al., 2019). The bands around 1545 and 1496 cm^{-1} can be assigned to the ring stretching vibration while the bands around 851 and 751 cm^{-1} may be assigned to the out-of-plane deformation modes of the aromatic ring (Souza et al., 2021). Previous studies have reported similar findings, indicating that exo and endo-cyclic nitrogen atoms were involved in the interaction between clay and INH (Akyuz & Akyuz, 2008; Esperanza Carazo et al., 2018). More INH bands appeared in the CL/INH spectrum than in the LP/INH spectrum due to the higher amount of INH incorporated in the CL hybrid.

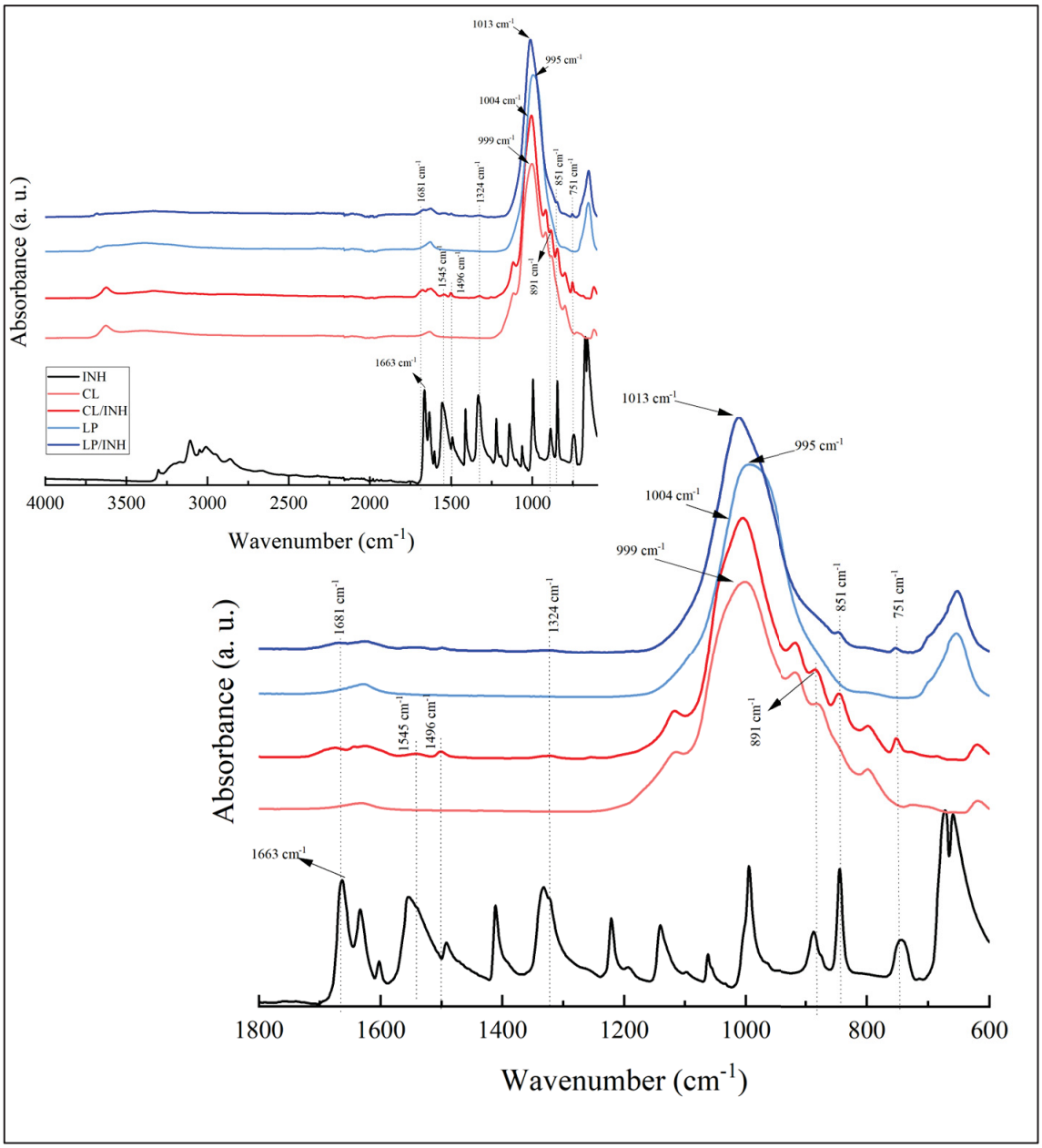

Figure 6.5 FTIR spectra of INH, CL, LP, CL/INH, and LP/INH at pH 2

6.2.6 XRD

Figure 6.6 displays the XRD patterns for INH, pristine clays, and their respective hybrids. None of the diffractograms for the clay-drug hybrids show the initial peaks of INH, as was observed in other studies (Esperanza Carazo et al., 2018) , which may suggest that the drug did not crystallize on the clay surface. The basal peak of CL shifted from 1.18 nm to 1.28 nm, while the basal peak of LP did not exhibit a change. Similar results were found in other

studies (Calabrese et al., 2013). When comparing pristine clays and their hybrids, the 001 reflection (2θ ≈ 7°) appears more defined after INH incorporation. The narrowing of this peak suggests enhanced structural organization, possibly due to physicochemical interactions between the clay and the drug. This interaction may promote partial rearrangement of the clay platelets, even in the absence of a significant increase in interlayer spacing, indicating that a portion of the drug might be intercalated between the layers. Additionally, the 001 peak of LP is broader than that of CL, which is consistent with its smaller platelet size and reduced preferred orientation along the z-axis.

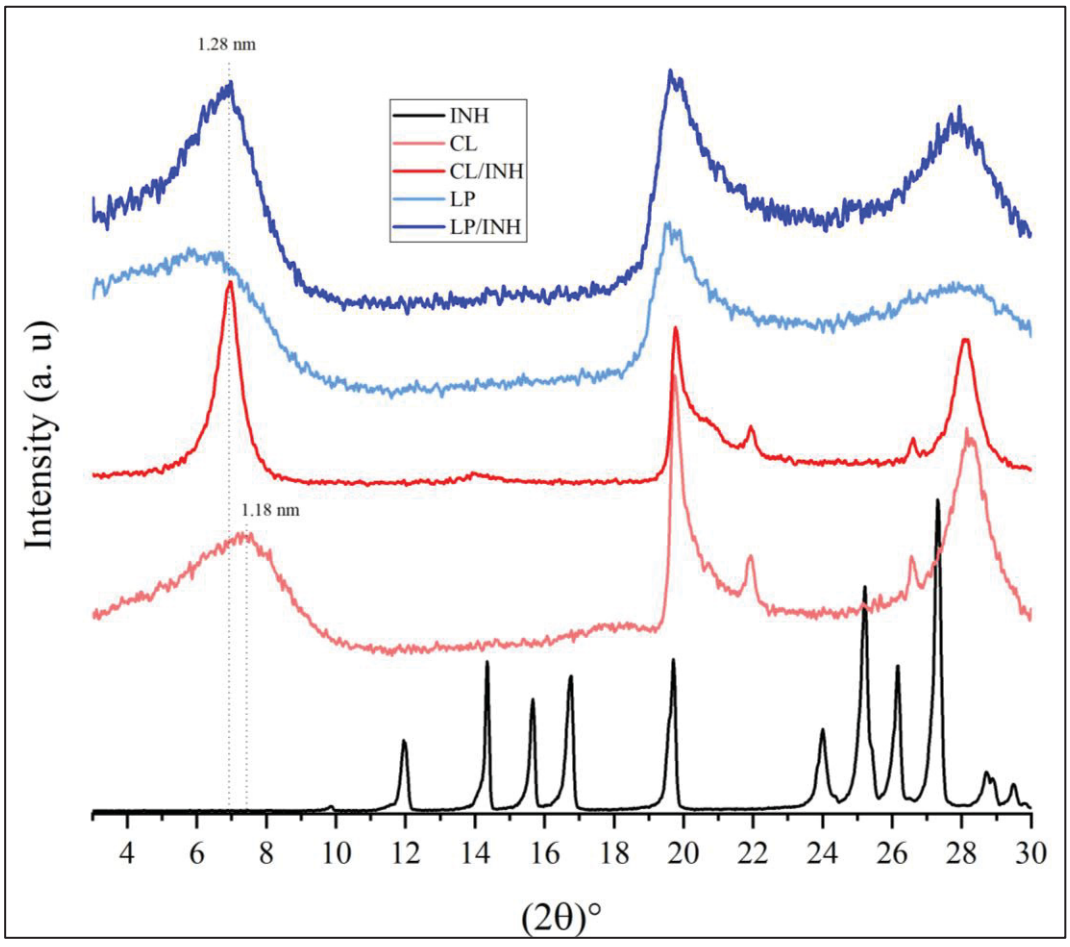

Figure 6.6 XRD patterns of CL and LP clays and hybrids made at pH 2

6.3 Conclusion

Two types of clays, cloisite (CL) and laponite (LP), were investigated for isoniazid (INH) adsorption and release efficiency, with CL being found to be superior to LP. INH adsorption by CL at pH 2 resulted in a significant adsorption ratio of mg/g compared to pH 7 due to an acid-base attraction. Minimal release by this clay was observed at a pH of 2, corresponding to the stomach conditions (around 8% of the drug incorporated, 9 mg/g), and this was prolonged for up to 5 hours. In the case of LP, around 25% of the drug was released at the same pH. This shows that the pH had a higher effect in CL, probably due to its lower surface charge, increasing the interaction with INH. For the same reason, the CL/INH hybrid showed an excellent adsorption ratio of 115 mg/g, and superior release at pH 6.8 and 7.4, corresponding to the conditions of the small intestine following the zero-order model. The importance of the interaction between the carrier and the drug was demonstrated by comparing clays with the same physical structure (pillared lamellas), but different chemical compositions. The protonation effect was utilized to maximize the drug intake into CL and LP at a pH equal to 2 while minimizing drug release in the stomach at the same pH.

Despite the promising results presented here, several limitations should be acknowledged. For instance, the potential for clay aggregation under physiological conditions and its effect on drug release and bioavailability remain to be investigated. Additionally, although the *in vitro* release studies are encouraging, further biological validation is required, including cytotoxicity assays, biocompatibility assessments, and *in vivo* evaluations to confirm the safety and efficacy of these systems. Future studies could also incorporate computational modeling to gain deeper insight into the interaction mechanisms between INH and clay surfaces at the molecular level. Such understanding would support the rational design and optimization of next-generation clay-based drug delivery platforms.

CHAPTER 7

PULLULAN MODIFICATION FOR ISONIAZID DRUG RELEASE

7.1 Introduction

In this final chapter presenting experimental results, pullulan-based hydrogels were investigated as potential drug delivery vehicles for isoniazid (INH). Before their application in release studies, the chemical modification of pullulan (Pul) was systematically evaluated to ensure the reproducibility and consistency of the process. The modified pullulan was characterized using Fourier-transform infrared spectroscopy (FTIR) and proton nuclear magnetic resonance (^{1}H-NMR) to confirm successful functionalization.

Following this, the resulting hydrogels were subjected to rheological analyses to assess the influence of UV exposure time and crosslinking density on their mechanical properties. Swelling behavior was also evaluated to determine the hydrogels' capacity for fluid absorption under physiological conditions. Based on these results, three hydrogel formulations were selected for INH release testing, conducted at pH 7.4 over 24 hours, simulating conditions relevant to intestinal drug delivery.

This chapter presents a comprehensive analysis of the synthesis, characterization, and performance of pullulan-based hydrogels, highlighting their potential as biocompatible, tunable platforms for controlled drug release applications.

7.2 Results and Discussion

7.2.1 Pullulan modification

The modification of Pul with methacrylic anhydride (MA), as described in Sections 1.2.4 and 3.3.6 sections, led to the formation of methacrylated pullulan, referred to in this study as PulMA. Three different concentrations of MA were used in the reaction: 0.5%, 1.5%, and 3.0% (v/v). The resulting materials were designated PulMA05, PulMA15, and PulMA30, respectively. To confirm the success of the chemical modification, the samples were analyzed by Fourier-transform infrared spectroscopy (FTIR). Their spectra are presented in Figure 7.1. Pristine Pul presented the characteristic bands at 3375, 2929, and 1638 cm^{-1}, which respectively correspond to O-H stretching, C-H stretching, and C-C

stretching (Hernandez-Tenorio & Giraldo-Estrada, 2022; Zeng et al., 2020) and bands around 1175 and 1030 corresponding to C-O-C and C-O stretching vibration modes (Hernandez-Tenorio & Giraldo-Estrada, 2022; W. Zheng et al., 2022).

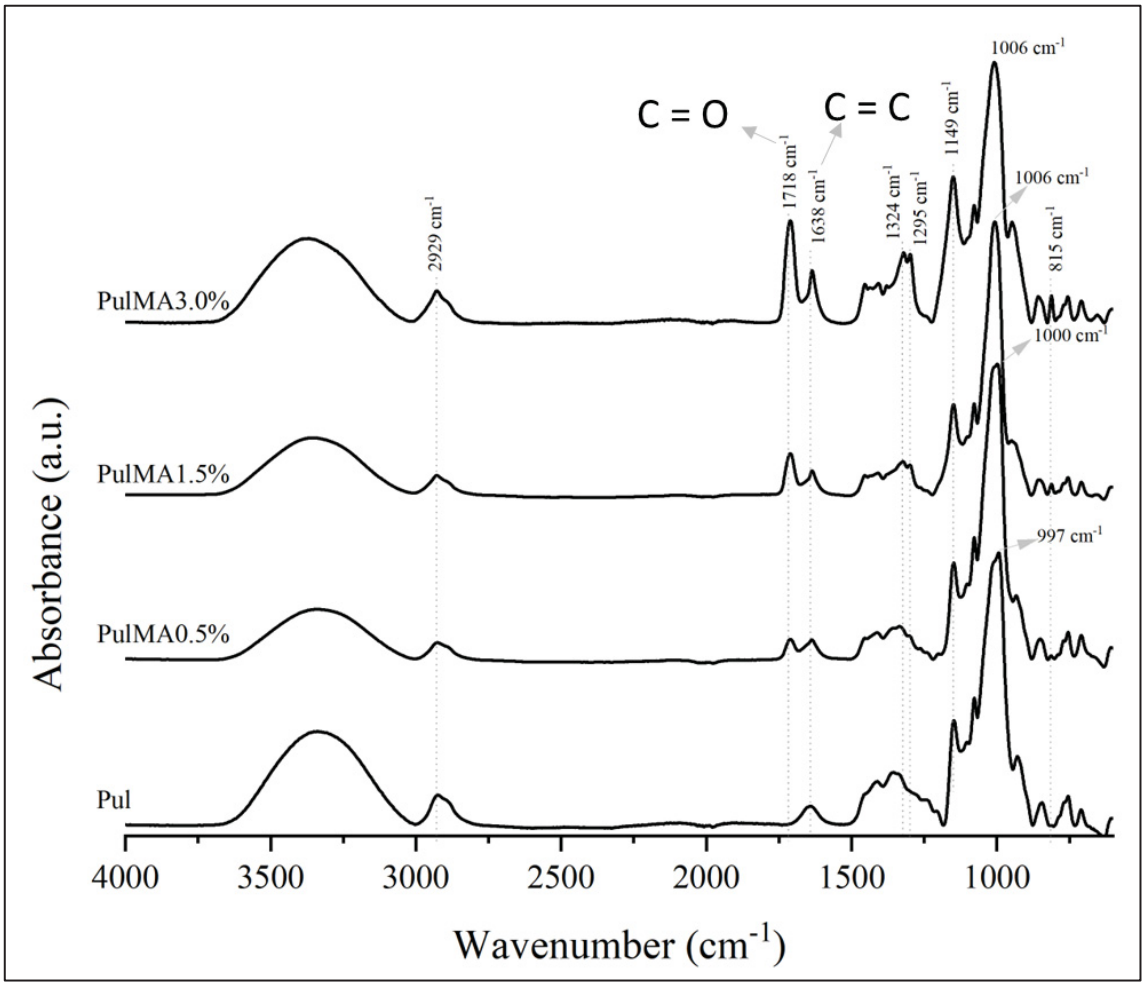

Figure 7.1 FTIR spectra of Pullulan and PulMA 0.5%, 1.5%, and 3.0%

The spectral differences between pristine Pul and PulMAs are consistent with the introduction of methacrylate functional groups, as summarized in Table 7.1. Compared to pristine Pul, the PulMA spectra exhibited several distinct spectral changes, particularly in the regions around 2929 cm^{-1} (C–H stretching of methacrylate CH_2/CH_3), 1700–1600 cm^{-1} (due to C=O stretching of the ester carbonyl group and C=C stretching of vinyl group), 1500–1250 cm^{-1} (CH_3 bending vibrations), and near 1000 cm^{-1} (possibly due to overlapping vibration from ether bonds and MA groups), along with the appearance of a new band at approximately 815 cm^{-1}. These observations are consistent with previous work

(Bae et al., 2011; Hernandez-Tenorio & Giraldo-Estrada, 2022; Mugnaini et al., 2021; Nonsuwan et al., 2023; W. Zheng et al., 2022). The increasing intensity of these peaks with higher MA concentrations supports the progression of the modification reaction. While FTIR was not used to quantify the degree of substitution, it served as qualitative confirmation of successful methacrylation and was consistent across replicates.

Table 7.1 FTIR spectral changes in PulMA samples relative to pristine pullulan

Wavenumber (cm^{-1})	**PulMA Observation**	**Band Assignment**	**Reference**
~2929	Increased intensity and changed shape	C–H stretching of methacrylate CH_2/CH_3	(Hernandez-Tenorio & Giraldo-Estrada, 2022; Zeng et al., 2020)
~1720	New band	C=O stretching of the ester carbonyl group	(Bae et al., 2011; Mugnaini et al., 2021; Nonsuwan et al., 2023)
1635–1615	New/shoulder band	C=C stretching (vinyl group)	(Bae et al., 2011; Nonsuwan et al., 2023)
1450–1370	New peaks	CH_3 bending vibrations	(Hernandez-Tenorio & Giraldo-Estrada, 2022; Mugnaini et al., 2021)
~1000 (shifted)	Slight upshift in C–O–C peak	Ether bond vibrations	(Hernandez-Tenorio & Giraldo-Estrada, 2022)
~815	New peak	(1->4) and (1->6) linked alpha-d-glucose units and alpha configuration	(Hernandez-Tenorio & Giraldo-Estrada, 2022)

As explained in the methodology section, three different batches of PulMA were made, and in all of them, the respective PulMA 0.5%, 1.5%, and 3.0% presented similar band peaks. The spectra of PulMA 2nd and 3rd can be seen in Appendix I.

To quantify the degree of methacrylation of PulMA, ^{1}H NMR spectroscopy was employed. The spectra of both pristine Pul and first batch modified PulMA are presented in Figure 7.2 (the spectra of 2nd and 3rd batch PulMA can be found in Appendix II. In the spectrum of pristine pullulan, several characteristic proton signals were observed: the signal at 5.32 ppm corresponds to the H1 proton; 5.28 ppm is attributed to α(1→4) glycosidic bonds; and 4.88 ppm is assigned to anomeric protons from α(1→6) linkages. Peaks at 3.78 and 3.81 ppm

correspond to the H6 protons of glucose units B and C in α(1→4) linkages, while the signal at 3.87 ppm represents the H6 proton involved in α(1→6) linkages. The broad multiplet between 3.95 and 3.38 ppm is attributed to the H2, H3, H4, and H5 protons of the glucose backbone. The solvent peak of D_2O appears at 4.80 ppm, and a residual DMSO peak from the purification step is observed at 2.71 ppm (Bae et al., 2011; Hernandez-Tenorio & Giraldo-Estrada, 2022; Mugnaini et al., 2021; Nonsuwan et al., 2023; Qin et al., 2021).

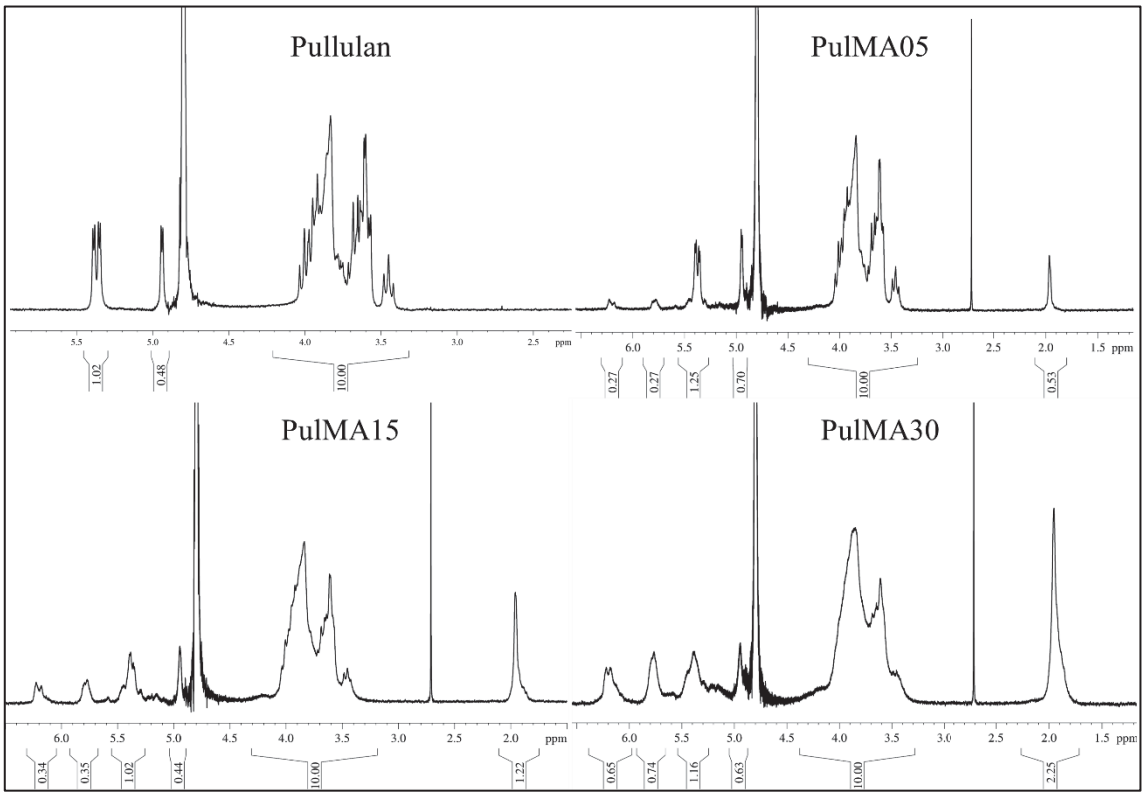

Figure 7.2 H-NMR spectra of Pullulan, PulMA 0.5%, PulMA 1.5%, and PulMA 3.0%

The PulMA spectra closely resembled that of pristine Pul, with additional signals confirming the successful grafting of methacrylate groups for all the initial MA concentration products and all PulMA batches. New peaks appeared around 6.2 and 5.8 ppm, corresponding to the vinyl protons (–$CH=CH_2$), and a signal near 1.9 ppm was assigned to the methyl protons (–CH_3) of the methacrylate group. As higher was the MA initial concentration, the higher the intensity of these groups' peaks. These spectral features

were consistently observed across all PulMA batches and agree with previous reports in the literature (Bae et al., 2011; Hernandez-Tenorio & Giraldo-Estrada, 2022; Mugnaini et al., 2021; Nonsuwan et al., 2023; Qin et al., 2021).

As discussed in Section 1.2.4, various methods for calculating the degree of methacrylation can be found in the literature, which may explain the inconsistencies among reported results. To enable comparison with previous studies, the degree of methacrylation for each batch, at each initial MA concentration, was also calculated using the equations presented in Table 7.2, which can be found in the literature. The results are also summarized in Table 7.2. As observed, increasing the initial concentration of methacrylic anhydride (MA) consistently led to a higher degree of methacrylation across all calculation methods. Additionally, each batch showed a low standard deviation, indicating that the methacrylation reaction is reproducible, which is an essential criterion for biomedical applications.

Table 7.2 PulMA substitution degree equations found in the literature and their results regarding PulMA obtained in this work

Ref.	Equation		PulMA substitution degree (%)					
			0.50%		1.50%		3.00%	
			SD av.	dev.	SD av.	dev.	SD av.	dev.
(Bae et al., 2011)	$\frac{I_{1.9}+I_{5.8}+I_{6.2}}{I_{3.3-4.1}+I_{4.9}+I_{5.3}}$	(7.1)	7.10	1.90	17.20	1.60	30.40	2.30
(Della Giustina et al., 2019)	$\frac{7(I_{1.85}+I_{5.7-5.9}+I_{6.1-6.3}}{5(I_{3.3-4.1}+I_{4.8-5.0}+I_{5.2-5.}}$	(7.2)	10.00	2.70	24.10	2.30	42.50	3.20
(Mugnaini et al., 2021)	$\frac{6I_{1.9}}{I_{4.02-3.35}}$	(7.3)	0.32	0.03	0.75	0.07	1.33	0.1
(Qin et al., 2021)	$\frac{I_{5.71-6.28}}{I_{4.92-5.51}}$	(7.4)	17.80	8.90	49.90	4.90	82.70	6.40
(Nonsuwan et al., 2023)	$\frac{I_{5.71-6.15}+I_{5.2}+I_{5.6}}{I_{5.38-4.44}}$	(7.5)	13.00	3.00	16.70	0.70	22.70	1.70

Other studies, such as those by Bae et al., (2011), Della Giustina et al. (2019), and Mugnaini et al. (2021), also prepared PulMA using the same initial methacrylic anhydride (MA) concentration of 0.5%, reporting methacrylation degrees of 6.4%, 3.38%, and 27%, respectively. In comparison, our result of 7.10% ± 1.90% aligns closely with the value reported by Bae et al. (2011). Their study also investigated PulMA synthesized with 1.5% MA, yielding a methacrylation degree of 16.5%, which is comparable to our result of 17.2% ± 1.6%. These similarities support the reproducibility and reliability of the methodology used in this work.

In addition to employing the same calculation methods used in previous studies, this work also proposes a new approach based on NMR quantification guidelines. To calculate the degree of substitution, a single reference peak was selected: the signal at 5.3 ppm, corresponding to the H1 proton of the glucose unit (Figure 7.3). This proton was chosen because its amount in the pullulan backbone remains constant regardless of the degree of methacrylation, due to its bonding to a carbon atom, not an oxygen. To validate this assumption, the pullulan spectrum was used as a reference. The intensity of the H1 peak was compared to the total intensity of the sugar region (4.4–3.3 ppm), and the resulting

ratio was found to be approximately 10.2%. This same analysis was applied to the PulMA spectra, and the results are presented in Table 7.3, confirmed that this ratio remains constant, independent of the extent of methacrylate incorporation. For calculating the methacrylation (or substitution) degree (SD), the vinyl group (signals at ~5.8 and ~6.2 ppm) was chosen, as represented by equation (7.6). The ratio of these signals to the H1 peak intensity was found to be consistent across all PulMA samples, indicating that either group can be reliably used for SD determination in this type of modified polysaccharide.

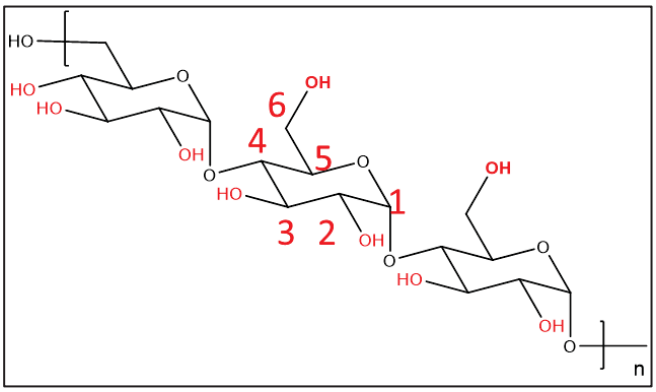

Figure 7.3 Pullulan chemical structure and hydrogen numbering

$$SD_{vynil} = \frac{\frac{I_{6.3-6.1} + I_{5.8-5.9}}{2}}{I_{5.5-5.2}} \tag{7.6}$$

Although several calculation approaches have been proposed in the literature, the method adopted in this study provides greater accuracy and consistency under our experimental conditions. This approach considers all characteristic vinyl proton signals (around 5.8 and 6.2 ppm), avoids overlapping with solvent or backbone signals, and ensures a more reliable quantification of methacrylate incorporation. For this reason, it was selected as the primary method for analyzing the methods of methacrylation efficiency in this work.

Table 7.3 ^{1}H-NMR results showing the calculated ratios used to determine the methacrylation degree for each PulMA batch, using the vinyl and methyl groups as methacrylate markers and the H1 proton of the pullulan backbone as the reference.

	Correlation H1/Sugar units		**Vinyl group/H1**	
PulMA	**SD average**	**dev.**	**SD average**	**dev.**
0.5%	10.7%	1.3%	13.2%	6.9%
1.5%	10.2%	0.0%	35.7%	3.3%
3.0%	10.8%	0.5%	60.5%	4.1%
Pullulan	10.0%	-	-	-

Accurate determination of the degree of methacrylation is essential for ensuring reproducibility across batches and for tuning the physicochemical properties of the final hydrogels, such as mechanical strength, swelling behavior, and drug release profile. The methodology proposed here, based on a structurally invariant reference (H1 proton) and well-resolved methacrylate peaks, minimizes the influence of overlapping signals or baseline inconsistencies commonly observed in broader integration methods reported in the literature. While care must still be taken to avoid interference from residual solvents near the methyl region, this approach offers a reliable and reproducible alternative for quantifying substitution in methacrylated pullulan, particularly in the context of biomedical applications.

7.2.2 Hydrogel formulation

To evaluate the processability of PulMA-based hydrogels under UV exposure, rheological tests were performed to determine the gel point and assess the degree of crosslinking, as described in (3.11). Three key parameters were investigated for their impact on hydrogel performance: UV exposure time, polymer concentration in water (10% and 20% w/v), and the degree of methacrylation (substitution degree) of PulMA.

Figure 7.4 presents the evolution of the storage modulus (G′) and loss modulus (G″) over time for PulMA with a 0.5% substitution degree at 20% (w/v) concentration. To evaluate the effect of UV exposure duration, the light source was activated at the beginning of the test and turned off at three different time points: after 1 minute, after 10 minutes, and at the

end of the test (15 minutes). An additional control test was performed with the UV lamp kept off throughout the entire experiment.

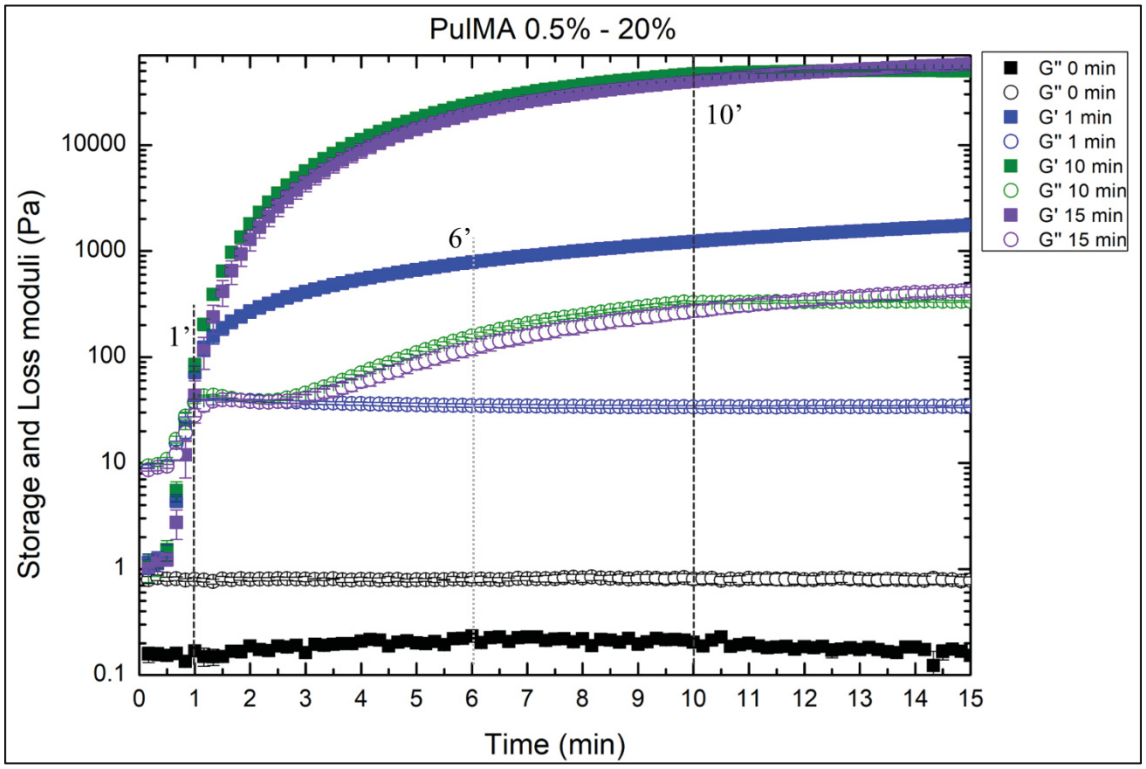

Figure 7.4 Time-dependent evolution of storage (G') and loss (G") moduli for a 20% (w/v) PulMA solution with 0.5% substitution degree, under varying UV exposure conditions: no exposure, and exposures of 1, 10, and 15 minutes

As can be seen, in the absence of UV exposure, both moduli remained constant over a 15-minute interval, indicating Newtonian behavior, as previously reported by other studies. In a separate test, UV exposure was applied for 1 minute starting at the beginning of the measurement. The gel point, defined by the crossover of G′ and G″, occurred at approximately 1 minute. After the UV source was turned off, G′ continued to increase for about 5 additional minutes, while G″ remained relatively stable. This post-irradiation increase in G′ is attributed to dark curing, where residual photogenerated radicals continue

to propagate crosslinking reactions, leading to further microstructural development (Bonino et al., 2011; Higham et al., 2014).

For samples exposed to UV light for 10 minutes, the storage modulus reached a plateau shortly after the light was turned off, indicating completion of the curing process. Under continuous UV exposure beyond 10 minutes, a slightly higher final G′ value was observed, suggesting a marginal increase in crosslink density. For the 10 minutes and 15 minutes UV light exposition, G’ sharply increased in the first 4 minutes, and after that its increase rate is reduced. This probably happened due to the significant decrease in PulMA chain mobility (Higham et al., 2014). Based on these results, the 15-minute UV light exposure was chosen to prepare the hydrogels in this study.

To evaluate the influence of PulMA substitution degree on hydrogel formulation, three degrees of methacrylation, 0.5%, 1.5%, and 3.0%, were tested in terms of their storage (G') and loss (G") moduli under 15 minutes of UV light exposure. As shown in Figure 7.5, an increase in the degree of methacrylation led to higher G" values, indicating that methacrylation plays a significant role in enhancing the crosslinking density, as was observed in other studies. Additionally, hydrogels prepared with higher initial PulMA concentrations exhibited increased G" values, likely due to the greater availability of polymer chains in the system, which facilitates intermolecular interactions and improves the efficiency of the crosslinking reaction (Bonino et al., 2011).

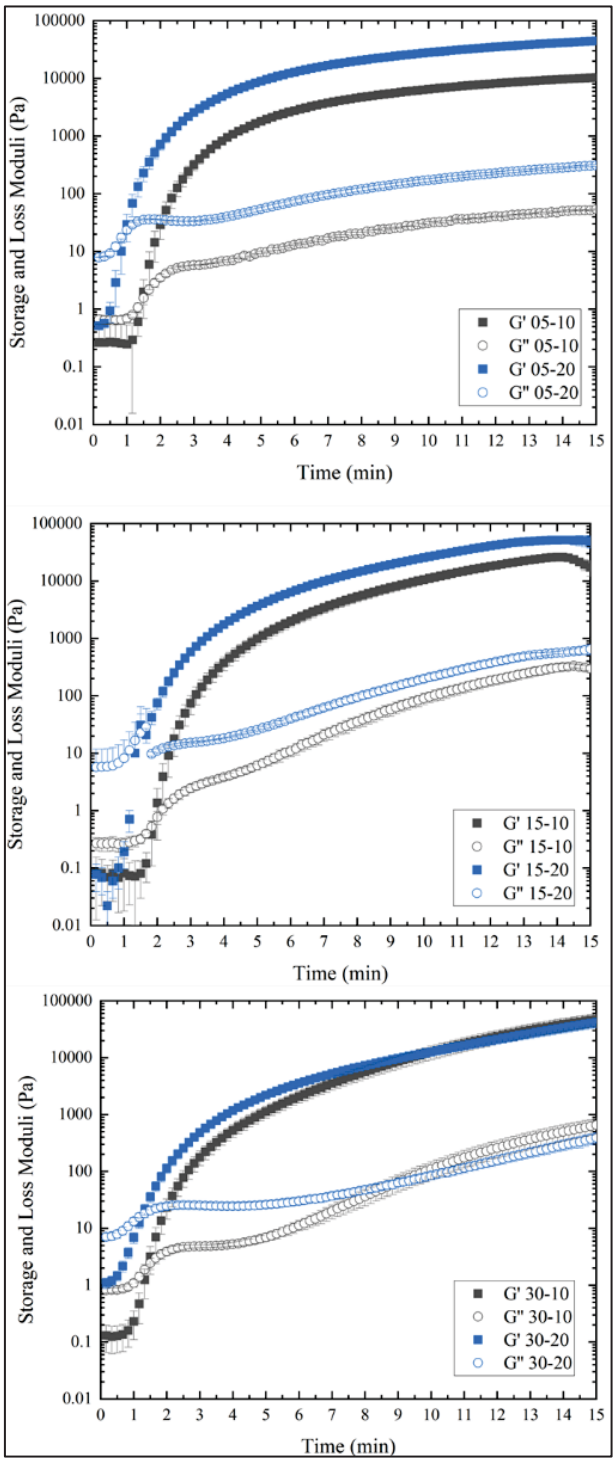

Figure 7.5 Rheological time sweep analysis of PulMA hydrogels (0.5%, 1.5%, and 3.0% MA initial concentrations) under UV light exposure for 15 minutes. Hydrogels were prepared at two initial PulMA concentrations: 10% and 20% (w/v)

The crosslink density was calculated based on the results obtained from the rheological tests and can be seen in Table 7.4 following the principles of rubber elasticity theory, which relates the elastic modulus of a polymer network to the number of elastically active chains per unit volume. According to this theory, a higher storage modulus (G') corresponds to a higher crosslink density, reflecting a more tightly connected network. As expected, increasing the degree of methacrylation led to higher crosslink densities for both solution concentrations. For hydrogels prepared with 10% (w/v) PulMA solutions at 0.5%, 1.5%, and 3.0% substitution degrees, the crosslink density increased from 4.2 to 9.9 and 16.0 mol/m³, respectively. However, for hydrogels prepared with 20% (w/v) PulMA, the differences were less pronounced, with values of 18.1, 22.4, and 21.0 mol/m³, respectively. This suggests that the polymer concentration had a stronger influence on the crosslinking efficiency than the methacrylation degree, possibly by increasing the likelihood of interactions between reactive sites during the UV-induced polymerization process.

Table 7.4 Crosslinking density of PulMA hydrogels based on their storage modulus values for PulMA 0.5%, 1.5%, and 3.0%. Hydrogels were prepared at two initial PulMA concentrations: 10% and 20% (w/v)

Hydrogel	Crosslink density (mol/m^3)	dev
PulMA05-10%	4.2	0.1
PulMA05-20%	18.1	0.5
PulMA15-10%	9.9	0.6
PulMA15-20%	22.4	1.1
PulMA30-10%	16.0	2.1
PulMA30-20%	21.0	2.5

The hydrogels crosslink density values were plotted as a function of the number of methacrylate groups available in the PulMA solution before UV crosslinking, as can be seen in Figure 7.6. The number of methacrylate groups was estimated by multiplying the substitution degree by the weight of PulMA used to prepare the solution and dividing by the molar mass of a glucose unit in pullulan. As shown in the plot, the samples PulMA05-10, PulMA15-10, PulMA30-10, and PulMA30-20 follow a clear logarithmic trend.

However, the other two data points deviate from this trend, suggesting that additional factors may have influenced the crosslinking efficiency in those formulations.

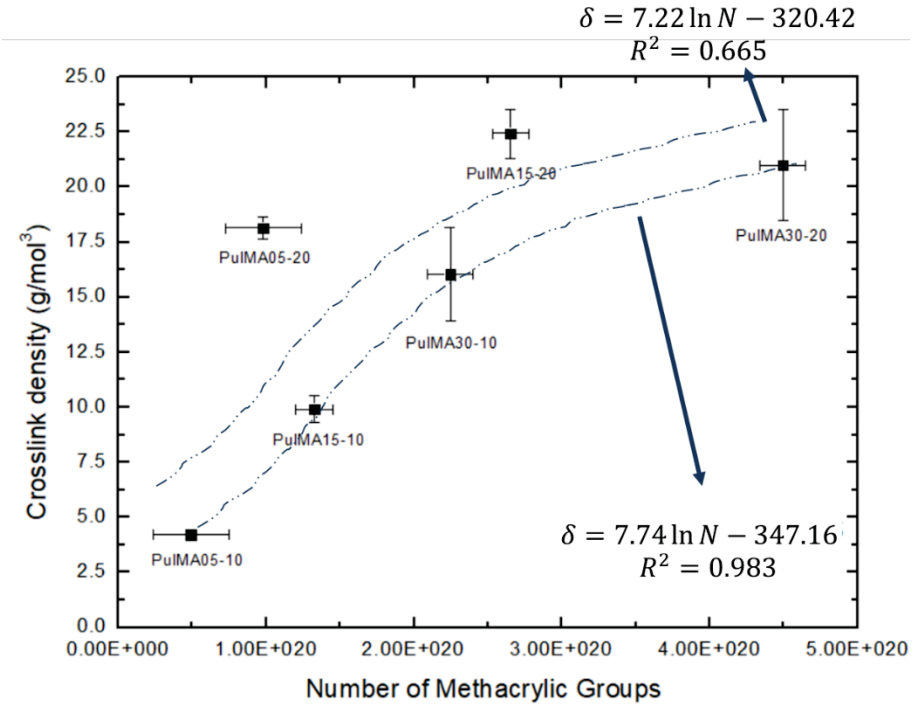

Figure 7.6 Crosslink density as a function of the number of MA groups available in the PulMA solutions

To characterize the hydrogels, swelling tests were conducted for all substitution degrees at both initial PulMA concentrations. Figure 7.7 presents the swelling capacity of the hydrogels after immersion in a pH 7.4 buffer solution for over 24 hours. The swelling capacity, expressed as a percentage, reflects the material's ability to absorb water and expand (O. Jeon et al., 2009). As expected from the crosslink density results, an inverse relationship was observed: higher crosslink density resulted in lower swelling capacity. This is likely due to the increased number of covalent bonds between polymer chains, which restricts their mobility and limits water uptake (Bae et al., 2011; I. Y. Jeon & Baek, 2010). Consequently, the PulMA hydrogel with the lowest methacrylation degree (0.5%) prepared at 10% (w/v) exhibited the highest swelling capacity, exceeding 400%. In contrast,

the PulMA hydrogel with the highest methacrylation degree (3.0%) at 20% (w/v) showed the lowest swelling, slightly above 200%, which is approximately half the value of the former.

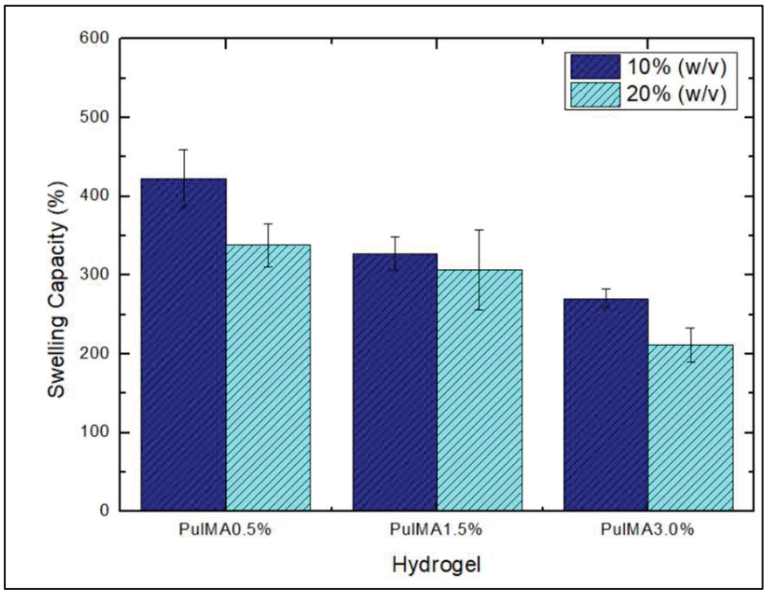

Figure 7.7 Swelling behavior of PulMA hydrogels with substitution degrees of 0.5%, 1.5%, and 3.0%, prepared at 10% and 20% (w/v) concentrations. Swelling was determined by measuring the weight difference between dry and swollen hydrogels after immersion in pH 7.4 buffer solution for 24 hours

The swelling capacity of the hydrogels was also plotted as a function of their crosslink density, as shown in

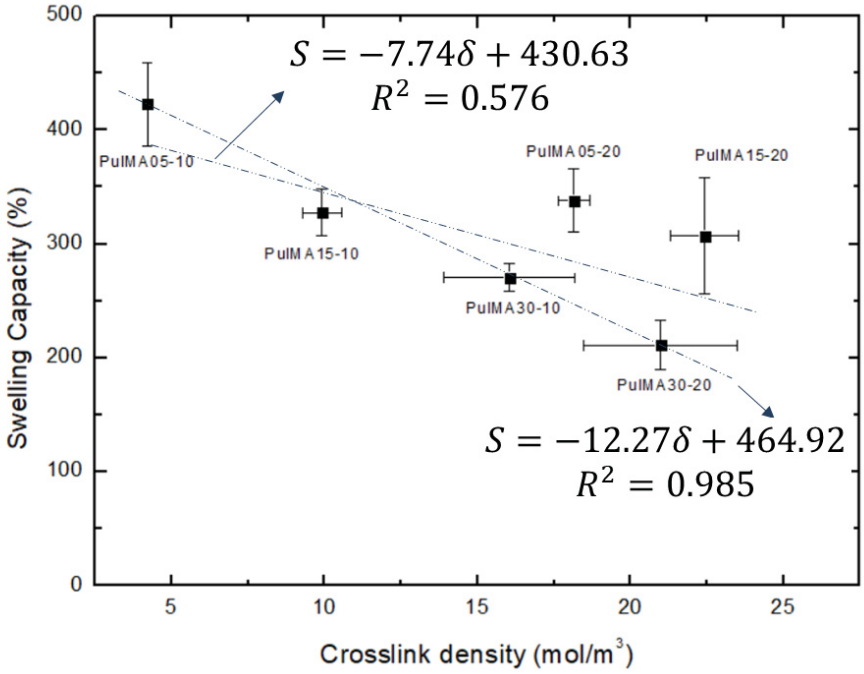

Figure 7.8. Consistent with the results observed in Figure 7.6, all samples followed the expected trend except for PulMA05-20 and PulMA15-20, which deviated from the trendline. The results confirm an inverse relationship between crosslink density and swelling capacity: as the crosslink density increases, the swelling capacity decreases, as previously observed. For the two hydrogels that did not follow this linear trend, it is likely that factors other than crosslink density, such as network defects or incomplete crosslinking, for example, may be influencing their swelling behavior.

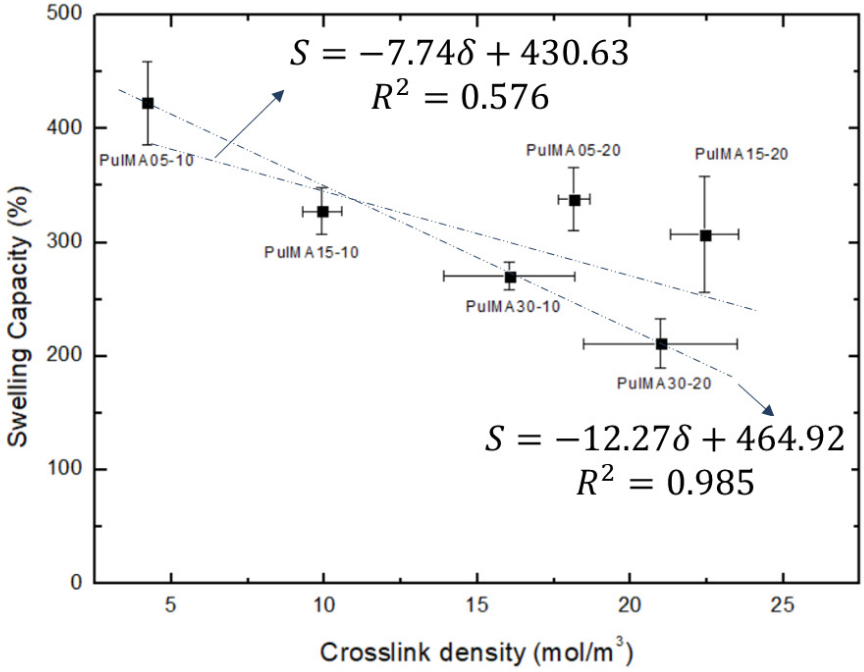

Figure 7.8 Correlation between PulMA hydrogels' swelling capacity (%) and crosslink density (mol/m^3)

To assess the influence of isoniazid (INH) concentration on the crosslinking density of hydrogels, a time sweep rheological test was conducted using PulMA 0.5% hydrogels prepared at 20% (w/v), both with and without INH. INH was incorporated at concentrations of 1%, 3%, and 5% (w/w, relative to PulMA), as can be seen in Figure 7.9. As observed, at 5% INH, the gel point was delayed, shifting from 1 minute (in the INH-free hydrogel) to approximately 2 minutes, suggesting that the presence of INH interferes with the crosslinking reaction. This effect is likely due to intermolecular interactions between INH and PulMA chains, particularly hydrogen bonding, which may hinder the mobility and proximity of reactive groups required for effective crosslinking. At lower INH concentrations, especially 1%, these interactions appeared less significant, allowing the storage modulus to reach values similar to those of the INH-free PulMA hydrogel, indicating a more efficient crosslinking process.

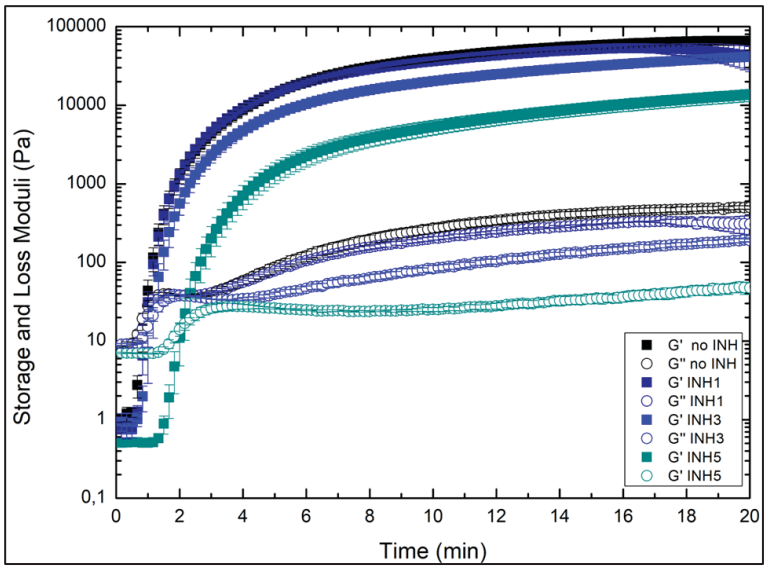

Figure 7.9 Rheological time sweep analysis of PulMA 0.5% hydrogels prepared at 20% (w/v), exposed to UV light for 15 minutes. Hydrogels were formulated with and without isoniazid (INH), using three different INH concentrations: 1%, 3%, and 5% (w/w)

Based on the results of the swelling test and the observed influence of isoniazid (INH) on the crosslinking density of PulMA hydrogels, drug release studies were conducted in pH 7.4 buffer solution for 8 hours (480 minutes) at 37 °C. Three systems were evaluated: PulMA 0.5% hydrogels (prepared at 20% w/v) containing 1% and 5% INH (w/w), and PulMA 3.0% hydrogels containing 1% INH. Figure 7.10 shows the cumulative release (%) of INH over time. For PulMA 0.5%, both INH-loaded hydrogels exhibited similar release profiles, with nearly complete drug release occurring within approximately 2 hours. In contrast, the PulMA 3.0% hydrogel showed a slight improvement in sustained release, extending to around 3 hours; however, the release was incomplete, with approximately 30% of the drug remaining unreleased by the end of the test. Although these systems did not demonstrate prolonged sustained release, the results highlight the potential of PulMA hydrogels for drug delivery applications. Future modifications, such as incorporating polymeric blends, developing PulMA/clay nanocomposites, or adding PEGDA, could be explored to further control the release rate and enhance the applicability of these systems.

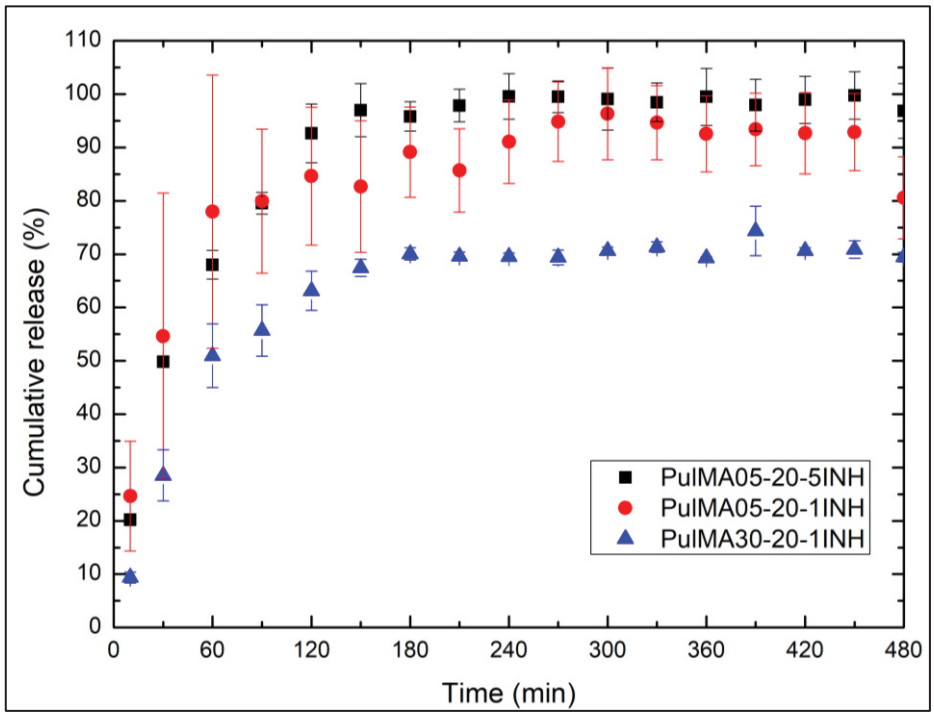

Figure 7.10 Cumulative release (%) of isoniazid (INH) from PulMA hydrogels prepared at 20% (w/v) polymer concentration, over 8 hours in pH 7.4 buffer solution at 37 °C. PulMA 0.5% hydrogels were formulated with 1% and 5% (w/w) INH, while PulMA 3.0% was tested with 1% (w/w) INH

To better understand the release mechanisms, the experimental data were fitted to three kinetic models: Zero-order, Higuchi, and Korsmeyer–Peppas (Table 7.5). As recommended, the Korsmeyer–Peppas model was applied only to the initial 70% of drug release. Among the models tested, it generally provided the best fit to the experimental data. As discussed in Section 1.1.1, the parameters of this model offer insight into the underlying release mechanisms. For all hydrogels, the n-values were approximately 0.6, indicating that anomalous (non-Fickian) diffusion played a significant role in the release behavior. This suggests that both swelling and drug diffusion contributed to the drug release process. The other constant parameter, “K”, decreased as the crosslinking degree density increased, indicating a decrease in the release rate.

Table 7.5 fitting parameters of PulMA hydrogels in three different models: Zero-order, Higuchi, and Korsmeyer-Peppas

Models	Parameters	PulMA05-20-1INH	PulMA05-20-5INH	PulMA30-20-IINH
Zero-order	K_0	0.146	0.294	0.210
	R^2	0.423	0.500	0.516
Higuchi	K_h	5.308	5.696	87.000
	R^2	0.999	0.691	0.704
Korsmeyer-Peppas	K	6.606	5.741	3.729
	n	0.606	0.610	0.601
	R^2	0.991	0.975	0.955

7.3 Conclusion

The results presented in this section demonstrate the significant influence of formulation parameters on the properties and performance of PulMA-based hydrogels. The degree of methacrylation was directly affected by the initial amount of methacrylic anhydride (MA), which in turn influenced the crosslinking behavior and mechanical properties of the resulting hydrogels.

Rheological analyses showed that PulMA solutions exhibited good stability in the absence of UV exposure. Upon UV irradiation, the crosslinking process was initiated, with the storage modulus (G') increasing over time. However, a plateau was reached after approximately 10 minutes, indicating that prolonged UV exposure beyond this point does not significantly enhance the crosslinking density.

Both the concentration of the PulMA solution and the degree of substitution were found to affect the final hydrogel properties. Higher PulMA concentrations led to greater crosslinking densities and consequently lower swelling capacities due to the denser polymeric network. Conversely, the incorporation of isoniazid (INH), especially at higher concentrations, interfered with the crosslinking process, likely through intermolecular interactions that hindered the formation of covalent bonds.

Despite this, hydrogels with higher crosslinking densities demonstrated improved sustained release profiles, emphasizing the importance of network structure in controlling drug delivery behavior. These findings confirm the potential of PulMA hydrogels for drug delivery applications and provide valuable insights for further optimization through compositional adjustments or incorporation of additional components.

In future works, the influence of UV intensity and the gel point determination by the Winter-Chambon criteria should be studied.

CONCLUSION

This thesis presents a comprehensive investigation into the development of clay-based and hydrogel-based systems for the controlled release of isoniazid (INH), a frontline antituberculosis drug. Through a multidisciplinary approach combining materials characterization, adsorption and release studies, and formulation optimization, the work highlights the potential of smectite clays and pullulan-derived hydrogels as effective carriers for oral drug delivery applications.

Smectite clays of natural and synthetic origins were systematically evaluated to determine their adsorption capacities, retention efficiencies, and release behaviors. The findings revealed that INH adsorption is highly dependent on the clay's physicochemical properties, particularly pore volume and surface interactions. An optimal pore volume of ~0.100 cm^3/g was identified for maximum INH uptake. XRD analyses confirmed that INH adsorption occurred primarily on external surfaces and inter-tactoid pores rather than through intercalation.

Among the tested clays, a Brazilian natural clay (VVd) demonstrated the highest adsorption capacity (~115 mg/g at pH 2) and favorable release profiles. Mechanistic investigations under different pH conditions elucidated the role of INH speciation and electrostatic interactions: at acidic pH, INH is protonated and adsorbs via electrostatic attraction, favoring strong monolayer binding and minimal drug release in gastric conditions (~8%). At neutral pH, adsorption involved both monolayer and multilayer mechanisms, with multilayer incorporation contributing to higher drug loading but increased burst release. These results underscore the delicate balance between drug loading and release control, dictated by the nature of drug–clay interactions.

Spectroscopic and thermal analyses (FTIR, TGA, DSC) confirmed that INH binds to clay surfaces through its hydrazine, pyridine, and carbonyl groups, establishing stable interactions that enhance thermal protection. The zero-order release kinetics observed in select formulations at intestinal pH further demonstrate the system’s promise for sustained drug delivery.

The study also explored the impact of clay chemical composition by comparing materials with similar morphology but distinct surface charges. Cloisite (CL), for instance, showed

superior performance to Laponite (LP) in both adsorption and release, likely due to its lower surface charge, which enhanced drug retention through stronger interactions.

In parallel, the potential of modified pullulan (PulMA) hydrogels was assessed. The degree of methacrylation was shown to regulate crosslinking density, rheological properties, and swelling behavior. UV exposure induced gelation, with a plateau in mechanical strength reached after 10 minutes. Drug incorporation affected hydrogel structure—higher INH concentrations interfered with network formation, decreasing crosslinking efficiency. However, when optimized, higher-density PulMA hydrogels achieved a more sustained release, demonstrating that network design is crucial for effective drug delivery.

Taken together, the results of this thesis establish a solid foundation for the rational design of drug delivery systems using smectite clays and PulMA hydrogels. VVd and CL clays, in particular, offer a biocompatible, cost-effective, and scalable platform for INH delivery. The adsorption process, based on room-temperature aqueous dispersion, further supports industrial translation. Importantly, cytotoxicity assays confirmed the safety of the natural clay, making it an appealing candidate for pharmaceutical applications.

Nonetheless, limitations remain, including potential aggregation effects under physiological conditions and the need for further in vivo validation. Future research should include advanced biological assessments, as well as molecular modeling to elucidate interaction mechanisms in greater detail. These insights will pave the way for the development of next-generation delivery platforms tailored for drugs requiring protection in acidic environments and controlled release in the intestine, such as those used in tuberculosis treatment.

RECOMMENDATION

- Clays
    - Evaluate the release of exchangeable cations from clays and their potential cytotoxic or stimulatory effects on human cells.
    - Investigate the potential agglomeration of clays under physiological conditions and assess its implications for biomedical applications, particularly in terms of bioavailability and safety.
- Pullulan
    - Study the influence of UV intensity in obtaining PulMA hydrogels.
    - Determine PulMA hydrogels' gel point by the Winter-Chambon criteria.
    - Incorporate PEGDA (polyethylene glycol diacrylate) into PulMA hydrogels to enhance mechanical properties and improve sustained drug release profiles.
    - Develop PulMA/clay composite hydrogels and investigate the effect of clay concentration on INH release kinetics and overall system performance.
    - Explore the application of PulMA hydrogels in other biomedical fields, such as tissue engineering, cell proliferation scaffolds, topical drug delivery, and ocular controlled release systems.
- Clays and Pullulan
    - Future studies should incorporate lung-relevant cell models to further evaluate the material’s effects in a more disease-specific context for cytotoxicity tests.

Conduct in vivo studies to validate the efficacy and safety of clay-based systems for isoniazid (INH) delivery.

APPENDIX

VITA

EDUCATION

- Ph.D. in Mechanical/Materials Engineering (2025) – École de Technologie Supérieure (Canada) / Universidade de São Paulo (Brazil)
- Master's in Materials Engineering (2019) – Universidade de São Paulo (Brazil)
- Bachelor's in Materials Engineering (2016) – Universidade de São Paulo (Brazil)

AWARDS AND SCHOLARSHIPS

- 2025 – ÉTS Financial support for the dissemination and promotion of research work, Travel Grant (1,000) to support attendance at the European Polymer Congress.
- 2025 – ETS Move on Scholarship Travel Grant (1,000) to support attendance at the European Polymer Congress.
- 2025 – SPE Travel Grant (1,000 CAD) to support attendance at the European Polymer Congress.
- 2025 – AIPEA Travel Grant (500 €), awarded by the Association Internationale pour l'Étude des Argiles through a competitive selection process to support attendance at the International Clay Conference 2025 (Dublin, Ireland).
- 2025 – Blair Jones / Jane Flynn Award (500 USD), granted by The Clay Minerals Society to the highest-rated travel grant application for the International Clay Conference 2025 (Dublin, Ireland).
- 2025 – Travel Grant from The Clay Minerals Society (1,250 USD), awarded through a competitive process with a record number of applicants, to attend the International Clay Conference 2025 (Dublin, Ireland).

- 2025 – Second-Best Poster Presentation Award, Colloque étudiant du CREPEC (Centre de recherche sur les systèmes polymères et composites à haute performance), Université de Montréal, Montréal. University-level competition.
- 2025 – Second-Best Oral Presentation Award, Journée scientifique ITechSanté, ÉTS, Montréal. University-level competition. Recipient of a 1,000 CAD prize.
- 2025 – First Place, “My Thesis in 3 Minutes” competition, Congrès annuel des étudiants chercheurs de l’ÉTS (CAÉC), Montréal. University-level competition. Recipient of a 100 CAD prize.
- 2023 – Second Place, “My Plastics in 3 Minutes” competition, Society of Plastics Engineers (SPE), Quebec. Recipient of a 300 CAD prize.
- 2022 – Best Presentation Award, “My Thesis in 3 Minutes,” PolymerÉTS Group, ÉTS, Montréal.
- 2022-2023 - Coordination for the Improvement of Higher Education Personnel (CAPES), Brazil.
- 2020–2023 – Ph.D. Fellowship, National Council for Scientific and Technological Development (CNPq), Brazil.
- 2017–2019 – Master’s Fellowship, Coordination for the Improvement of Higher Education Personnel (CAPES), Brazil.
- 2014-2015: Undergraduate Research Fellowship (Brazil) – USP-PIBIC.

JOURNAL PUBLICATION

1. de Carvalho Arjona, J.; Samara, M.; Ulsen, C.; Valenzuela Diaz, F.R.; Demarquette, N.R. Isoniazid Adsorption and Release by Cloisite and Laponite: An Effect of Surface Charge. Mater Chem Phys 2025, 344, doi:10.1016/j.matchemphys.2025.131097.

2. de Carvalho Arjona, J.; Ulsen, C.; Tada, D.; Valenzuela Diaz, F.R.; Demarquette, N.R. The Influence of Adsorption Incorporation Mechanism on the Release of Isoniazid by Montmorillonite. J Drug Deliv Sci Technol 2025, 106809, doi:https://doi.org/10.1016/j.jddst.2025.106809.

3. de Carvalho Arjona, J.; Ulsen, C.; Valenzuela-Diaz, F.R.; Demarquette, N.R. Influence of Smectite Clays' Pores Volume on Isoniazid Adsorption and Release. Appl Clay Sci 2024, 252, doi:10.1016/j.clay.2024.107341.

4. Pinheiro, G. de O.; Batista, J.; Carvalho, T.; Arjona, J.; Nascimento, V.S. de O.; Gaviria, M.; Valenzuela-Diaz, F.R. Incorporation of Isoniazid in Clay Minerals : A Study Review. Brazilian Journal of Health Review 2022, 5, 4493–4510, doi:10.34119/bjhrv5n2-049.

5. Arjona, J. de C.; Silva-Valenzuela, M.D.G.; Wang, S.H.; Valenzuela-Diaz, F.R. Biodegradable Nanocomposite Microcapsules for Controlled Release of Urea. Polymers (Basel) 2021, 13, 1–12, doi:10.3390/polym13050722.

6. Pinheiro Gilmar and Carvalho, T. and M.B. and A.J. and B.M. and S.-V.M. and C.T. and V.-D.F. Characterization of a Brazilian Kaolin and Its Sorption Ability to Mineral Oils. In Proceedings of the Characterization of Minerals, Metals, and Materials 2020; Li Jian and Zhang, M. and L.B. and M.S.N. and I.S. and K.Y.E. and H.J.-Y. and E.-D.J.P. and C.J.S. and B.A.D., Ed.; Springer International Publishing: Cham, 2020; pp. 367–373.

7. Arjona, J.C.; Valenzuela-Díaz, F.R.; Wiebeck, H.; Hui, W.S.; Silva-Valenzuela, M.G. Physical Properties of PHB/VMF2 Nanocomposite Microcapsules in Water. Materials Science Forum 2018, 930, 190–194.

8. Arjona, J.C.; Valenzuela-Diaz, F.R.; Wiebeck, H.; Wang, S.H.; Silva-Valenzuela, M.G. Evaluation of Urea Encapsulation by Microcapsules of PHB/MMT and PHB/OMMT Nanocomposites. In Minerals, Metals, and Materials 2018. Minerals, Metals and Materials Series.; Springer International Publishing: Cham, 2018; pp. 365–372 ISBN 9783319724836.

CONFERENCE PRESENTATIONS

2025 – XVIII International Clay Conference (ICC). Oral presentation: “The Influence of Clay Pore Volume and Surface Charge on Isoniazid Adsorption and Release”.

2025 – European Polymer Congress (EPF). Oral presentation: “Pullulan Hydrogels as Drug Release Vehicle for Tuberculosis Treatment”.

2025 – CREPEC Student Colloquium (Centre for Research on High-Performance Polymer and Composite Systems), Université de Montréal. Poster presentation: “A Promising Hydrogel for Tomorrow’s Biomedical Solutions.”

2018 – The Minerals, Metals & Materials Society (TMS) Conference. Oral presentation: “Evaluation of Urea Encapsulation by Microcapsules of PHB/MMT and PHB/OMMT Nanocomposites.”

2016 – Brazilian Congress on Materials Engineering and Science (CBECIMAT). Poster presentation: “Physical Properties of PHB/VMF2 Nanocomposite Microcapsules in Water.”

2015 – USP International Symposium on Scientific Initiation (SIICUSP). Poster presentation: “Production of Microcapsules from PHB Composites Reinforced with Brazilian Clay.”

APPENDIX I

FTIR SPECTRA OF PULMA 2ND AND 3RD BATCHES

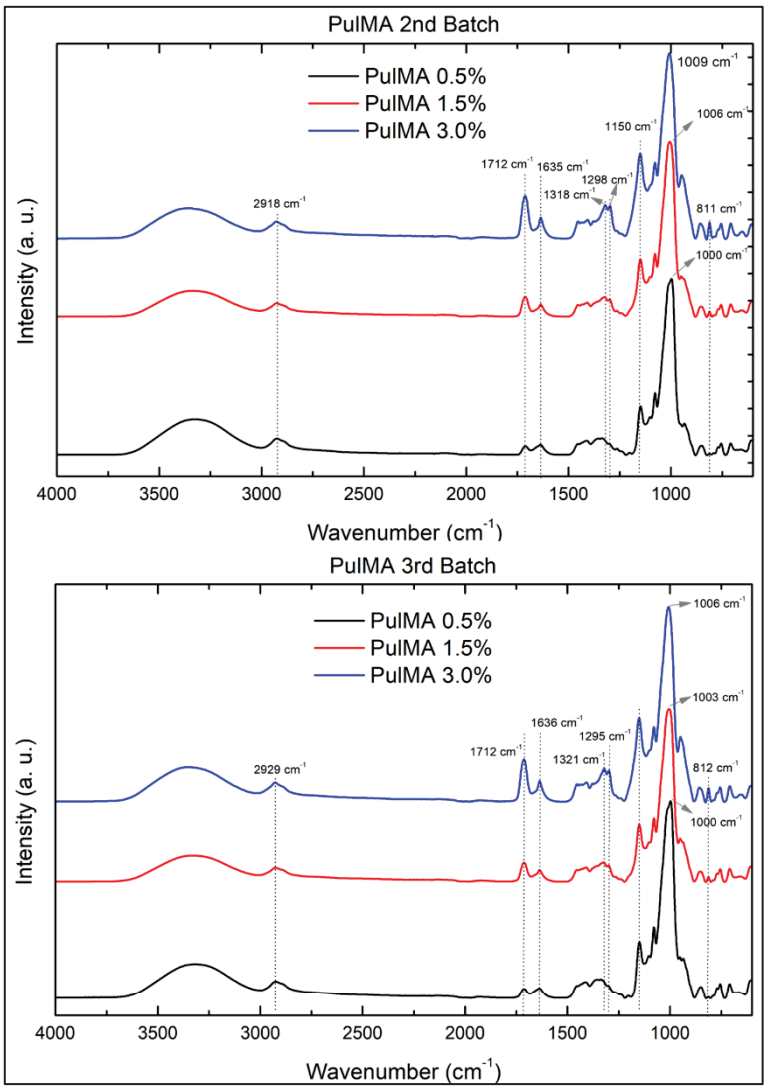

Figure A - I - 1 FTIR spectra of the second and third batches of PulMA 0.5%, 1.5%, and 3.0%

APPENDIX II

^{1}H-NMR SPECTRA OF PULMA 2ND AND 3RD BATCH

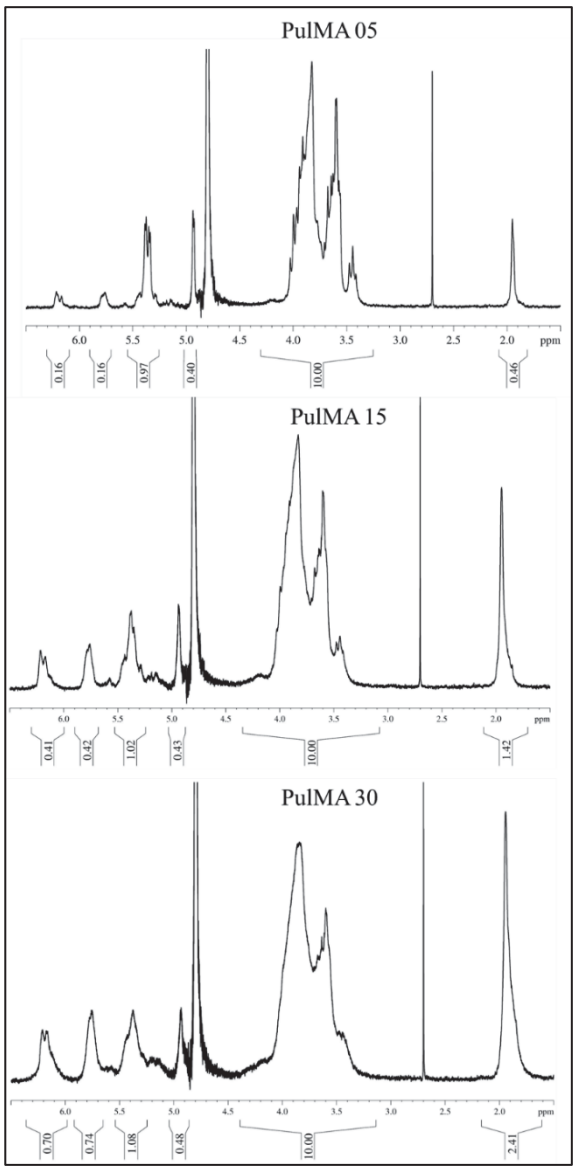

Figure A - II - 1 ^{1}H-NMR spectra of PulMA 0.5%, 1.5%, and 3.0% 2nd batch

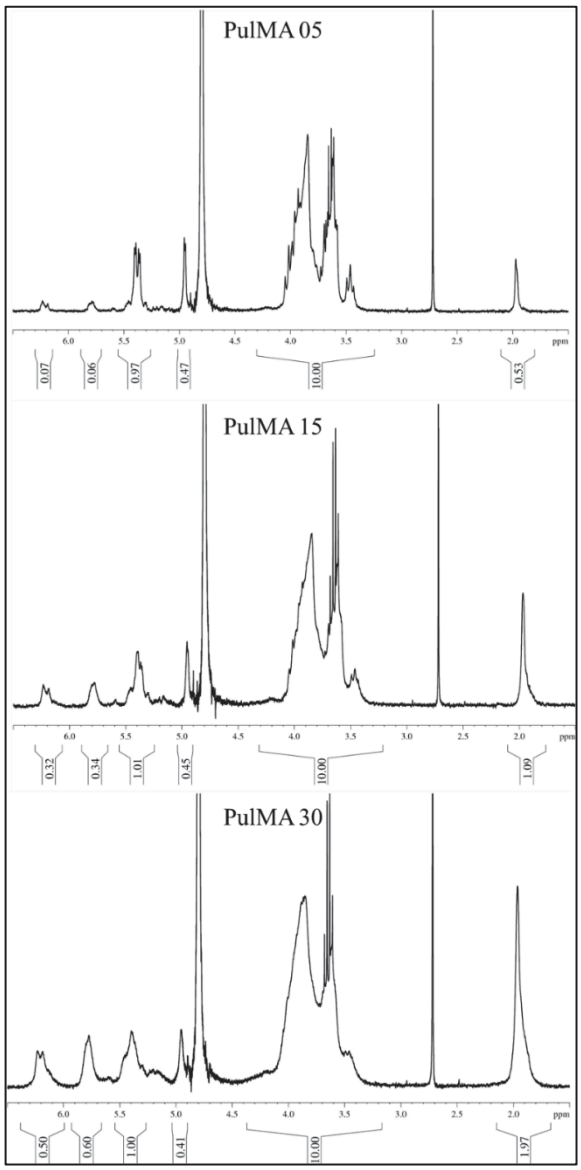

Figure A - II - 2 H-NMR spectra of PulMA 0.5%, 1.5%, and 3.0% 3rd batch

LIST OF REFERENCES

Adoungotchodo, A., Epure, L. M., Mwale, F. & Lerouge, S. (2021). Chitosan-based hydrogels supplemented with gelatine and link n enhance extracellular matrix deposition by encapsulated cells in a degenerative intervertebral disc environment. *European Cells and Materials*, *41*, 471-484. https://doi.org/10.22203/eCM.v041a30

Aguzzi, C., Cerezo, P., Viseras, C. & Caramella, C. (2007). Use of clays as drug delivery systems: Possibilities and limitations. *Applied Clay Science*, *36*, 22-36. https://doi.org/10.1016/j.clay.2006.06.015

Ahmed, L., Atif, R., Salah Eldeen, T., Yahya, I., Omara, A. & Eltayeb, M. (2019). Study the Using of Nanoparticles as Drug Delivery System Based on Mathematical Models for Controlled Release. *International Journal of Latest Technology in Engineering*, *VIII*(V), 52-56. www.ijltemas.in

Akyuz, S. & Akyuz, T. (2008). FT-IR and FT-Raman spectroscopic studies of adsorption of isoniazid by montmorillonite and saponite. *Vibrational Spectroscopy*, *48*(2), 229-232. https://doi.org/10.1016/j.vibspec.2008.02.019

Akyuz, S., Akyuz, T. & Akalin, E. (2010). Adsorption of isoniazid onto sepiolite-palygorskite group of clays: An IR study. *Spectrochimica Acta - Part A: Molecular and Biomolecular Spectroscopy*, *75*(4), 1304-1307. https://doi.org/10.1016/j.saa.2009.12.069

Alabarse, F. G., Conceição, R. V., Balzaretti, N. M., Schenato, F. & Xavier, A. M. (2011). In-situ FTIR analyses of bentonite under high-pressure. *Applied Clay Science*, *51*(1-2), 202-208. https://doi.org/10.1016/j.clay.2010.11.017

Almeida, J. M. F. de, Damasceno Júnior, E., Verrísimo, L. M. & Fernandes, N. S. (2019). pH-Dependent release system of isoniazid carried on nanoparticles of silica obtained from expanded perlite. *Applied Surface Science*, *489*, 297-312. https://doi.org/10.1016/j.apsusc.2019.05.317

Altamimi, M. A., Hussain, A., Imam, S. S., Alshehri, S., Singh, S. K. & Webster, T. J. (2020). Transdermal delivery of isoniazid loaded elastic liposomes to control cutaneous and systemic tuberculosis. *Journal of Drug Delivery Science and Technology*, *59*, 101848. https://doi.org/10.1016/j.jddst.2020.101848

Alves, A. D., Cavaco, J. S., Guerreiro, F., Lourenço, J. P., Rosa Da Costa, A. M. & Grenha, A. (2016). Inhalable antitubercular therapy mediated by locust bean gum microparticles. *Molecules*, *21*(6), 1-22. https://doi.org/10.3390/molecules21060702

Angadi, S. C., Manjeshwar, L. S. & Aminabhavi, T. M. (2010). Interpenetrating polymer network blend microspheres of chitosan and hydroxyethyl cellulose for controlled release of isoniazid. *International Journal of Biological Macromolecules*, *47*(2), 171-179. https://doi.org/10.1016/j.ijbiomac.2010.05.003

Anisimova, Y. V, Gelperina, S. I., Peloquin, C. A. & Heifets, L. B. (2000). Nanoparticles as antituberculosis drugs carriers: effect on activity against Mycobacterium tuberculosis in human monocyte-derived macrophages. *Journal of Nanoparticle Research*, *2*, 165-171.

Badr, S., Madadian, E., MacDonald, D., Tasker, R. A. & Ahmadi, A. (2023). A mist-based crosslinking technique for coaxial bioprinting of hollow hydrogel fibers. *Bioprinting*, *35*. https://doi.org/10.1016/j.bprint.2023.e00308

Bae, H., Ahari, A. F., Shin, H., Nichol, J. W., Hutson, C. B., Masaeli, M., Kim, S. H., Aubin, H., Yamanlar, S. & Khademhosseini, A. (2011). Cell-laden microengineered pullulan methacrylate hydrogels promote cell proliferation and 3D cluster formation. *Soft Matter*, *7*(5), 1903-1911. https://doi.org/10.1039/c0sm00697a

Banik, N., Hussain, A., Ramteke, A., Sharma, H. K. & Maji, T. K. (2012). Preparation and evaluation of the effect of particle size on the properties of chitosan-montmorillonite nanoparticles loaded with isoniazid. *RSC Advances*, *2*(28), 10519-10528. https://doi.org/10.1039/c2ra20702h

Banik, N., Ramteke, A. & Maji, T. K. (2014). Carboxymethyl chitosan-montmorillonite nanoparticles for controlled delivery of isoniazid: evaluation of the effect of the glutaraldehyde and montmorillonite. *Polymers for Advanced Technologies*, *25*(12), 1580-1589. https://doi.org/10.1002/pat.3406

Batalha, I. L., Bernut, A., Schiebler, M., Ouberai, M. M., Passemar, C., Klapholz, C., Kinna, S., Michel, S., Sader, K., Castro-hartmann, P., Renshaw, S. A., Welland, M. E. & Floto, R. A. (2019). Polymeric nanobiotics as a novel treatment for mycobacterial infections. *Journal of Controlled Release*, *314*, 116-124. https://doi.org/10.1016/j.jconrel.2019.10.009

Bekaroğlu, M. G., Nurili, F. & İşçi, S. (2018). Montmorillonite as imaging and drug delivery agent for cancer therapy. *Applied Clay Science*, *162*, 469-477. https://doi.org/10.1016/j.clay.2018.06.039

Bera, H., Ang, S. R., Chiong, S. W., Chan, C. H., Abbasi, Y. F., Law, L. P., Chatterjee, B. & Venugopal, V. (2020). Core-shell structured pullulan based nanocomposites as erlotinib delivery shuttles. *International Journal of Polymeric Materials and Polymeric Biomaterials*, *69*(13), 848-859. https://doi.org/10.1080/00914037.2019.1626389

Bergaya, F, Theng, B. & Lagaly, G. (2005). Handbook of Clay Science. Dans Elsevier (Éd.), *Handbook of Clay Science* (4th éd.). Elsevier.

Bhandari, R. & Kaur, I. P. (2012). A Sensitive HPLC Method for Determination of Isoniazid in Rat Plasma, Brain, Liver and Kidney. *Journal of Chromatography & Separation Techniques*, *03*(03). https://doi.org/10.4172/2157-7064.1000128

Bhardwaj, A., Mehta, S., Yadav, S., Singh, S. K., Grobler, A., Goyal, A. K. & Mehta, A. (2016a). Pulmonary delivery of antitubercular drugs using spray-dried lipid–polymer hybrid nanoparticles. *Artificial Cells, Nanomedicine and Biotechnology*, *44*(6), 1544-1555. https://doi.org/10.3109/21691401.2015.1062389

Bhardwaj, A., Mehta, S., Yadav, S., Singh, S. K., Grobler, A., Goyal, A. K. & Mehta, A. (2016b). Pulmonary delivery of antitubercular drugs using spray-dried lipid–polymer hybrid nanoparticles. *Artificial Cells, Nanomedicine and Biotechnology*, *44*(6), 1544-1555. https://doi.org/10.3109/21691401.2015.1062389

Bhat, A. H., Rangreez, T. A., Inamuddin & Chisti, H.-T.-N. (2020). Wastewater Treatment and Biomedical Applications of Montmorillonite Based Nanocomposites: A Review. *Current Analytical Chemistry*, *18*(3), 269-287. https://doi.org/10.2174/1573411016999200729123309

Bonino, C. A., Samorezov, J. E., Jeon, O., Alsberg, E. & Khan, S. A. (2011). Real-time in situ rheology of alginate hydrogel photocrosslinking. *Soft Matter*, *7*(24), 11510-11517. https://doi.org/10.1039/c1sm06109g

Borrego-Sánchez, A. & Sainz-Díaz, C. I. (2021). Clay minerals as filters of drug compounds for green chemistry applications. Dans *Green Chemistry and Computational Chemistry: Shared Lessons in Sustainability* (p. 403-423). Elsevier. https://doi.org/10.1016/B978-0-12-819879-7.00012-X

Bostanudin, M. F., Barbu, E. & Liew, K. Bin. (2021). Hydrophobically grafted pullulan nanocarriers for percutaneous delivery: Preparation and preliminary in vitro characterisation. *Polymers*, *13*(17). https://doi.org/10.3390/polym13172852

Brasil. Ministério da Saúde. (2025). *TUBERCULOSE 2025: Boletim Epidemiológico*.

Brigatti, M. F., Galan, E. & Theng, B. K. G. (2006). Chapter 2 Structures and Mineralogy of Clay Minerals. Dans Faïza Bergaya, B. K. G. Theng & G. Lagaly (Éd.), *Handbook of Clay Science* (Vol. 1, p. 19-86). Elsevier. https://doi.org/https://doi.org/10.1016/S1572-4352(05)01002-0

Bromberg, L., Straut, C. M., Centrone, A., Wilusz, E. & Hatton, T. A. (2011). Montmorillonite functionalized with pralidoxime as a material for chemical protection against organophosphorous compounds. *ACS Applied Materials and Interfaces*, *3*(5), 1479-1484. https://doi.org/10.1021/am200041e

BYK Additives & Instruments. (2014). Laponite: performance additives. Dans *Technical information B-RI 21*.

Calabrese, I., Cavallaro, G., Scialabba, C., Licciardi, M., Merli, M., Sciascia, L. & Turco Liveri, M. L. (2013). Montmorillonite nanodevices for the colon metronidazole delivery. *International Journal of Pharmaceutics*, *457*(1), 224-236. https://doi.org/10.1016/j.ijpharm.2013.09.017

Calabrese, I., Gelardi, G., Merli, M., Liveri, M. L. T. & Sciascia, L. (2017). Clay-biosurfactant materials as functional drug delivery systems: Slowing down effect in the in vitro release of cinnamic acid. *Applied Clay Science*, *135*, 567-574. https://doi.org/10.1016/j.clay.2016.10.039

Caliceti, P., Salmaso, S., Lante, A., Yoshida, M., Katakai, R., Martellini, F., Mei, L. H. I. & Carenza, M. (2001). Controlled release of biomolecules from temperature-sensitive hydrogels prepared by radiation polymerization. *Journal of Controlled Release*, *75*, 173-181.

Çalışkan Salihi, E., Gündüz, Z., Baştuğ, A. S., Salihi, E. Ç., Gündüz, Z. & Baştuğ, A. S. (2019). Fast retention of isoniazid on organobentonite prepared using green chemistry approach: contribution of the π interactions. *Separation Science and Technology (Philadelphia)*, *54*(16), 2695-2705. https://doi.org/10.1080/01496395.2018.1543324

Carazo, E., Borrego-Sánchez, A., García-Villén, F., Sánchez-Espejo, R., Aguzzi, C., Viseras, C., Sainz-Díaz, C. I. & Cerezo, P. (2017). Assessment of halloysite nanotubes as vehicles of isoniazid. *Colloids and Surfaces B: Biointerfaces*, *160*, 337-344. https://doi.org/10.1016/j.colsurfb.2017.09.036

Carazo, E., Borrego-Sánchez, A., García-Villén, F., Sánchez-Espejo, R., Viseras, C., Cerezo, P. & Aguzzi, C. (2018). Adsorption and characterization of palygorskite-isoniazid nanohybrids. *Applied Clay Science*, *160*, 180-185. https://doi.org/10.1016/j.clay.2017.12.027

Carazo, Esperanza, Borrego-Sánchez, A., Sánchez-Espejo, R., García-Villén, F., Cerezo, P., Aguzzi, C. & Viseras, C. (2018). Kinetic and thermodynamic assessment on isoniazid/montmorillonite adsorption. *Applied Clay Science*, *165*, 82-90. https://doi.org/10.1016/j.clay.2018.08.009

Carazo, Esperanza, Sandri, G., Cerezo, P., Lanni, C., Ferrari, F., Bonferoni, C., Viseras, C. & Aguzzi, C. (2019). Halloysite nanotubes as tools to improve the actual challenge of fixed doses combinations in tuberculosis treatment. *Journal of Biomedical Materials Research - Part A*, *107*(7), 1513-1521. https://doi.org/10.1002/jbm.a.36664

Carretero, M. I. (2002). Clay minerals and their beneficial effects upon human health. A review. *Applied Clay Science*, *21*, 155-163. https://doi.org/10.1016/S0140-6736(00)90347-7

Cavalcanti, G. R. S., Fonseca, M. G., da Silva Filho, E. C. & Jaber, M. (2019). Thiabendazole/bentonites hybrids as controlled release systems. *Colloids and Surfaces B: Biointerfaces*, *176*, 249-255. https://doi.org/10.1016/j.colsurfb.2018.12.030

Chang, J., Fan, X., Jiang, Z., Wang, X., Chen, L., Li, J., Zhu, L., Wan, C. & Chen, Z. (2022). Differential impact of clay minerals and organic matter on pore structure and its fractal characteristics of marine and continental shales in China. *Applied Clay Science*, *216*. https://doi.org/10.1016/j.clay.2021.106334

Chavda, H. & Patel, C. (2010). Chitosan superporous hydrogel composite-based floating drug delivery system: A newer formulation approach. *Journal of Pharmacy and Bioallied Sciences*, *2*, 124-131. https://doi.org/10.4103/0975-7406.67010

Chen, F., Yu, S., Liu, B., Ni, Y., Yu, C., Su, Y., Zhu, X., Yu, X., Zhou, Y. & Yan, D. (2016). An Injectable Enzymatically Crosslinked Carboxymethylated Pullulan/Chondroitin Sulfate Hydrogel for Cartilage Tissue Engineering. *Scientific Reports*, *6*. https://doi.org/10.1038/srep20014

Chen, G., Wu, Y., Yu, D. & Li, R. (2018). Isoniazid-loaded chitosan/carbon nanotubes microspheres promote secondary wound healing of bone tuberculosis. *Journal of Biomaterials applications*, *33*(7), 989-996. https://doi.org/10.1177/0885328218814988

Choy, J., Choi, S., Oh, J. & Park, T. (2007). Clay minerals and layered double hydroxides for novel biological applications. *Applied Clay Science*, *36*(1-3), 122-132. https://doi.org/10.1016/j.clay.2006.07.007

Constantin, M., Fundueanu, G., Bortolotti, F., Cortesi, R., Ascenzi, P. & Menegatti, E. (2007). A novel multicompartimental system based on aminated poly(vinyl alcohol) microspheres/succinoylated pullulan microspheres for oral delivery of anionic drugs. *International Journal of Pharmaceutics*, *330*(1-2), 129-137. https://doi.org/10.1016/j.ijpharm.2006.09.005

Damasceno Junior, E., Almeida, J. M. F. de, Silva, I. do N., Moreira de Assis, M. L., Santos, L. M. dos, Dias, E. F., Bezerra Aragão, V. E., Veríssimo, L. M., Fernandes, N. S. & da Silva, D. R. (2019). pH-responsive release system of isoniazid using palygorskite as a nanocarrier. *Journal of Drug Delivery Science and Technology*, *55*, 101399. https://doi.org/10.1016/j.jddst.2019.101399

David Avnir & Mieczyslaw Jaroniec. (1989). An Isotherm Equation for Adsorption on Fractal Surfaces of Heterogeneous Porous Materials. *Langmuir*, *5*, 1431-1433. https://pubs.acs.org/sharingguidelines

De Arce Velasquez, A., Ferreira, L. M., Stangarlin, M. F. L., Da Silva, C. D. B., Rolim, C. M. B. & Cruz, L. (2014). Novel Pullulan-Eudragit® S100 blend microparticles for oral delivery of risedronate: Formulation, in vitro evaluation and tableting of blend microparticles. *Materials Science and Engineering C*, *38*(1), 212-217. https://doi.org/10.1016/j.msec.2014.02.003

de Carvalho Arjona, J., Samara, M., Ulsen, C., Valenzuela Diaz, F. R. & Demarquette, N. R. (2025). Isoniazid adsorption and release by Cloisite and Laponite: An effect of surface charge. *Materials Chemistry and Physics*, *344*. https://doi.org/10.1016/j.matchemphys.2025.131097

de Carvalho Arjona, J., Ulsen, C., Tada, D., Valenzuela Diaz, F. R. & Demarquette, N. R. (2025). The Influence of Adsorption Incorporation Mechanism on the Release of Isoniazid by Montmorillonite. *Journal of Drug Delivery Science and Technology*, 106809. https://doi.org/https://doi.org/10.1016/j.jddst.2025.106809

de Carvalho Arjona, J., Ulsen, C., Valenzuela-Diaz, F. R. & Demarquette, N. R. (2024). Influence of smectite clays' pores volume on isoniazid adsorption and release. *Applied Clay Science*, *252*. https://doi.org/10.1016/j.clay.2024.107341

de Paiva, L. B., Morales, A. R. & Valenzuela Díaz, F. R. (2008). Organoclays: Properties, preparation and applications. *Applied Clay Science*, *42*(1-2), 8-24. https://doi.org/10.1016/j.clay.2008.02.006

Delgado, A., Gonzalez-Caballero, F. & Bruque, J. M. (1986). On the Zeta Potential and Surface Charge Density of Montmorillonite in Aqueous Electrolyte Solutions. *Journal of Colloid and Interface Science*, *113*(1), 203-211.

Della Giustina, G., Gandin, A., Brigo, L., Panciera, T., Giulitti, S., Sgarbossa, P., D'Alessandro, D., Trombi, L., Danti, S. & Brusatin, G. (2019). Polysaccharide hydrogels for multiscale 3D printing of pullulan scaffolds. *Materials and Design*, *165*. https://doi.org/10.1016/j.matdes.2018.107566

Devi, N. & Maji, T. K. (2010). Genipin crosslinked chitosan'k-carrageenan polyelectrolyte nanocapsules for the controlled delivery of Isoniazid. *International Journal of Polymeric Materials and Polymeric Biomaterials*, *59*(10), 828-841. https://doi.org/10.1080/00914037.2010.484792

Dionísio, M., Cordeiro, C., Remuñán-López, C., Seijo, B., Da Costa, A. M. R. & Grenha, A. (2013). Pullulan-based nanoparticles as carriers for transmucosal protein delivery. *European Journal of Pharmaceutical Sciences*, *50*(1), 102-113. https://doi.org/10.1016/j.ejps.2013.04.018

Djomgoue, P. & Njopwouo, D. (2013). FT-IR Spectroscopy Applied for Surface Clays Characterization. *Journal of Surface Engineered Materials and Advanced Technology*, *03*(04), 275-282. https://doi.org/http://dx.doi.org/10.4236/jsemat.2013.34037

Feng, D., Li, X., Wang, X., Li, J., Sun, F., Sun, Z., Zhang, T., Li, P., Chen, Y. & Zhang, X. (2018). Water adsorption and its impact on the pore structure characteristics of shale clay. *Applied Clay Science*, *155*, 126-138. https://doi.org/10.1016/j.clay.2018.01.017

Ferreira, L. M., De Velasquez, A. A., Schaffazick, S. R. & Cruz, L. (2015). Pullulan: An advantageous natural polysaccharide excipient to formulate tablets of alendronate-loaded microparticles. *Brazilian Journal of Pharmaceutical Sciences*, *51*(1), 27-34. https://doi.org/10.1590/S1984-82502015000100003

Foox, M. & Zilberman, M. (2015). Drug delivery from gelatin-based systems. *Expert Opinion on Drug Delivery*, *12*(9), 1547-1563. https://doi.org/10.1517/17425247.2015.1037272

Gajendiran, M., Jo, H., Kim, K. & Balasubramanian, S. (2019). In vitro controlled release of tuberculosis drugs by amphiphilic branched copolymer nanoparticles. *Journal of Industrial and Engineering Chemistry*, *77*, 181-188. https://doi.org/10.1016/j.jiec.2019.04.033

Garbacz, G., Cadé, D., Benameur, H. & Weitschies, W. (2014). Bio-relevant dissolution testing of hard capsules prepared from different shell materials using the dynamic open flow through test apparatus. *European Journal of Pharmaceutical Sciences*, *57*(1), 264-272. https://doi.org/10.1016/j.ejps.2013.08.039

Genina, N., Boetker, J. P., Colombo, S., Harmankaya, N., Rantanen, J. & Bohr, A. (2017). Anti-tuberculosis drug combination for controlled oral delivery using 3D printed compartmental dosage forms: From drug product design to in vivo testing. *Journal of Controlled Release*, *268*, 40-48. https://doi.org/10.1016/j.jconrel.2017.10.003

Ghanizadeh Tabriz, A., Nandi, U., Hurt, A. P., Hui, H. W., Karki, S., Gong, Y., Kumar, S. & Douroumis, D. (2021). 3D printed bilayer tablet with dual controlled drug release for tuberculosis treatment. *International Journal of Pharmaceutics*, *593*(November 2020), 120147. https://doi.org/10.1016/j.ijpharm.2020.120147

Ghorbel-Abid, I., Vagner, C., Denoyel, R. & Trabelsi-Ayadi, M. (2016). Effect of cadmium and chromium adsorption on the zeta potential of clays. *Desalination and Water Treatment*, *57*(36), 17128-17138. https://doi.org/10.1080/19443994.2015.1134350

Giles, C. H., MacEwan, T. H., Nakhwa, S. N. & Smith, D. (1960). Studies in adsorption. Part XI. A system of classification of solution adsorption isotherms, and its use in diagnosis of adsorption mechanisms and in measurement of specific surface areas of solids. *Journal of the Chemical Society (Resumed)*, 3973-3993. https://doi.org/10.1039/jr9600003973

Giles, Charles H. & Smith, D. (1974). A General Treatment and Classification of the Solute Adsorption Isotherm. *Journal of Colloid and Interface Science*, *47*(3), 755-765. https://doi.org/10.1007/s41193-016-0111-5

Gomes, C. de S. F. & Silva, J. B. P. (2007). Minerals and clay minerals in medical geology. *Applied Clay Science*, *36*(1), 4-21. https://doi.org/10.1016/j.clay.2006.08.006

Göttel, B., de Souza e Silva, J. M., Santos de Oliveira, C., Syrowatka, F., Fiorentzis, M., Viestenz, A., Viestenz, A. & Mäder, K. (2020). Electrospun nanofibers – A promising solid in-situ gelling alternative for ocular drug delivery. *European Journal of Pharmaceutics and Biopharmaceutics*, *146*, 125-132. https://doi.org/10.1016/j.ejpb.2019.11.012

Grenier, J., David, B., Journé, C., Cicha, I., Letourneur, D. & Duval, H. (2023). Perfusion of MC3T3E1 Preosteoblast Spheroids within Polysaccharide-Based Hydrogel Scaffolds: An Experimental and Numerical Study at the Bioreactor Scale. *Bioengineering*, *10*(7). https://doi.org/10.3390/bioengineering10070849

Gulen, B. & Demircivi, P. (2020). Synthesis and characterization of montmorillonite/ciprofloxacin/TiO2 porous structure for controlled drug release of ciprofloxacin tablet with oral administration. *Applied Clay Science*, *197*. https://doi.org/10.1016/j.clay.2020.105768

Hadke, J. & Khan, S. (2021). Preparation of sterculia foetida-pullulan-based semi-interpenetrating polymer network gastroretentive microspheres of amoxicillin trihydrate and optimization by response surface methodology. *Turkish Journal of Pharmaceutical Sciences*, *18*(4), 388-397. https://doi.org/10.4274/tjps.galenos.2020.33341

Han, Y. & Lv, S. (2019). Synthesis of chemically crosslinked pullulan/gelatin-based extracellular matrix-mimetic gels. *International Journal of Biological Macromolecules*, *122*, 1262-1270. https://doi.org/10.1016/j.ijbiomac.2018.09.080

Hernandez-Tenorio, F. & Giraldo-Estrada, C. (2022). Characterization and chemical modification of pullulan produced from a submerged culture of Aureobasidium pullulans ATCC 15233. *Polymer Testing*, *114*. https://doi.org/10.1016/j.polymertesting.2022.107686

Higham, A. K., Bonino, C. A., Raghavan, S. R. & Khan, S. A. (2014). Photo-activated ionic gelation of alginate hydrogel: Real-time rheological monitoring of the two-step crosslinking mechanism. *Soft Matter*, *10*(27), 4990-5002. https://doi.org/10.1039/c4sm00411f

Hillery, A. M. & Brayden, D. J. (2017). Oral Drug Delivery. Dans A. M. Hillery & K. Park (Éd.), *Drug Delivery: Fundamentals & Applications* (Second, p. 171-199). Taylor & Francis Group.

Hoyo, C. Del. (2007). Layered double hydroxides and human health : An overview. *Applied Clay Science*, *36*, 103-121. https://doi.org/10.1016/j.clay.2006.06.010

Hulbert, S. F., Carolina, S., Bowman, L. S. & Carolina, S. (1972). History of ceramic orthopedic implants. *Materials Research Bulletin*, *7*, 1239-1246.

Ishino, R., Yoshino, H., Hirakawa, Y. & Noda, K. (1992). Design and Preparion of Pulsatile Release Tablet as a New Oral Drug Delivery System. *Chemical Pharmaceutical Bulletin*, *40*(11), 3036-3041.

James C. Johnston, R. C. & Menzies, D. (2022). Chapter 5: Treatment of tuberculosis disease. *Canadian Journal of Respiratory, Critical Care, and Sleep Medicine*, *6*(sup1), 66-76. https://doi.org/10.1080/24745332.2022.2036504

Jeon, I. Y. & Baek, J. B. (2010). Nanocomposites derived from polymers and inorganic nanoparticles. *Materials*, *3*(6), 3654-3674. https://doi.org/10.3390/ma3063654

Jeon, O., Bouhadir, K. H., Mansour, J. M. & Alsberg, E. (2009). Photocrosslinked alginate hydrogels with tunable biodegradation rates and mechanical properties. *Biomaterials*, *30*(14), 2724-2734. https://doi.org/https://doi.org/10.1016/j.biomaterials.2009.01.034

Jiang, Z., Hao, J., You, Y., Gu, Q. U. N., Cao, W. & Deng, X. (2009). Biodegradable Thermogelling Hydrogel of P(CL-GL)-PEG-P (CL-GL) Triblock Copolymer: Degradation and Drug Release Behavior. *Journal of Pharmaceutical Sciences*, *98*(8), 2603-2610. https://doi.org/10.1002/jps

Joshi, G. V., Kevadiya, B. D. & Bajaj, H. C. (2010). Design and evaluation of controlled drug delivery system of buspirone using inorganic layered clay mineral. *Microporous and Mesoporous Materials*, *132*(3), 526-530. https://doi.org/10.1016/j.micromeso.2010.04.003

Kevadiya, B. D., Patel, T. A., Jhala, D. D., Thumbar, R. P., Brahmbhatt, H., Pandya, M. P., Rajkumar, S., Jena, P. K., Joshi, G. V., Gadhia, P. K., Tripathi, C. B. & Bajaj, H. C. (2012). Layered inorganic nanocomposites: A promising carrier for 5-fluorouracil (5-FU). *European Journal of Pharmaceutics and Biopharmaceutics*, *81*(1), 91-101. https://doi.org/10.1016/j.ejpb.2012.01.004

Kiaee, G., Dimitrakakis, N., Sharifzadeh, S., Kim, H. J., Avery, R. K., Moghaddam, K. M., Haghniaz, R., Yalcintas, E. P., Barros, N. R. de, Karamikamkar, S., Libanori, A., Khademhosseini, A. & Khoshakhlagh, P. (2022). Laponite-Based Nanomaterials for Drug Delivery. Dans *Advanced Healthcare Materials* (Vol. 11, Numéro 7, p. 1-21). John Wiley and Sons Inc. https://doi.org/10.1002/adhm.202102054

Korsmeyer, R. W., Gurny, R., Doelker, E., Buri, P. & Peppas, N. A. (1983). Mechanisms of solute release from porous hydrophilic polymers. *International Journal of Pharmaceutics*, *15*(1), 25-35. https://doi.org/10.1016/0378-5173(83)90064-9

Krieser, K., Emanuelli, J., Daudt, R. M., Bilatto, S., Willig, J. B., Guterres, S. S., Pohlmann, A. R., Buffon, A., Correa, D. S. & Külkamp-Guerreiro, I. C. (2020). Taste-masked nanoparticles containing Saquinavir for pediatric oral administration. *Materials Science and Engineering C*, *117*. https://doi.org/10.1016/j.msec.2020.111315

Lagaly, G. (2006). *GENERAL INTRODUCTION : CLAYS , CLAY MINERALS , AND CLAY SCIENCE*. *1*(05). https://doi.org/10.1016/S1572-4352(05)01001-9

Lagaly, G, Gonzalez, M. F. & Weiss, A. (1976). Problems in layer-charge determination of montmorillonites. *Clay Minerals*, *11*(3), 173-187.

Lagaly, Gerhard & Beneke, K. (1976). Cation exchange reactions of the mica-like potassium niobate K4Nb6O17. *Journal of Inorganic and Nuclear Chemistry*. https://doi.org/10.1016/0022-1902(76)90019-1

Li, C., Liu, Y. Y., Wei, M., Liu, J., Yu, X., Hu, P. & Liu, Y. Y. (2022). A novel core-shell rifampicin/isoniazid electrospun nanofiber membrane for long time drug dissolution. *Engineered Regeneration*, *3*(1), 73-79. https://doi.org/10.1016/j.engreg.2022.02.002

Li, Z., Chang, P. H., Jean, J. S., Jiang, W. T. & Wang, C. J. (2010). Interaction between tetracycline and smectite in aqueous solution. *Journal of Colloid and Interface Science*, *341*(2), 311-319. https://doi.org/10.1016/j.jcis.2009.09.054

Lucinda-Silva, R. M. & Evangelista, R. C. (2003). Microspheres of alginate-chitosan containing isoniazid. *Journal of Microencapsulation*, *20*(2), 145-152. https://doi.org/10.1080/02652040210162621

M. Chorom & P. Rengasamy. (1995). Dispersion and Zeta Potential of Pure Clays as Related to net Particle Charge Under Varying pH, Electrolyte Concentration and Cation Type. *European Journal of Soil Science*, *46*, 657-665.

Maisanaba, S., Pichardo, S., Puerto, M., Gutiérrez-Praena, D., Cameán, A. M. & Jos, A. (2015). Toxicological evaluation of clay minerals and derived nanocomposites: A review. *Environmental Research*, *138*, 233-254. https://doi.org/https://doi.org/10.1016/j.envres.2014.12.024

Marengo, R. C., Mengatto, L. N., Olivares, M. L. & Berli, C. L. A. (2021). Microfluidics-based encapsulation of isoniazid in egg white/carrageenan microparticles for sustained release. *Food Hydrocolloids for Health*, *1*, 100041. https://doi.org/10.1016/j.fhfh.2021.100041

Mitchell, N. J., Kumi, J., Aleser, M., Elmore, S. E., Rychlik, K. A., Zychowski, K. E., Romoser, A. A., Phillips, T. D. & Ankrah, N.-A. (2014). Short-Term Safety and Efficacy of Calcium Montmorillonite Clay (UPSN) in Children. *The American Society of Tropical Medicine and Hygiene*, *91*(4), 777-785. https://doi.org/10.4269/ajtmh.14-0093

Mugnaini, G., Resta, C., Poggi, G. & Bonini, M. (2021). Photopolymerizable pullulan: Synthesis, self-assembly and inkjet printing. *Journal of Colloid and Interface Science*, *592*, 430-439. https://doi.org/10.1016/j.jcis.2021.02.074

Murata, Y., Isobe, T., Kofuji, K., Nishida, N. & Kamaguchi, R. (2010). Preparation of fast dissolving films for oral dosage from natural polysaccharides. *Materials*, *3*(8), 4291-4299. https://doi.org/10.3390/ma3084291

Muráth, S., Dvorníková, N., Moreno-Rodríguez, D., Novotný, R., Pospíšil, M., Urbanová, M., Brus, J. & Kovanda, F. (2023). Intercalation of atorvastatin and valsartan into Mg[sbnd]Al layered double hydroxide host using a restacking procedure. *Applied Clay Science*, *231*. https://doi.org/10.1016/j.clay.2022.106717

Muselík, J., Komersová, A., Kubová, K., Matzick, K. & Skalická, B. (2021). A critical overview of FDA and EMA statistical methods to compare in vitro drug dissolution profiles of pharmaceutical products. *Pharmaceutics*, *13*(10). https://doi.org/10.3390/pharmaceutics13101703

Nomicisio, C., Ruggeri, M., Bianchi, E., Vigani, B., Valentino, C., Aguzzi, C., Viseras, C., Rossi, S. & Sandri, G. (2023). Natural and Synthetic Clay Minerals in the Pharmaceutical and Biomedical Fields. Dans *Pharmaceutics* (Vol. 15, Numéro 5). MDPI. https://doi.org/10.3390/pharmaceutics15051368

Nonsuwan, P., Phiboonchaiyanan, P. P., Hirun, N. & Kraisit, P. (2023). Curcumin-loaded methacrylate pullulan with grafted carboxymethyl-β-cyclodextrin to form hydrogels for wound healing: In vitro evaluation. *Carbohydrate Polymers*, *321*. https://doi.org/10.1016/j.carbpol.2023.121294

Oliveira, P. M., Matos, B. N., Pereira, P. A. T., Gratieri, T., Faccioli, L. H., Cunha-Filho, M. S. S. & Gelfuso, G. M. (2017). Microparticles prepared with 50–190 kDa chitosan as promising non-toxic carriers for pulmonary delivery of isoniazid. *Carbohydrate Polymers*, *174*, 421-431. https://doi.org/10.1016/j.carbpol.2017.06.090

Pandey, G., Yadav, S. K. & Mishra, B. (2016). Preparation and characterization of isoniazid and lamivudine co-loaded polymeric microspheres. *Artificial Cells Nanomedicine Biotechnology*, *44*(8), 1867-1877.

Peng, Q., Xu, P. & Xiao, S. (2018). Porous Laponite/Poly(L-lactic acid) Membrane with Controlled Release of TCH and Efficient Antibacterial Performance. *Fibers and Polymers*, *19*(3), 477-488. https://doi.org/10.1007/s12221-018-7925-5

Perrie, Y., Rades, T. & Graeser, K. (2019). Principles of Controlled Release. Dans A. M. Hillery & K. Park (Éd.), *Drug delivery: fundamentals & applications* (2nd éd., p. 25-46). Taylor & Francis. https://doi.org/10.1201/9781315382579

Pires, P. C., Damiri, F., Zare, E. N., Hasan, A., Neisiany, R. E., Veiga, F., Makvandi, P. & Paiva-Santos, A. C. (2024). A review on natural biopolymers in external drug delivery systems for wound healing and atopic dermatitis. Dans *International Journal of Biological Macromolecules* (Vol. 263). Elsevier B.V. https://doi.org/10.1016/j.ijbiomac.2024.130296

Priyadarshi, R., Kim, S. M. & Rhim, J. W. (2021). Pectin/pullulan blend films for food packaging: Effect of blending ratio. *Food Chemistry*, *347*. https://doi.org/10.1016/j.foodchem.2021.129022

Public Health Agency of Canada. (2025, 31. janvier). *Tuberculosis Disease in Canada, 2023 (infographic)*. https://www.canada.ca/en/public-health/services/publications/diseases-conditions/tuberculosis-disease-2023-infographic.html.

Qin, X., He, R., Chen, H., Fu, D., Peng, Y., Meng, S., Chen, C. & Yang, L. (2021). Methacrylated pullulan/polyethylene (glycol) diacrylate composite hydrogel for cartilage tissue engineering. *Journal of Biomaterials Science, Polymer Edition*, *32*(8), 1057-1071. https://doi.org/10.1080/09205063.2021.1899888

Reinholdt, M. X., Hubert, F., Faurel, M., Tertre, E., Razafitianamaharavo, A., Francius, G., Prêt, D., Petit, S., Béré, E., Pelletier, M. & Ferrage, E. (2013). Morphological properties of vermiculite particles in size-selected fractions obtained by sonication. *Applied Clay Science*, *77-78*, 18-32. https://doi.org/10.1016/j.clay.2013.03.013

Saifullah, B., El Zowalaty, M. E., Arulselvan, P., Fakurazi, S., Webster, T. J., Geilich, B. M. & Hussein, M. Z. (2016). Synthesis, characterization, and efficacy of antituberculosis isoniazid zinc aluminum-layered double hydroxide based nanocomposites. *International Journal of Nanomedicine*, *11*, 3225-3237. https://doi.org/10.2147/IJN.S102406

Saikia, C., Hussain, A., Ramteke, A., Sharma, H. K. & Maji, T. K. (2015). Carboxymethyl starch-chitosan-coated iron oxide magnetic nanoparticles for controlled delivery of isoniazid. *Journal of Microencapsulation*, *32*(1), 29-39. https://doi.org/10.3109/02652048.2014.940015

Sarmah, M., Hussain, A., Ramteke, A. & Maji, T. K. (2016). Isoniazid loaded gelatin-cellulose whiskers nanoparticles for controlled drug delivery applications. *Journal of Chemical Sciences*, *128*(8), 1291-1301. https://doi.org/10.1007/s12039-016-1129-6

Sciascia, L., Calabrese, I., Cavallaro, G., Merli, M., Scialabba, C. & Liveri, M. L. T. (2021). Modified montmorillonite as drug delivery agent for enhancing antibiotic therapy. *Minerals*, *11*(12). https://doi.org/10.3390/min11121315

Seki, T., Fukushi, N., Chono, S. & Morimoto, K. (2008). Effects of sperminated polymers on the pulmonary absorption of insulin. *Journal of Controlled Release*, *125*(3), 246-251. https://doi.org/10.1016/j.jconrel.2007.10.017

Shah, L. A., da Silva Valenzuela, M. das G., Ehsan, A. M., Valenzuela Díaz, F. R. & Khattak, N. S. (2013). Characterization of Pakistani purified bentonite suitable for possible pharmaceutical application. *Applied Clay Science*, *83-84*, 50-55. https://doi.org/10.1016/j.clay.2013.08.007

Shah, L. A., Silva Valenzuela, M. das G. da, Farooq, M., Khattak, S. A. & Valenzuela Díaz, F. R. (2018). Influence of preparation methods on textural properties of purified bentonite. *Applied Clay Science*, *162*, 155-164. https://doi.org/10.1016/j.clay.2018.06.001

Silva-Valenzuela, M. das G., Chambi-Peralta, M. M., Sayeg, I. J., de Souza Carvalho, F. M., Wang, S. H. & Valenzuela-Díaz, F. R. (2018). Enrichment of clay from Vitoria da Conquista (Brazil) for applications in cosmetics. *Applied Clay Science*, *155*, 111-119. https://doi.org/10.1016/j.clay.2018.01.011

Sing, K. S. W., Everett, D. H., Haul, R. A. W., Moscou, L., Pierotti, R. A., Rouquérol, J. & Siemieniewska, T. (1985). REPORTING PHYSISORPTION DATA FOR GAS/SOLID SYSTEMS. *Pure and Applied Chemistry*, *57*(4), 603-619.

Singh, R. S., Kaur, N., Hassan, M. & Kennedy, J. F. (2021). Pullulan in biomedical research and development - A review. Dans *International Journal of Biological Macromolecules* (Vol. 166, p. 694-706). Elsevier B.V. https://doi.org/10.1016/j.ijbiomac.2020.10.227

Soni, S. R. & Ghosh, A. (2017). Exploring pullulan-poly(vinyl alcohol) interpenetrating network microspheres as controlled release drug delivery device. *Carbohydrate Polymers*, *174*, 812-822. https://doi.org/10.1016/j.carbpol.2017.07.016

Sosnik, A. & Seremeta, K. P. (2015). Advantages and challenges of the spray-drying technology for the production of pure drug particles and drug-loaded polymeric carriers. Dans *Advances in Colloid and Interface Science* (Vol. 223, p. 40-54). Elsevier B.V. https://doi.org/10.1016/j.cis.2015.05.003

Souza, I. M. S., Borrego-Sánchez, A., Sainz-Díaz, C. I., Viseras, C. & Pergher, S. B. C. (2021). Study of Faujasite zeolite as a modified delivery carrier for isoniazid. *Materials Science and Engineering C*, *118*, 12. https://doi.org/10.1016/j.msec.2020.111365

Souza, I. M. S., Sainz-Díaz, C. I., Viseras, C. & Pergher, S. B. C. (2020). Adsorption capacity evaluation of zeolites as carrier of isoniazid. *Microporous and Mesoporous Materials*, *292*. https://doi.org/10.1016/j.micromeso.2019.109733

Stipa, P., Marano, S., Galeazzi, R., Minnelli, C., Mobbili, G. & Laudadio, E. (2021). Prediction of drug-carrier interactions of PLA and PLGA drug-loaded nanoparticles by molecular dynamics simulations. *European Polymer Journal*, *147*(November 2020), 110292. https://doi.org/10.1016/j.eurpolymj.2021.110292

Swartzen-Allen, S. L. & Matijevic, E. (1974). Surface and Colloid Chemistry of Clays. *Chemical Reviews*, *74*(3), 385-400.

Tan, K. L. & Hameed, B. H. (2017). Insight into the adsorption kinetics models for the removal of contaminants from aqueous solutions. *Journal of the Taiwan Institute of Chemical Engineers*, *74*, 25-48. https://doi.org/10.1016/j.jtice.2017.01.024

Özer, Ö., Özcan, I., Çetin, E. Ö., Tekmen, I., Sönmez, Ü., Kırılmaz, L. & Güneri, T. (2006). Evaluation of in vitro release and skin irritation of benzoyl peroxide-containing products. *Journal of Drug Delivery Science and Technology*, *16*(6), 449-454.

Tören, E. & Mazari, A. A. (2024). Pullulan/Collagen Scaffolds Promote Chronic Wound Healing via Mesenchymal Stem Cells. *Micro*, *4*(4), 599-620. https://doi.org/10.3390/micro4040037

Ulsen, C., Tseng, E., Angulo, S. C., Landmann, M., Contessotto, R., Balbo, J. T. & Kahn, H. (2019). Concrete aggregates properties crushed by jaw and impact secondary crushing. *Journal of Materials Research and Technology*, *8*(1), 494-502. https://doi.org/10.1016/j.jmrt.2018.04.008

Vishwanath, B., Shivakumar, H. R., Sheshappa, R. K., Ganesh, S., Prasad, P., Guru, G. S. & Bhavya, B. B. (2012). In-vitro release study of metoprolol succinate from the bioadhesive films of pullulan-polyacrylamide blends. *International Journal of Polymeric Materials and Polymeric Biomaterials*, *61*(4), 300-307. https://doi.org/10.1080/00914037.2011.584227

Vueba, M., De Carvalho, L. B., Veiga, F., Sousa, J. & Pina, M. (2013). In vitro release of ketoprofen from hydrophilic matrix tablets containing cellulose polymer mixtures. *Drug Development and Industrial Pharmacy*, *39*, 1651-1662. https://doi.org/10.3109/03639045.2012.729146

Wang, S., Zheng, F., Huang, Y., Fang, Y., Shen, M., Zhu, M. & Shi, X. (2012). Encapsulation of amoxicillin within laponite-doped poly(lactic-co-glycolic acid) nanofibers: Preparation, characterization, and antibacterial activity. *ACS Applied Materials and Interfaces*, *4*(11), 6393-6401. https://doi.org/10.1021/am302130b

Wang, X., Cheng, H., Chai, P., Bian, J., Wang, X., Liu, Y., Yin, X., Pan, S. & Pan, Z. (2020). Pore Characterization of Different Clay Minerals and Its Impact on Methane Adsorption Capacity. *Energy and Fuels*, *34*(10), 12204-12214. https://doi.org/10.1021/acs.energyfuels.0c01922

WHO. (2024). *Global Tuberculosis Report 2024*.

WHO, W. H. O. (2020). The impact of COVID-19 on the TB epidemic : A community perspective. *Tuberculosis Weekly report*.

Zauška, Ľ., Beňová, E., Urbanová, M., Brus, J., Zeleňák, V., Hornebecq, V. & Almáši, M. (2022). Adsorption and Release Properties of Drug Delivery System Naproxen-SBA-15: Effect of Surface Polarity, Sodium/Acid Drug Form and pH. *Journal of Functional Biomaterials*, *13*(4). https://doi.org/10.3390/jfb13040275

Zeng, Q., Qi, X., Zhang, M., Tong, X., Jiang, N., Pan, W., Xiong, W., Li, Y., Xu, J., Shen, J. & Xu, L. (2020). Efficient decontamination of heavy metals from aqueous solution using pullulan/polydopamine hydrogels. *International Journal of Biological Macromolecules*, *145*, 1049-1058. https://doi.org/10.1016/j.ijbiomac.2019.09.197

Zheng, L., Zhou, B., Qiu, X., Xu, X., Li, G., Lee, W. Y. W., Jiang, J. & Li, Y. (2019). Direct assembly of anticancer drugs to form Laponite-based nanocomplexes for therapeutic co-delivery. *Materials Science and Engineering C*, *99*, 1407-1414. https://doi.org/10.1016/j.msec.2019.02.083

Zheng, W., Zhang, Z., Li, Y., Wang, L., Fu, F., Diao, H. & Liu, X. (2022). A novel pullulan oxidation approach to preparing a shape memory sponge with rapid reaction capability for massive hemorrhage. *Chemical Engineering Journal*, *447*. https://doi.org/10.1016/j.cej.2022.137482

Zhu, R., Chen, Q., Zhou, Q., Xi, Y., Zhu, J. & He, H. (2016). Adsorbents based on montmorillonite for contaminant removal from water: A review. *Applied Clay Science*, *123*, 239-258. https://doi.org/10.1016/j.clay.2015.12.024